

Draft for thesis:

Sensitivity of Tropospheric Chemistry to the  
Source of NO<sub>x</sub> from Lightning: Simulations  
with the Global 3D Chemistry-Transport  
Model MATCH-MPIC

Lorenzo Labrador

April 5, 2005



# Contents

|          |  |           |
|----------|--|-----------|
| <b>1</b> | <b>Introduction</b>  | <b>5</b>  |
| 1.1      | Chemistry of Nitrogen Oxides . . . . .   | 7         |
| 1.2      | The Phenomenon of Lightning . . . . .  | 13        |
| 1.2.1    | The Electrification of Clouds . . . . .  | 17        |
| 1.2.2    | Theories of Cloud Electrification . . . . .  | 20        |
| 1.2.3    | The Lightning Discharge . . . . .  | 23        |
| 1.2.4    | Negative Cloud to Ground Discharges . . . . .  | 24        |
| 1.2.5    | Positive Cloud to Ground Discharges . . . . .  | 26        |
| 1.2.6    | Cloud Discharges . . . . .   | 26        |
| 1.3      | Production of Nitrogen Oxide by Lightning . . . . .  | 28        |
| 1.3.1    | Theoretical Studies . . . . .  | 28        |
| 1.3.2    | Experimental Studies . . . . .   | 30        |
| 1.3.3    | Field Observations . . . . .   | 31        |
| 1.4      | Objectives of this Study . . . . .   | 31        |
| 1.4.1    | Outline of this Study . . . . .  | 33        |
| <b>2</b> | <b>The Model of Atmospheric Transport and Chemistry, Max<br/>Planck Institute for Chemistry Version (MATCH-MPIC)</b> | <b>35</b> |
| 2.1      | MATCH-MPIC at a Glance . . . . .   | 35        |

|          |   |           |
|----------|---|-----------|
| 2.2      | Meteorology in MATCH-MPIC . . . . .   | 36        |
| 2.2.1    | Advection . . . . .   | 36        |
| 2.2.2    | Convection and Clouds . . . . .   | 37        |
| 2.2.3    | Vertical Turbulent Diffusion . . . . .  | 38        |
| 2.3      | Photochemistry in MATCH-MPIC . . . . .  | 39        |
| 2.3.1    | Photochemistry Integration . . . . .  | 39        |
| 2.3.2    | Photolysis Rates . . . . .  | 40        |
| 2.3.3    | Wet Deposition and Vertical Redistribution by Hy-<br>drometeors . . . . .   | 40        |
| 2.3.4    | Dry Deposition . . . . .  | 41        |
| 2.3.5    | Emissions . . . . .   | 42        |
| 2.4      | Sensitivity Studies . . . . .   | 48        |
| <b>3</b> | <b>Horizontal Distribution of Modeled Lightning in MATCH-<br/>MPIC</b>  | <b>53</b> |
| 3.1      | The Optical Transient Detector and the Lightning Imaging<br>Sensor . . . . .  | 54        |
| 3.2      | Comparisons Between Modeled Flash Activity and OTD/LIS<br>Data . . . . .  | 56        |
| 3.2.1    | Seasonal Variations . . . . .   | 63        |
| 3.3      | Sensitivity Runs with the Allen and Pickering (2002) Con-<br>vective Mass Flux Lightning Parameterization . . . . . | 71        |
| <b>4</b> | <b>Effects of Lightning-Produced Nitrogen Oxides on Tropo-<br/>spheric Chemistry</b>                                | <b>77</b> |
| 4.1      | Basic significance of $\text{LtNO}_x$ for $\text{NO}_x$ and Other Tropospheric<br>Trace Gas Concentrations. . . . . | 77        |
| 4.1.1    | Effects on $\text{NO}_x$ . . . . .  | 78        |

---

|          |   |            |
|----------|---|------------|
| 4.1.2    | Effects on O <sub>3</sub> . . . . .   | 82         |
| 4.1.3    | Effects on HNO <sub>3</sub> . . . . .   | 85         |
| 4.1.4    | Effects on PAN . . . . .  | 88         |
| 4.1.5    | Effects on OH and the Tropospheric Oxidizing Efficiency . . . . .   | 92         |
| 4.2      | Sensitivity of Tropospheric Chemistry to Increases in the Magnitude of the Source of NO <sub>x</sub> from Lightning . . . . . | 101        |
| 4.3      | Comparisons of Model Output with Observations . . . . .   | 108        |
| <b>5</b> | <b>Importance of the Vertical Distribution of the Source of NO<sub>x</sub> from Lightning</b>                                 | <b>121</b> |
| 5.1      | Effects on NO <sub>x</sub> . . . . .  | 122        |
| 5.2      | Effects on O <sub>3</sub> . . . . .   | 126        |
| 5.3      | Effects on OH . . . . .   | 126        |
| 5.4      | Effects on HNO <sub>3</sub> . . . . .   | 128        |
| 5.5      | Effects on PAN . . . . .  | 130        |
| <b>6</b> | <b>Conclusions</b>  | <b>133</b> |



# Chapter 1

## Introduction

The Earth's atmosphere is an extremely complex system. Its multi-layered structure, with its many gas constituents, is home to many physical and chemical processes fueled mainly by the sun's energy. Only in the last two centuries has man begun to understand the fundamental processes that take place in the Earth's gaseous envelope and assess their importance to the sustenance of life. But at the same time mankind, as a result of its technological achievements and everyday activities, has started to have an effect on the Earth's atmosphere, mainly through the injection of trace gases that, in large quantities, have the power to alter its natural equilibrium.

Since the dawn of the industrial revolution, considerable amounts of so-called "greenhouse gases", such as ozone ( $O_3$ ), carbon dioxide ( $CO_2$ ) and methane ( $CH_4$ ), which have the ability to trap outgoing long-wave radiation, have been building up in the Earth's atmosphere and are thought to be responsible for an increase in the atmosphere's temperature since the early decades of the twentieth century. Certain chlorine-based compounds, a by-product of industrial processes, were found to be responsible for the rapid destruction of ozone over the polar regions, giving rise to the so-called ozone hole. Many studies point towards possible radical alteration in the Earth's climate if the pace of industrialization and its consequent emissions of gases, such as carbon dioxide and nitrogen oxides continues to

increase unchecked and strong emission control policies are not instituted. It has thus become a priority in the latest decades to determine both the naturally-occurring, as well as the anthropogenic amounts of trace gases in the atmosphere. Of these gases, ozone is of great importance; in the stratosphere it absorbs incoming ultraviolet radiation, thereby protecting life at the surface. In the troposphere it is, as mentioned, a powerful greenhouse gas and, in high concentrations near the surface, can have detrimental effects on life. Its abundance there is largely controlled by the presence of oxidized nitrogen compounds and various hydrocarbons, which occur both naturally and through human production.

Of the natural sources of oxidized nitrogen, production by lightning constitutes an important part of the budget of total nitrogen oxides ( $\text{NO}_x = \text{NO} + \text{NO}_2$ ) and is one of the sources with the largest uncertainty, with estimates ranging from 1-20 Tg(N)/yr (Lawrence *et al.*, 1995; Price *et al.*, 1997a). Produced mostly in and around active thunderstorms, lightning-produced  $\text{NO}_x$  (Lt $\text{NO}_x$  hereafter) is readily carried to the upper levels of the troposphere by convection, where its lifetime is considerably longer than in the lower troposphere (LT). The link between lightning and nitrogen oxides was probably first recognized in the 1820s by J. von Liebig (von Liebig, 1827), although it was not until the 1970s that further studies started to be conducted to determine its role in the photochemistry of the troposphere, primarily in controlling ozone concentrations. In order to determine an accurate budget for tropospheric ozone, it is crucial in turn to determine an accurate budget for Lt $\text{NO}_x$ . Lt $\text{NO}_x$  is also closely linked with OH radical production and hence has the potential to affect the atmosphere's oxidizing efficiency (Labrador *et al.*, 2004b).

The large uncertainty in Lt $\text{NO}_x$  production estimates is reflected in Table 1.1. From early estimates of the production range exceeding 100 Tg(N)/yr, only in the last decade do we see the estimates in different studies settling within the 1-20 Tg(N) range. The reasons for these uncertainties are manifold, among them relatively poorly understood aspects of the lightning phenomenon itself, including the charge separation process,

the amount of energy deposited per flash, the partitioning among cloud-to-ground, intracloud and intercloud flashes, as well as those aspects related to the production of  $\text{NO}_x$ , such as the amount of NO molecules produced per flash or per unit energy. While a number of laboratory studies have been carried out in order to try to better determine these parameters, issues such as the similarity of simulated sparks to real flashes and the scalability of laboratory measurements to the characteristic dimensions of lightning in the atmosphere may be a source of error. The global distribution of lightning, as well as the total global flash rate continue to be a source of uncertainty, although this has been improved substantially by the recent advent of dedicated space-borne observation platforms such as the Optical Transient Detector (OTD) and Lightning Imaging Sensor (LIS) (Christian *et al.*, 2003). Airborne observation campaigns provide critically-needed data to help validate model results. As will be discussed later, there is a definite need for further measurements of  $\text{NO}_x$  enhancements in storm areas, particularly in the tropics.

This chapter will offer an introduction into the basics of the chemistry of nitrogen oxides as well as the phenomenon of lightning and the processes whereby nitrogen oxides are produced in lightning discharges, followed by an overview of the objectives and contents of this thesis.

## 1.1 Chemistry of Nitrogen Oxides

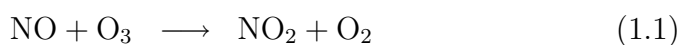
Nitrogen oxides play a very important role in the chemistry of the atmosphere. They catalyze the series of reactions that lead to the formation of  $\text{O}_3$  and also indirectly control the formation of the OH radical, thus influencing the oxidizing efficiency of the atmosphere. They are mostly emitted into the atmosphere in the form of nitric oxide (NO), via such processes as combustion, microbial activity in soils, or lightning, and is then converted to nitrogen dioxide ( $\text{NO}_2$ ), which photolyzes during daytime to reform NO. The main sources of nitrogen oxides are summarized in Table 2.1.

Table 1.1: Global estimates of lightning-produced  $\text{NO}_x$  (values prior to 1995 adopted from Lawrence *et al.* (1995))

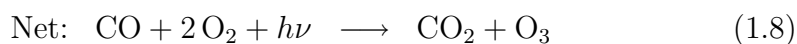
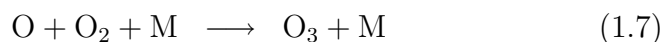
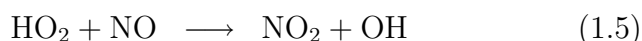
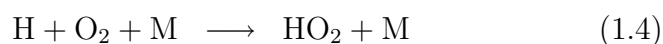
| REFERENCE<br>(type of estimate)                    | Molec.(NO)/unit energy<br>( $\times 10^{16}$ molec./J) | Molec.(NO)/fl.<br>( $\times 10^{25}$ molec./fl.) | Numb. of flashes<br>(flashes/sec) | Lt $\text{NO}_x$ prod. rate<br>(Tg(N)/yr) |
|--|--|--|-----------------------------------|---|
| Tuck (1976) <sup>a</sup>                           | -  | 1.1  | 500                               | 4   |
| Chameides <i>et al.</i> (1977) <sup>a</sup>        | 3-7  | 6-14   | 400                               | 18-41                                     |
| Noxon (1976) <sup>c</sup>                          | -  | 10   | 500                               | 37  |
| Chameides (1979) <sup>a</sup>                      | 8-17   | 16-34  | 400                               | 47-100                                    |
| Dawson (1980) <sup>a</sup>                         | -  | 0.8  | 500                               | 3   |
| Hill <i>et al.</i> (1980) <sup>a</sup>             | -  | 1.2  | 100                               | 0.9                                       |
| Levine <i>et al.</i> (1981) <sup>b</sup>           | 5 $\pm$ 2  | 0.5  | 500                               | 1.8 $\pm$ 0.7                             |
| Kowalczyk and Bauer (1982) <sup>a</sup> -          | -  | 10   | 500                               | 5.7                                       |
| Peyrous and Lapyere (1982) <sup>b</sup>            | 1.6  | 3.2  | 400                               | 9.4                                       |
| Drapcho <i>et al.</i> (1983) <sup>c</sup>          | -  | 40   | 100                               | 30  |
| Chameides <i>et al.</i> (1987) <sup>d</sup>        | -  | -  | -                                 | 7   |
| Franzblau and Popp (1989) <sup>c</sup>             | -  | 300  | 100                               | 220                                       |
| Sisterson and Liaw (1990) <sup>a</sup>             | -  | 8.2  | 200                               | 12  |
| Liaw <i>et al.</i> (1990) <sup>e</sup>             | -  | -  | -                                 | 81  |
| Lawrence <i>et al.</i> (1995) <sup>e</sup>         | -  | 2.3(1-7)   | 100(70-150)                       | 2(1-8)                                    |
| Kumar <i>et al.</i> (1995) <sup>c</sup>            | -  | 0.5  | 100                               | 2   |
| Ridley <i>et al.</i> (1996) <sup>c</sup>           | -  | -  | 100                               | 2-5                                       |
| Levy <i>et al.</i> (1996) <sup>a</sup>             | -  | -  | -                                 | 2-6                                       |
| Price <i>et al.</i> (1997a) <sup>c</sup>           | 10   | -  | 70-100                            | 12.2(5-20)                                |
| Price <i>et al.</i> (1997b) <sup>a</sup>           | 10   | -  | -                                 | 13.2(5-25)                                |
| Wang <i>et al.</i> (1998) <sup>b</sup>             | -  | 3.1  | 30-100                            | 2.5-8.3                                   |
| Nesbitt <i>et al.</i> (2000) <sup>c</sup>          | -  | 0.87-6.2   | 57                                | 0.9                                       |
| Navarro-Gonzales <i>et al.</i> (2001) <sup>b</sup> | 15 $\pm$ 5   | -  | -                                 | -   |
| Huntrieser <i>et al.</i> (2002) <sup>c</sup>       | -  | $2.7 \times 10^{21}$ molec/m flash               | -                                 | 3   |
| Christian <i>et al.</i> (2003) <sup>c</sup>        | -  | -  | 44 $\pm$ 5                        | -   |
| Fehr <i>et al.</i> (2004) <sup>c</sup>             | -  | 21   | -                                 | -   |

<sup>a</sup>Theoretical estimate<sup>b</sup>Laboratory-based estimate<sup>c</sup>Field observations-based estimate<sup>d</sup>Thunderstorm extrapolation-based estimate<sup>e</sup>Review-based estimate

Once emitted into the atmosphere, NO reacts quickly to form different oxidized compounds. NO and NO<sub>2</sub> are commonly treated together as the family NO<sub>x</sub>, due to their fast turnover time of  $\sim 100$  seconds. During daytime, and in the presence of sunlight, NO is oxidized by O<sub>3</sub> into NO<sub>2</sub>. NO<sub>2</sub> is then photolyzed into NO + O and the oxygen atom thus formed reacts with oxygen to form O<sub>3</sub>, thus establishing a photochemical stationary state:

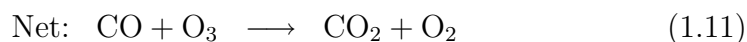
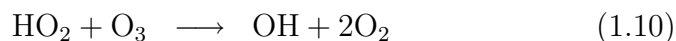
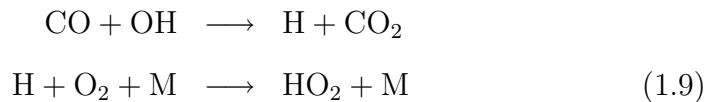


The role of nitrogen oxides in controlling the formation of O<sub>3</sub> takes place in reaction sequences such as the oxidation of carbon monoxide (CO). In the presence of solar radiation of wavelengths below 400nm, the following set of reactions occur:



where M denotes an energy-accepting third body. This leads to the formation of O<sub>3</sub> without loss of hydroxyl and peroxy radicals, NO, or NO<sub>2</sub>. These reactions are typical of NO<sub>x</sub>-rich environments, where high amounts of NO relative to O<sub>3</sub> are present. In NO<sub>x</sub>-poor environments, the oxidation of CO

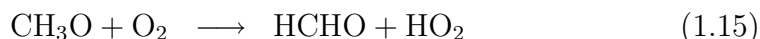
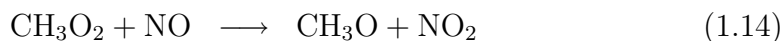
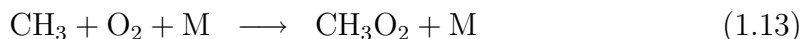
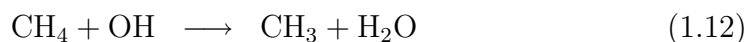
can proceed as follows:



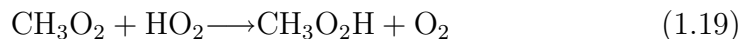
leading to  $\text{O}_3$  destruction, again without loss of either OH or  $\text{HO}_2$ .

In  $\text{NO}_x$ -rich environments, equation 1.5 will dominate over equation 1.10. The ratio of the reaction coefficients of eq. 1.10 to eq. 1.5, approximately  $2 \times 10^{-4}$ , can give an indication of the mixing ratios of  $\text{NO}_x$  and of  $\text{O}_3$  necessary to produce or destroy  $\text{O}_3$ ; for  $\text{O}_3$  mixing ratios of  $\sim 20$  nmol/mol in the lower troposphere,  $\text{NO}_x$  mixing ratios of  $\sim 5$  pmol/mol will lead to  $\text{O}_3$  production. In the upper troposphere, with  $\text{O}_3$  mixing ratios of  $\sim 100$  nmol/mol,  $\text{NO}_x$  mixing ratios of 20 pmol/mol will suffice to produce  $\text{O}_3$  (Crutzen, 1972, 1974; Crutzen *et al.*, 1979; Liu *et al.*, 1980; Gallardo, 1996).

In  $\text{NO}_x$ -rich environments, a different set of reactions, namely the oxidation of methane ( $\text{CH}_4$ ), also results in net production of  $\text{O}_3$  :



with, as in the oxidation of CO, no net loss of NO, NO<sub>2</sub>, OH or HO<sub>2</sub>. In NO<sub>x</sub>-poor environments, the methyl peroxy radical in eq. 1.14 reacts with HO<sub>2</sub> instead of NO leading to:



Methylhydroperoxide (CH<sub>3</sub>O<sub>2</sub>H) can either photolyze or react with OH to form CH<sub>3</sub>O<sub>2</sub> plus water. This reaction tends to destroy HO<sub>x</sub> (HO<sub>x</sub> = OH + HO<sub>2</sub>), which will be lower under low NO<sub>x</sub> conditions (von Kuhlmann, 2001).

The lifetime of the overall family NO<sub>x</sub> varies considerably with altitude, ranging from ~ 10 days in the upper troposphere (UT) (Jaeglé *et al.*, 1997) to ~10 hours in the planetary boundary layer. This change in lifetimes is mainly due to the change in partitioning between NO and NO<sub>2</sub> and the temperature dependence of the NO<sub>2</sub> and OH reactions; in the lower troposphere, NO<sub>x</sub> consists mainly of NO<sub>2</sub> which reacts with OH to form nitric acid (HNO<sub>3</sub>) via:



which, due to its high solubility, is readily removed by wet deposition in about one week (Seinfeld and Pandis, 1998). On the other hand, in the UT,  $\text{NO}_x$  is mainly made up of NO (up to 80%) (Crawford *et al.*, 1996) which, along with colder temperatures, further hinders reaction with OH. Furthermore, in the UT removal mechanisms such as wet and dry deposition are not as effective as in the LT. NO and  $\text{NO}_2$  are not particularly soluble in water, which means that they can be effectively transported to the upper reaches of the troposphere, where reaction 1.20 can still occur, but where  $\text{HNO}_3$  is not subject to dry deposition and where wet deposition is less likely.

Once in the UT,  $\text{HNO}_3$  can be transformed back into  $\text{NO}_x$  via:



or by reaction with OH:

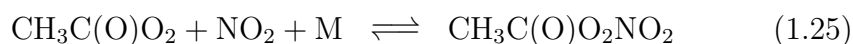


which makes  $\text{HNO}_3$  an effective  $\text{NO}_x$  reservoir species.

$\text{HNO}_3$  is also formed as a result of the reaction of  $\text{NO}_2$  with  $\text{O}_3$  to form the nitrate radical ( $\text{NO}_3$ ); further reaction with  $\text{NO}_2$  leads to the formation of di-nitrogen pentoxide ( $\text{N}_2\text{O}_5$ ), which reacts with water on aerosol particles to form  $\text{HNO}_3$  (Dentener and Crutzen, 1993). In the UT, the lifetime of  $\text{HNO}_3$  is mainly determined by photolysis, and its reconversion into  $\text{NO}_x$  gains importance, thus turning  $\text{HNO}_3$  into an important reservoir species of  $\text{NO}_x$ .

Other oxidized nitrogen species, such as peroxyacetyl nitrate, or PAN ( $\text{CH}_3\text{C}(\text{O})\text{O}_2\text{NO}_2$ ), also act as  $\text{NO}_x$  reservoir species, particularly in the UT where, due to the strong temperature dependence of its reaction, it becomes quite stable. Long range transport can act to deposit PAN in remote areas with low  $\text{NO}_x$  background levels, where in the presence of

high temperatures, it can decompose and release  $\text{NO}_x$ . The reaction chain leading to PAN formation, and subsequent degradation back into  $\text{NO}_2$  serves as a good example to illustrate the reservoir species principle:



Under UT temperature conditions, the equilibrium reaction 1.25 is shifted toward the right, whereas under lower tropospheric temperature conditions, it is shifted to the left, thereby releasing  $\text{NO}_x$  that can readily enter the  $\text{O}_3$  formation cycle even in remote regions.

## 1.2 The Phenomenon of Lightning

The phenomenon of lightning has long been present in the Earth's atmosphere, perhaps since its formation. Due to its fast, striking and violent nature, lightning, and its audible manifestation, thunder, have both fascinated and instilled respect and fear in man, as evidenced by the innumerable records of the phenomenon that have made their way into mankind's religion and mythology records, where it has been associated with the wrath of the gods. Numerous deities in mythology have been depicted either carrying or hurling thunderbolts; In India, the ancient Vedic books described how Indra carried thunderbolts in his chariot. Buddha has been depicted carrying thunderbolts with arrowheads on their ends. The God Seth of ancient Egypt used to hurl thunderbolts. The ancient Greeks viewed lightning as a punishment sent by Zeus. Some native-American tribes believed that lightning was caused by the flashing wings of the mythical "*thunderbird*", whereas thunder came from the rubbing of its wings. In northern European mythology the god Thor produced lightning as his hammer pounded his

anvil while he rode his chariot through thunder clouds.

In our everyday life, lightning has made its way into the names given to the days of the week in different cultures: In German, *Donnerstag* is the day of thunder, as is *Giovedì* in Italian .

Even today, with the degree of understanding we have of the phenomenon, it is undeniable that it is still able to fascinate and capture our imagination. Part of this impression that lightning has left through history is due to its potential to destroy life; a direct strike can kill a person and, though numbers are hard to get, more than thousand people are said to be killed by lightning strikes each year, and probably many more animals are.

Tall man-made structures, such as antennae and tops of buildings are frequently struck by lightning. If not properly connected to earth i.e, “grounded”, sensitive electrical devices can be damaged. Airplanes are also routinely hit by lightning. It is not yet clear whether they intercept naturally-occurring flashes, or whether they initiate them. Uman and Krider (1989) point out that the shape of the aircraft (i.e., the pointy sections thereof, such as the nose, the wingtip and the tail sections) may play a role in enhancing the electric field in clouds beyond its breakdown value.

Lightning can also cause forest fires by striking trees. It has been proposed, however, that lightning-initiated forest fires act as a natural mechanism which keep forests from overpopulation, and thus “healthy”. Lightning tends to hit taller trees which, if burned, may clear space for other smaller, younger trees to grow in their stead.

Lightning also plays a very important role in the maintenance of the Earth’s fair weather electric field. Although far from an ideal conductor, the atmosphere possesses some conductive capability; below approximately 50km, conductivity is mainly due to the presence of ions created by both cosmic rays and the Earth’s natural radioactivity. Small ions, with diameters ranging from 0.1 to 1 nm and lifetimes of about 100 ms are responsible for this. Above 60 km, however, free electrons are the main contributors

to this conductivity. At surface level, the Earth's natural radioactivity and cosmic rays play an equal role in creating these ions; at altitudes above 1 km, however, cosmic rays are mainly responsible for ion production in the Earth's atmosphere. The electrical conductivity of the air at sea level is about  $10^{-14}$  Siemens/m ( 1 Siemens = 1/ohm) and increases rapidly with altitude; at 35 km, where the air density is only 1% of that at the surface, conductivity is about  $10^{-11}$  S/m. About approximately 80 km, however, the conductivity of the atmosphere becomes anisotropic due to the influence of the Earth's magnetic field and the diurnal variations of the solar photoionization processes. This conductivity creates a downward-pointing electric field, the fair weather field, between the electrosphere, at about 60 km of altitude, and the Earth's surface with a value of about 100 V/m at the surface. The magnitude of this field decreases with altitude; at 10km it has a value of about 3% of that at the surface, whereas at 30km it is about 300mV/m and  $1\mu\text{V}/\text{m}$  at about 85km (Rakov and Uman, 2003).

This system can be viewed as a spherical capacitor, with the Earth's surface and the electrosphere as the inner and outer shells, respectively. The integration of the electric field from the surface up to the electrosphere yields a value of about 300kV. In this model, the Earth is negatively charged with a magnitude of approximately  $5 \times 10^5 \text{C}$ , with an equal positive charge distributed throughout the atmosphere. Most of the positive charge is found within the first km from the surface, whereas 90% thereof lies within the first five km from the surface. Because of the Earth's weak conducting capacity, a fair-weather current of about  $2 \times 10^{-12}$  A exists between the shells of this capacitor. At this rate, the charge in the capacitor would be depleted in approximately 10 minutes if there were no mechanism to constantly replenish it. Wilson (1920) was the first to propose that thunderstorms could provide such a mechanism. In this view, thunderstorms can be regarded as the Earth's global generator. An average of the order of 2000 thunderstorms exist at any one time above the surface of the Earth. The current generated by thunderstorms, composed of lightning, corona discharges and precipitation must then balance the fair-weather current. Current from

thunderstorms flows both to the electrosphere (depositing mainly positive charge there) and to the surface of the Earth, depositing mostly negative charge.

Lightning is also an important mechanism whereby nitrogen oxides are produced in nature. Molecular nitrogen and oxygen are dissociated in the hot lightning channel and recombined into nitrogen oxide. The extremely fast cooling of the lightning channel leaves some of the NO “frozen out”. This mechanism will be discussed in more detail in a later section.

The ancient Greeks were familiar with the electrical properties of material objects. By rubbing a small shaft of amber with a piece of wool, they were able to induce an electric field in an otherwise neutral material, which attracted pieces of other materials to it. By the mid 18th century the knowledge of electricity was such that charges were routinely separated and stored in primitive batteries known as Leiden jars. With this background knowledge, Benjamin Franklin proposed an experiment prove that clouds were electrically charged. In his setup, a man was to stand inside a sentry box from which a pointed iron rod was to be placed on top of an insulator and pass through an exit. If clouds were charged, when they passed overhead, the tip of the rod would draw lightning discharges and the man inside the box could draw sparks between the iron rod and a grounded wire. The experiment was successfully performed by the Frenchman Thomas-Francois D'alibard in May 1752 (Uman, 1987).

Franklin himself got to perform a related experiment in a somewhat different way, by flying a kite directly into a storm. The kite took the place of the iron rod, and Franklin was able to make sparks jump from a key tied to the bottom of the kite string to the knuckles of his hand. This experiment proved beyond doubt that clouds were indeed electrically charged and provided Franklin with the necessary knowledge to devise what is perhaps the first practical application derived from the study of lightning: the lightning rod. This device, currently found in practically every tall man-made structure susceptible of being struck by lightning, directs the current

in the flash directly through the ground.

### 1.2.1 The Electrification of Clouds

Lightning can be described as an atmospheric transient electric discharge from the cloud to the ground, or from one region of a cloud to another or between two clouds, or, rarely, from a cloud to a clear air region. Although there have been reports of so-called clear clear-air lightning (though this is most likely lightning that originates from distant thunderstorms and strike areas with clear overhead skies), lightning occurs predominantly in and around thunderstorm clouds. This means that there exist mechanisms whereby these clouds become electrically charged and whose electric field reaches high enough values to result in the dielectric breakdown of the air. The air is ionized and its electric properties changes from that of an insulator to a conductor. Conditions are then set for an electric discharge to occur. In this section, some of the mechanisms of cloud electrification are briefly discussed.

There does not yet seem to be agreement on a single theory as best describing the electrification of clouds. This fact arises in part from the poorly understood physics of static electrification. Compounding the problem is the fact the cloud electrification spans processes of scales across several orders of magnitude, from the molecular and microphysical scales at which the charge separation mechanism takes place, to the scale of thunderstorm clouds.

The processes that lead to clouds being electrified result in the effective separation of cloud charges into at least three distinct regions, usually a positive charge center in the uppermost region of the cloud, a negative charge center below the former and a smaller pocket of positive charge below the negative charge center (Fig. 1.1). This structure has been inferred mostly from in-situ and remote field observations based on the changes in the electric fields that occurs when a lightning discharge takes place. Electrical fields of the order of  $10^5$  V/m are typical between the main positive

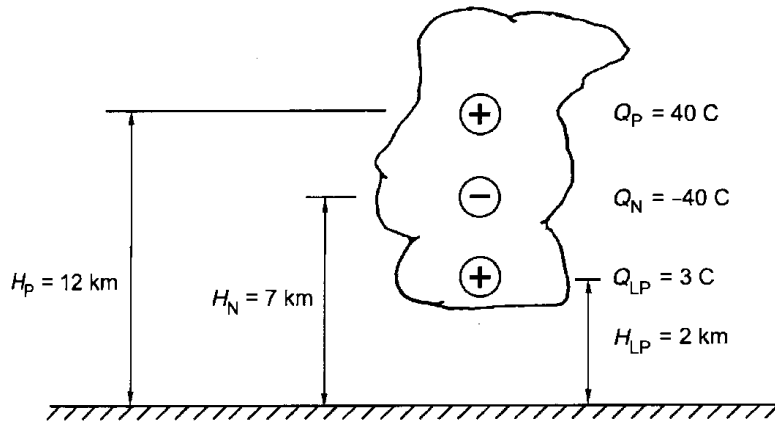


Figure 1.1: Basic representation of the tripole charge structure of a thundercloud. Adopted from Rakov and Uman (2003).

and negative centers of charge in a thunderstorm. It is interesting to note that this value is at least one full order of magnitude below the value of the electrical field intensity,  $3 \times 10^6$  V/m, for electrical breakdown between two parallel plane electrodes at sea level in dry air (Rakov and Uman, 2003). It has been proposed that, in clouds, the large surface curvature of some cloud particles can cause enough local field enhancement and ion emission to initiate large scale breakdown when the electric field is well below the minimum value (Pruppacher and Klett, 1997).

The main center of positive charge is agreed upon as lying above the negative charge center, and most authors point to an altitude range corresponding to a temperature of  $-20^\circ\text{C}$  and lower. Krehbiel (1986) pointed out that this center of charge tends to be at progressively higher altitudes as tropical thunderstorm progress, increasing in time from 10km ( $-30^\circ\text{C}$ ) to 14Km ( $-60^\circ\text{C}$ ).

The negative center of charge is agreed upon by some authors to be localized in a temperature range between  $-15$  and  $-20^\circ\text{C}$  and has been found to essentially remain within that temperature range throughout the lifetime of the storm (Pruppacher and Klett, 1997). On the other hand, Williams (1988) and Saunders (1995) pointed out that this center has been found to generally lie in the temperature range between  $-6$  and  $-15^\circ\text{C}$ , although negative centers as cold as  $-33^\circ\text{C}$  have been reported. Williams (1988) also

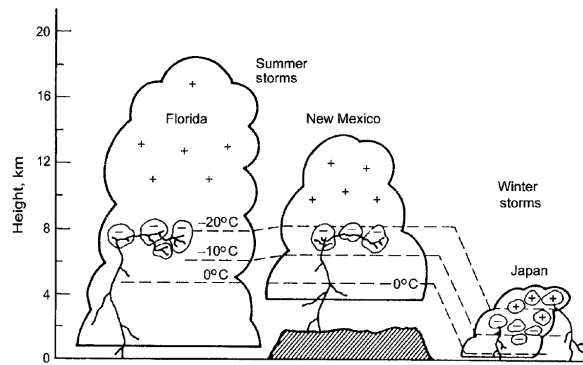


Figure 1.2: The location of ground charge sources for summer thunderstorms in New Mexico and Florida and for a winter thunderstorm in Japan, represented by the irregular contour areas. The locations were found using simultaneous measurements of electric field at a number of ground stations. Adopted from Krehbiel (1986).

points out this center of charge is relatively flat in shape and does not exceed 1km in vertical extent. Rakov and Uman (2003) indicate that this charge center occurs in a layer 1-3 km thick with a lower temperature boundary between 0 and  $-10^{\circ}\text{C}$ . Is it interesting to point out that in the range of temperatures that most authors agree on, water particles in all 3 phases coexist.

Krehbiel (1986) showed, in an interesting comparison, that the negative centers involved in cloud-to-ground flashes are at similar temperature levels in thunderstorms in New Mexico and Florida, despite the fact that the Florida thunderstorms extended well above and below the  $0^{\circ}\text{C}$  level (Fig. 1.2). The negative charge centers for intracloud flashes were also at the same temperature and altitude level. The negative charge centers in winter thunderstorms in Japan were found to be at lower altitude than those of continental US summer thunderstorms, however, they resided at the same temperature levels.

The smaller positive center of charge located below the negative center appears near the  $0^{\circ}\text{C}$  level but is not necessarily related to the melting level (Saunders, 1995). Its origin has been linked to critical a temperature, called the charge reversal temperature, discussed in the theories of cloud electrification below.

A smaller layer of negative charge approximately 100 meters in thickness

above the upper center of positive charge has also been reported (Saunders, 1995). It probably results from negative ions produced above and outside the cloud and then captured by droplets or ice particles. This screening layer of charge is predicted by the convection theory of cloud electrification discussed below.

### 1.2.2 Theories of Cloud Electrification

Two main groups of theories have been proposed to account for the charge separation process and subsequent dipole structure in cumulonimbus clouds; the precipitation theory and the convection theory.

The precipitation theory relies mainly on collisions between mixed-phase hydrometeors in clouds, namely hail, graupel and ice crystals and invokes two different mechanism for the generation of charges, inductive and non-inductive.

The noninductive mechanism concerns the generation of charge from collisions of hydrometeors of different weight, i.e, heavy falling precipitation particles such as hail, interacting with lighter particles, such as ice crystals, carried in updrafts. The originally neutral particles become charged via these interactions resulting in the heavier particles acquiring a negative charge and the lighter particles a positive one. Gravity and updraft will separate these particles carrying the lighter ones to the upper parts of the clouds and the heavier ones towards the bottom thereof, resulting in a positive dipole structure.

One of the mechanism used to explain the charging of the colliding particles is the thermoelectric effect. Consider a rod of ice warmed at one end and cooled at the other; a temperature difference  $\Delta T$  is thus established. Water has a natural tendency to dissociate into into positive H and negative OH ions, and the number of ions increases with increasing temperature; therefore the warmer end of the rod will contain a larger number of ions than the colder end. Both positive and negative ions have a natural

tendency to migrate from regions of high ion concentrations to regions of low ion concentrations. As early as 1958, Eigen and Demaeyer (1958) were able to measure the mobility of ions in an ice rod and discovered that the mobility of positive H ions is at least one order of magnitude higher than that of negative OH ions. Thus, the positive ions migrate much faster to the cold end of the ice rod. This leads to a rapid charge buildup which eventually establishes a steady state condition and a difference of potential  $\Delta V$  between the ends of the ice rod, which in turn prevents further migration of positive ions into that region. Latham and Mason (1961) found the potential difference between the extremes of the rod, expressed in millivolts, to obey the relationship  $V = 1.86\Delta T$ .

Now, what role does this effect play in the charging of super-cooled and ice particles inside clouds? Upon colliding, supercooled water droplets freeze on the surface of heavier, downward-moving hail particles. The latent heat of freezing thus released creates a temperature gradient on the hail particle that results in the riming surface being warmer than the center of the particle. As the hail particle continues its downward motion through the cloud, it collides with ice crystals. The temperature gradient established between the warm outer shell of the hail particle and the cold ice crystals will produce the migration of positive H ions from the riming surface of the hail particle to the cold ice crystals, resulting in a net positively-charged ice crystal and a net negative charge in the hail particle. Gravity and updrafts will separate the charged particles, taking the lighter ice crystals to the top of the cloud and the heavier hail particles to the bottom. The dipole structure is thus formed.

Another theory also invoking the same effect proposes that, upon colliding with hail particles, supercooled water droplets freeze from the outside inwards so, while the core of the droplet is at 0 °C or slightly below, the outer shell is at the ambient temperature, usually well below zero. The temperature gradient leaves the freezing shell charged positively and the still-liquid core negatively charged. As the shell freezes, it expands and parts thereof may shatter, releasing light, positively-charged splinters, and

leaving behind the negatively charged core. Again, gravity and updrafts will separate the lighter splinters and the heavier hail particles.

In the induction mechanism, two originally uncharged, but electrically polarized particles (i.e., with negative charge at the top and positive charge at bottom of the particles induced by the the ambient fair-weather field) collide and the small and lighter hydrometeor picks up the positive charge from the bottom of the larger, heavier particle during the collision (Saunders, 1995). As before, gravity and updraft act to separate the particles to the top and bottom of the cloud creating the dipole structure. The polarization of the particles results from the the alignment of their charges with the fair-weather field, and is reinforced by the charge structure of the cloud itself.

The convective theory of cloud electrification was independently proposed by G. Grenet of the University of Paris in 1947 (Grenet, 1947) and B. Vonnegut of the university of New York at Albany (Vonnegut, 1953). It involves the transport of positive charge generated at the ground by the electric field of sharp objects (a phenomenon known as corona discharges) by convection to the upper portions of the cloud. Upon reaching the top of the cloud, the positive charge will attract negative charge from the air surrounding the cloud (produced by cosmic ray-induced ionization of the air). This negative charge gets trapped by water droplets and ice crystals, forming a “screening layer” of negative charge on the outside of the cloud. Downdrafts will carry air from the outer portions of the cloud downwards toward the surface leading to the formation of the positive dipole structure (Uman, 1987; Saunders, 1995).

Both theories have their shortcomings. As mentioned before, the electrical structure of a cloud is actually more resembling of a tripole than a dipole; there is a very small region or pocket of positive charge at the base of the cloud. The classical precipitation theory does not account for this layer, while the convective theory does by prescribing the convective transport of positive charge from the ground to the base of the cloud. While it was

believed that this flux could account for the lowermost region of positive charge, measurements of the flux indicated it was one order of magnitude too low. Furthermore, the precipitation theory fails, on the account of mixed-phase particle collisions, to explain the electrification of the so-called warm clouds, where only liquid water is present.

More recently, however, a modification of the precipitation theory has been proposed that could explain both the region of positive charge at the base of the cloud and its magnitude. It has been observed that most of the positive particles that fall below the area of negative charge are graupel and ice crystals. It has been found that when such particles collide, the polarity of the charge exchange depends strongly on the temperature of the air in which the collision takes place: below a critical temperature, called the charge reversal temperature, the falling graupel particles acquire a negative charge, whereas above that temperature, typical of the lower, warmer regions of the clouds, positive charge is transferred to the graupel (Jayaratne and Saunders, 1985; Williams, 1988; Wettlaufer and Dash, 2000). Although the exact value of the charge reversal temperature is still in dispute, there is agreement for a range between  $-10$  and  $-20$  °C.

### 1.2.3 The Lightning Discharge

Once the cloud has been electrified and the value of the electric field surpasses the local dielectric strength of the atmosphere, a lightning flash occurs. As in the cloud electrification process, there are many aspects of the microphysics of the lightning discharge that are, at best, poorly understood. In this section, an overview of the what are thought to be the main characteristic of the lightning discharge is given.

As stated earlier, lightning can be divided into flashes that go from the cloud to the ground or vice-versa, which in this work will be referred to as cloud to ground discharges (CG flashes), and flashes that go from one region of the cloud to another and between one cloud and another (hereafter IC flashes). Figure 1.3 gives a broad picture of the different kinds of flashes.

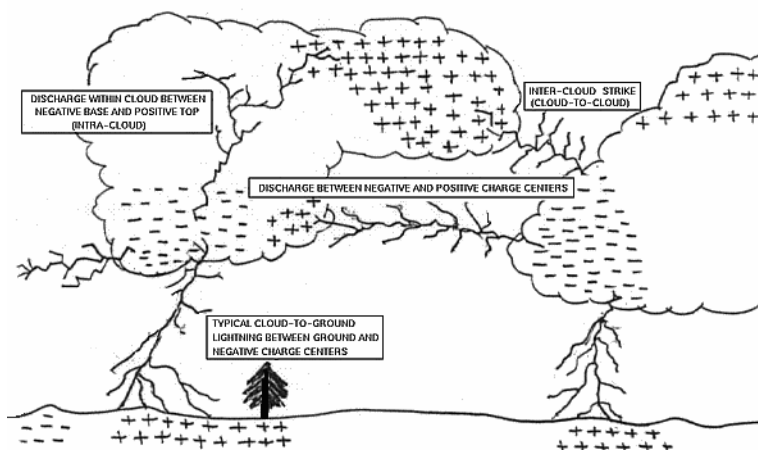


Figure 1.3: Schematic representation of the different types of lightning flashes. Adopted from NASA's Global Hydrology and Climate Center webpage: <http://thunder.msfc.nasa.gov/primer/primer2.html>.

What all have in common is the fact that through them massive amounts of charge, be it positive or negative, are transferred from one region to another (Uman and Krider, 1989).

#### 1.2.4 Negative Cloud to Ground Discharges

Of the cloud to ground flashes, negative CG flashes are the most common, making up close to 90% of cloud-to-ground discharges (Rakov and Uman, 2003). This type of discharge starts in the cloud and lowers some tens of coulombs of negative charge to the ground. The first step in the generation of a flash starts with changes in the electric field in the area of the cloud the flash will emanate from. This initial change in the electric field is called preliminary breakdown and sets the stage for the negative charge to be lowered to the ground. There is no consensus on how this initial phase develops, although one author suggested that it may be a discharge bridging the negative center of charge in the cloud and the small positive pocket of charge at the base thereof (Rakov and Uman, 2003). The initial breakdown seems to last from a few milliseconds to some of tens of milliseconds. Then, an intermittently advancing column of plasma, known as the stepped leader,

starts making its way down from the cloud to ground. As its name indicates, the stepped leader moves in intermittent steps of approximately  $1 \mu\text{s}$  in duration and approximately 10 meters in length, with pauses of 20 to 50  $\mu\text{s}$  between steps. The leader creates a conducting path between the cloud charge source and the ground and deposits tens of coulombs of negative charge from the cloud source along its path in a process lasting on the order of tens of ms and with an average speed of the order of  $2 \times 10^5 \text{ m/sec}$  and currents of the order of 1 kA (Uman, 1987). As the stepped leader moves toward the ground, it branches into the structure commonly seen in lightning flashes. The electric potential at the bottom of the negatively charged leader channel can reach magnitudes in excess of  $10^7$  volts (Uman, 1987). This causes the electric fields at sharp objects on the ground or at irregularities in the ground to exceed the breakdown value of the air and thus one or more upward-moving discharges are initiated from those points and directed toward the incoming stepped leader. When one or more of these discharges make contact with the stepped leader, the leader's tip is connected to ground potential, which marks the beginning of the attachment process. Next, negative charges at the tip of the channel move to the ground, causing large current to flow and the channel near the ground to become ionized and very luminous. This wave of ground potential along the original leader's channel is known as the return stroke, the next phase in the lightning discharge, and is what is perceived as the visible manifestation of lightning. The return stroke propagates upwards through the ionized leader's channel at speeds of the order of  $3\text{-}10 \times 10^7 \text{ m/s}$ , or up to approximately  $1/3$  the speed of light ( $C = 2.998 \times 10^8 \text{ m/s}$ ). At these speeds, the trip of the return stroke to the channel's base takes approximately  $100 \mu\text{s}$  (Uman, 1987). The return stroke serves to neutralize the leader's charge, that is, to transport to the ground the negatives charges stored on the leader's channel and in the cloud source region. Eventually, in a few microseconds, the coulombs of charge that were originally deposited in the leader's channels will have flowed into the ground. The current generated in this process can reach 30 kA, and the rapid release of energy heats the channel leader to temperatures of up to

30000 K and generates the shock waves that eventually becomes thunder. The stepped leader and return stroke processes serve effectively to transport charge from the cloud to the ground. If no more charge is available to the top of the channel, the lightning discharge ends there. If, however, additional charge is made available at the top of the original stepped leader channel, a dart leader may propagate down the original channel. Unlike the stepped leader, the dart leader does not exhibit a step-wise progression towards the ground. Typical speeds for the dart leader are of the order of  $10^6$  m/sec and up to 1 coulomb of charge can be deposited via a current of  $\sim 1$  kA. If further charge is still available at the top of the channel, the dart leader will initiate subsequent return strokes. The time between successive return strokes in a flash is usually in the range of tens of milliseconds but can be as long as tenths of a second. It is the succession of return strokes that give lightning flashes the flickering appearance they sometimes have.

### 1.2.5 Positive Cloud to Ground Discharges

Positive ground flashes lower positive charge to the ground. Though less common than negative CG flashes, they have much higher currents, in the 200-300kA range. Unlike negative CG flashes, the leaders that initiate them are not stepped, but tend to follow a more straight path to the ground and from the positive charge region. Once the leader makes contact with the ground, a single return stroke follows with a continuing current discharge. Positive CG flashes are thought to occur from the main positive charge center of the cloud when it is displaced from the vertical center of the cloud, as in the case of strong wind shear or extended cumulonimbus anvils.

### 1.2.6 Cloud Discharges

The term cloud discharges is oftentimes used to denote three different types of lightning, all of which have in common the fact that they do not make contact with the ground, namely intracloud discharges, those limited to the

confines of the cloud, intercloud discharges, which are the ones occurring between two thunderclouds, and clear air discharges, which take place between a thundercloud and a region of clear air. The term IC, an abbreviation for intracloud flashes or intercloud flashes (or both), is commonly used in the literature to refer to all three discharges mentioned. For simplicity, the term IC flashes will be used throughout this work to refer to cloud discharges.

Although apparently more numerous than cloud to ground discharges, the processes underlying IC flashes are less well known, due in part to the difficulties associated with both obtaining photographic records and directly measuring the current in the charge transfer processes that occur during the discharges. Furthermore, from a practical point of view, IC flashes are less relevant than CG flashes given that they pose a lesser risk to human or wildlife, man-made structures on the ground and forests. As mentioned earlier, aircraft and launch vehicles are susceptible to IC lightning strikes. Rakov and Uman (2003) point out that the sharp angles found in aircraft such as in wingtips and vertical and horizontal stabilizers may enhance the electric field beyond the electric breakdown value and thus trigger a lightning discharge, although the case can also be that the either aircraft or space launch vehicles flying through thunderclouds can intercept already occurring flashes.

IC flashes seem to occur primarily between positive and negative charge centers within clouds (Uman, 1987), and have approximately the same duration as CG discharges, or about 1/2 second. In the process, tens of coulombs of charge are transferred across a distance of the order of 5-10 km. During the discharge process, a continuously-propagating leader generates a series of weak return strokes known as recoil streamers. Weak electric fields, known as K changes, are produced once the leader contacts pockets of charge of sign opposite to its own. Measurements of these electric fields have led to the notion that IC flashes are less energetic than GC flashes (Turman, 1978; Kowalczyk and Bauer, 1982), although some authors such as Gallardo and Cooray (1996), however, do dispute this notion. Determining the energy output of IC flashes is critical for determining the  $\text{NO}_x$  production by

this type of flashes.

### 1.3 Production of Nitrogen Oxide by Lightning

The basic approach used to determine the total amount of  $\text{NO}_x$  produced by lightning flashes, is what Lawrence *et al.* (1995) refers to as the flash-extrapolation approach, or FEA. In this approach,  $G(\text{NO})$ , or the global production of  $\text{NO}_x$  by lightning is defined as:

$$G(\text{NO}) = P(\text{NO})f_f \quad (1.26)$$

where  $P(\text{NO})$  is the production, in molecules of  $\text{NO}$ , by a single flash and  $f_f$  the global flash frequency. This approach rests on the basic assumption that the global production of  $\text{NO}$  by lightning can be characterized by the production of "an average flash". However, energy dissipation in flashes might not be similar, varying instead according to the different type of discharge or even according to the specific part of the discharge. This approach also assumes a good understanding of the worldwide lightning flash distribution and flash frequency, both of which are still uncertain. There are essentially three approaches to determine to determine  $G(\text{NO})$ , namely theoretical, experimental and field-measurement based.

#### 1.3.1 Theoretical Studies

The theoretical study of the formation of nitric oxide ( $\text{NO}$ ) by lightning relies mainly on the Zel'dovitch reactions, originally proposed to explain the formation of  $\text{NO}$  in thermonuclear explosions (Zel'dovitch and Razier, 1966). Above  $\sim 400$  K the following set of reactions take place that lead to an equilibrium state between  $\text{O}$ ,  $\text{NO}$ ,  $\text{N}_2$  and  $\text{O}_2$ :

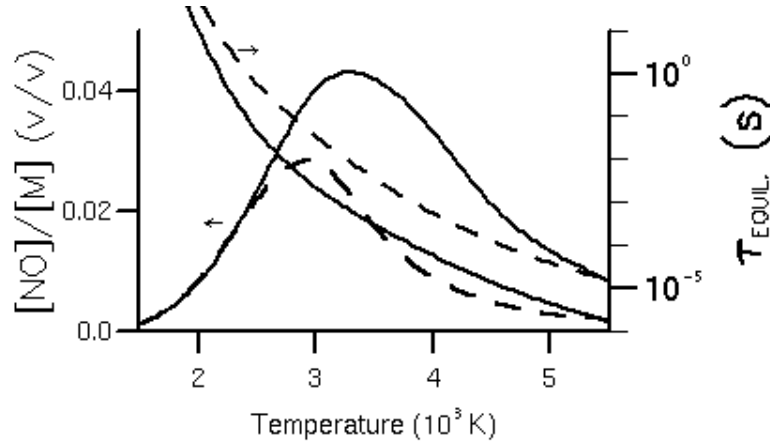
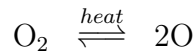


Figure 1.4: Variation of the NO equilibrium mixing ratio and of the time to reach thermodynamic equilibrium ( $\tau_{equil}$ ) with temperature at 500 mbar (solid line) and at 27 mbar (dashed line), from Stark *et al.* (1996).



where eqs. 1.27 through 1.30 are known as the Zel'dovitch reactions.

As in a nuclear explosion, the large release of energy around the discharge channel, where air temperatures in excess of 30000 K can be reached, acts to dissociate molecular oxygen and nitrogen and recombine them into NO. As the temperature rises, the NO thus formed is in thermochemical equilibrium, that is, it is formed and destroyed at the same rate. If the gas temperature were to be kept at thermochemical equilibrium as it cools, the resulting concentration of NO upon reaching ambient temperature would be negligible since, at ambient temperature, its equilibrium concentration

is nearly zero. The thermochemical equilibrium concentration of NO has a strong dependence on temperature, reaching a maximum of about 10% at approximately 4000 K (Lawrence *et al.*, 1995). The time to reach thermochemical equilibrium also exhibits a strong dependence on temperature, increasing exponentially as temperature decreases and ranging from a few  $\mu\text{s}$  at 5000K to approximately one second at 2000K to 1000 years at 1000K, as illustrated in Fig 1.4. The air around the heated discharge channel cools very fast and a temperature is reached where the equilibrium reaction is too slow to maintain the NO concentration in thermochemical equilibrium. Therefore a certain amount of NO is left out of equilibrium concentration or "frozen out". Further cooling of the gas mixtures results in the NO concentration no longer following the thermochemical equilibrium curve below the freeze out temperature (Stark *et al.*, 1996).

The number of NO molecules produced during this process is proportional to the volume of the heated gas mixture heated to the freeze out temperature times the NO concentration at freeze out temperature:

$$[NO]_{freezeout} = [NO]_{equil}(T_{freezeout}) \quad (1.31)$$

While this analysis has been based on the dependency of NO formation by lightning on temperature, Goldenbaum and Dickerson (1993) have suggested that NO is frozen out by a rapid drop in density in the core of the lightning channel, causing the time constant for approach to equilibrium to increase, since the rate of molecular collisions depends both on density and temperature.

### 1.3.2 Experimental Studies

This approach involves the production of NO in laboratory conditions by spark discharges that simulate lightning flashes. Assuming that the NO production is proportional to the discharge energy and that it scales linearly with energy, the results are then extrapolated to obtain  $G(\text{NO})$ . The uncer-

tainties with this method arise from the assumptions made when extrapolating laboratory results to the real-world conditions; Wang *et al.* (1998) found that, at atmospheric pressure, the NO production per unit energy dissipated is not constant, pointing instead to the discharge unit length as a more appropriate parameter. Stark *et al.* (1996) found that parameters such as the gap between the electrodes that produce the simulated lightning spark, the pressure and the electrode size may affect  $P(\text{NO})$ . Goldenbaum and Dickerson (1993) pointed out that there is no simple dependence of the production of  $\text{NO}_x$  on energy density, temperature and air pressure and that further experiments are needed to measure the characteristics of the discharge core in laboratory sparks of the same energy as atmospheric lightning.

### 1.3.3 Field Observations

In this method  $P(\text{NO})$ , or the NO yield per flash is directly measured by measuring the enhancement in  $\text{NO}_x$  in and around thunderstorm clouds. The accuracy of the results depends largely on the detection efficiency of the instruments used in the measurement process. Assumptions need to be made concerning the number of flashes during the storm's life and the energy of each type of flash as well as the NO yield per unit energy. Mixing and detrainment of the air affected from the lightning discharge may be a further source of uncertainty. However, dedicated airborne campaigns, such as EULINOX (<http://www.pa.op.dlr.de/eulinox/start.html>) and TROCCINOX (<http://www.pa.op.dlr.de/troccinox/>) have been able to gather valuable data on  $\text{LtNO}_x$  production.

## 1.4 Objectives of this Study

This study employs a global chemistry and transport model to examine the issue of the production of nitrogen oxides by lightning discharges. To accomplish this objective, an evaluation of the effects of lightning-produced

nitrogen oxides on tropospheric chemistry in general and on the concentration and distribution of other trace gases that affect the production or distribution of  $O_3$  is made. This evaluation is made using the model's current lightning parameterization. The questions this study tries to answer may be summarized as: i) What is the sensitivity of tropospheric chemistry, as reflected in the concentration and distribution of a variety of atmospheric trace gas constituents, to the source of  $NO_x$  from lightning? ii) How do these trace species respond to variations in both the source magnitude and vertical placement of lightning-produced  $NO_x$ ? iii) How good is the current lightning parameterization in MATCH-MPIC and what could be possible paths to explore for improving  $LtNO_x$  parameterizations?

To answer these questions a series of sensitivity runs were carried out, changing mainly parameters related to the production of  $LtNO_x$ . The results of this study have been published in two peer-reviewed journals and presented at international conferences and seminars. The answers to these questions carry the limitations imposed by the assumptions made concerning the source of  $NO_x$  from lightning. I believe, however, that even with these limitations, the assessment of the effects of  $LtNO_x$  on tropospheric chemistry is an important and worthwhile undertaking.

Chemistry-transport models have proven to be particularly useful tools in the assessment of the effects of particular parameters on atmospheric chemistry. Despite their limitation, their typical domain ranges make it possible to determine the effects on spatial and temporal scales that would be otherwise impossible with measurements alone. While trying to get a better understanding of the the chemistry of the troposphere, one is found dealing with species whose concentration are very small compared to those of the main constituents of the atmosphere. Furthermore, the effects of these trace components do not exhibit a linear behavior. The chemistry of the troposphere is largely driven by the photooxidation reactions of tropospheric trace gases by the OH radical, that is in turn produced by reactions involving  $O_3$ . One of the main problems of tropospheric chemistry is thus to determine the processes that produce and destroy  $O_3$  as well as those

that affect its temporal and spatial distribution. Since nitrogen oxides are known catalysts of O<sub>3</sub>-producing reactions, it is of key importance to have a properly balanced budget of NO<sub>x</sub>. As mentioned earlier, the source of NO<sub>x</sub> from lightning still has the largest uncertainty of all sources. This fact stems largely from both the complexity and the current degree of understanding of the underlying processes of this source of NO<sub>x</sub>.

### 1.4.1 Outline of this Study

This study is broken down as follows. In this chapter, a brief introduction to tropospheric chemistry, with emphasis on the chemistry of oxidized nitrogen is given. The phenomenon of lightning is described along with the currently accepted theories of cloud electrification. A brief description of the main mechanisms currently accepted to lead to the formation of nitrogen oxides in lightning discharges is also presented.

Chapter 2 briefly describes the computational tool used in this study, the Model of Atmospheric Transport and Chemistry in its Max Planck Institute for Chemistry version, or MATCH-MPIC. The series of sensitivity runs carried out for this study are also described therein.

In Chapter 3 the global horizontal flash distribution of the current parameterization is studied and comparisons with satellite lightning observations are made. The results of the implementation of a lightning parameterization based on convective mass flux are presented.

In Chapter 4, the basic significance of the source of NO<sub>x</sub> from lightning for tropospheric chemistry is examined via the effects on several key tropospheric trace species, namely NO<sub>x</sub>, O<sub>3</sub>, OH, HNO<sub>3</sub> and peroxyacetyl-nitrate (PAN). First, the effects of the source are analyzed by comparing the results of a run with a 5 Tg(N)/yr production rate against a run in which the production of LtNO<sub>x</sub> has been “turned off”. The response of tropospheric chemistry to increases in the source magnitude of LtNO<sub>x</sub>, over the range of uncertainty from 0-20 Tg(N)/yr, is then analyzed. Finally, the model

results are compared against a set of airborne campaign observations.

Chapter 5 examines the effects of the vertical placement of  $\text{LtNO}_x$  on tropospheric chemistry, by analyzing the effects of three different assumptions on the same set of trace species considered in chapter 4.

Chapter 6 gives a summary of the conclusions of this study.

## Chapter 2

# The Model of Atmospheric Transport and Chemistry, Max Planck Institute for Chemistry Version (MATCH-MPIC)

### 2.1 MATCH-MPIC at a Glance

The model used for this study is the Model of Atmospheric Transport and Chemistry, in its Max-Planck Institute for Chemistry version, or MATCH-MPIC. MATCH-MPIC is an off-line chemistry and transport model based on the NCAR CCM (Community Climate Model) (Rasch *et al.*, 1995), which reads in gridded, basic meteorological input, such as temperature, surface pressure, latent and sensible heat fluxes and zonal and meridional winds from a general circulation model or from meteorological analysis and uses these to calculate the remaining meteorological parameters, such as vertical wind velocity, convective mass fluxes, cloud fraction and vertical turbulence. For this study, a vertical structure of 28 levels from the surface in terrain-following sigma coordinates up to approximately 2.7 hPa is used. The horizontal resolution used in this study is T21 or approximately 5.6°

$\times 5.6^\circ$ . The time resolution comprises a 30 minute timestep.

The model consists of two main modules; a meteorological and a photochemical module. In this section, a brief description of the model's main two components, as used for this study, is given.

The equation for tracer density,  $\rho$ , solved in MATCH-MPIC is:

$$\frac{\partial}{\partial t}\rho + \nabla(\rho\vec{v}) = P_{diff} + P_{conv} + P_{em} + P_{wet} + P_{dry} + P_{chem} \quad (2.1)$$

where  $t$  is the time,  $\vec{v}$  is the 3D velocity vector and the P terms represent the physical and chemical process accounted for in the model, namely turbulent diffusion, convection, emissions, wet scavenging, dry deposition and chemical reactions in a set of first order differential equations solved in a sequential manner known as 1st order operator splitting. This method involves using the output of a previous operation as input for the next. Although in nature the different processes represented in the model do not take place in a sequential manner, this method makes the problem of solving coupled integral equations manageable from a computational point of view while allowing separate and independent budgeting of each process.

## 2.2 Meteorology in MATCH-MPIC

### 2.2.1 Advection

Within the context of a chemistry transport model, the term advection refers to the horizontal and vertical transport of trace species by the mean wind components. These winds are driven mainly by pressure gradients within synoptic-scale weather patterns such as frontal systems and are influenced by large scale phenomena such as the Coriolis force. It constitutes the principal means of horizontal redistribution of tracers in the atmosphere, particularly close to large scale atmospheric circulation features such as the

Hadley and Walker cells and the monsoon circulations. (Lawrence, 1996). In MATCH-MPIC this process is simulated via the advection scheme known as SPITFIRE (Split Implementation of Transport Using Flux Integral Representation). The form flux method on which the algorithm is based involves the computation of the changes in tracer density across the grid cell walls of the model's horizontal domain.

### 2.2.2 Convection and Clouds

Convection is the main process responsible for the vertical transport and redistribution of trace gases in the atmosphere. From small scale, localized convection, lasting in the range of minutes, to regional scale features such as thunderstorms, squall lines and hurricanes, to planetary scales, such as the intertropical convergence zone (ITCZ) as a component of the Hadley cell, convection acts to mix atmospheric constituents all the way from the planetary boundary layer (PBL) to the upper reaches of the troposphere and even into the lowermost stratosphere in a matter of hours. Convection is mainly driven by the warming of air masses in contact with the Earth's surface, in turn heated by the incoming solar radiation. Not only does this transport remove trace gases from the places where they are originally produced, but also, upon being transported to the UT, their lifetime can be significantly enhanced if their reaction rates have significant dependencies on temperature. Convection plays a crucial role in the redistribution of energy throughout the atmosphere, mainly from the tropics to the midlatitudes via the ITCZ. Convective precipitation is also responsible for the removal of water- and ice-soluble trace gases from the atmosphere, such as  $\text{HNO}_3$ , thus turning it into an effective sink of reactive nitrogen species (Crutzen and Lawrence, 2000). Thus, the proper treatment of convection is of paramount importance if an accurate representation of atmospheric chemistry is to be made in chemistry transport models, regardless of their scale.

Two schemes are used to parameterize moist convection in MATCH-MPIC; the penetrative deep convection scheme by Zhang and McFarlane

(1995) is used in tandem with the convective adjustment scheme by Hack (1994). The former is based on the simplification of a plume ensemble to a bulk formulation (Lawrence and Rasch, 2005). In the plume ensemble formulation convection is simulated via a collection of convective columns that entrain air throughout their length and detrain only in a thin layer at their tops (updraft) and below the cloud base (downdrafts). The bulk approach simply sums these individual plumes into a single entraining and dissipating plume. The latter scheme then removes any remaining instabilities by the exchange of energy and tracers in neighboring vertical layers, adjusting 3 layers at a time (Hack, 1994).

Cloud fractions are computed using the parameterization by Slingo (1987). Four different types of clouds are represented in the model; low-level stratiform clouds, mid-level layered clouds, high-level cirriform clouds and convective clouds.

The cloud microphysics scheme by Rasch and Kristjánsson (1998) is used to compute condensation and evaporation rates for non-convective clouds. Four different types of condensate are treated in the model: cloud water, cloud ice, rain and snow; however, only the total of them is transported after each timestep.

### 2.2.3 Vertical Turbulent Diffusion

Vertical turbulent diffusion, or the mixing resulting from eddy motions in the lowermost troposphere, constitutes another means of mixing trace gases, particularly in the PBL. Apart from gases, this process also redistributes momentum and energy in that level of the atmosphere. In MATCH-MPIC turbulent diffusion is treated with the non-local scheme by Holtslag and Boville (1993).

## 2.3 Photochemistry in MATCH-MPIC

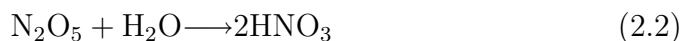
The photochemistry module in MATCH-MPIC was developed to treat those processes affecting the sources, sinks and transformation of atmospheric trace gases, the physical redistribution being dealt with by the meteorology module. This module considers a suite of 141 gas phase reactions of 56 gas species. The species are divided into transported and non-transported, depending on their lifetimes. Those species with lifetimes long enough for the physical redistribution process considered in the model to have an impact on their final concentration are transported; such is the case of trace species such as the  $\text{NO}_x$  family,  $\text{O}_3$ ,  $\text{H}_2\text{O}_2$  and  $\text{HNO}_3$ , among others. It is also interesting to notice that some of the physical redistribution processes considered, such as convection, have an important impact on the lifetime of some of the trace gases treated herein; for instance, the lifetime of  $\text{NO}_x$  in the PBL is the range of a few hours to a day. Once lofted by convection to the UT, its lifetime is of the order of days.

The remainder of the trace gases can be assumed to be in a state of photochemical equilibrium and are thus not subject to transport schemes, which saves considerable computational effort (Lawrence, 1996). Next, the main processes included in the photochemistry module of MATCH-MPIC are briefly described. For further details, the reader is referred to (Lawrence *et al.*, 1999; von Kuhlmann, 2001; von Kuhlmann *et al.*, 2003a,b).

### 2.3.1 Photochemistry Integration

Formerly, the photochemistry integration in MATCH-MPIC was handled using an integration scheme that employed either steady state or backward- or forward-eulerian approximations. More recently however, a new method, the kinetic pre-processor KPP (Damian-Iordache, 1996), which affords a great degree of flexibility in changing the chemical mechanism and adding new species, has been implemented (von Kuhlmann, 2001). The current integration scheme used with KPP in MATCH-MPIC is a linearly implicit,

2-stage Rosenbrock method known as ROS2 (Verwer *et al.*, 1997, 1999). The scheme is mass-conserving. Direct sources are treated as constants, which has the added advantage of reducing numerical instabilities as well as saving computational time. Likewise, species that are transported as families, such as  $\text{NO}_x$ , can be emitted individually, something not possible to do when emissions are treated in a separate operator (von Kuhlmann, 2001). Only one heterogeneous loss process, the hydrolysis of  $\text{N}_2\text{O}_5$  on climatological sulfate and sea-salt aerosols (Dentener and Crutzen, 1993) and on cloud droplets, based on the modeled water liquid content, is included;



### 2.3.2 Photolysis Rates

The scheme used to compute photolysis rates in MATCH-MPIC is from Landgraf and Crutzen (1998). Photolysis rates are computed online every timestep using a method that calculates actinic fluxes at 8 “base” wavelengths for a purely absorbing atmosphere (von Kuhlmann, 2001). Actinic fluxes are computed considering the modeled overhead  $\text{O}_2$  and  $\text{O}_3$  columns, along with clouds and liquid water concentrations from the microphysics and convection schemes.

### 2.3.3 Wet Deposition and Vertical Redistribution by Hydrometeors

Water-soluble species are taken up by hydrometeors and then transported downwards in the atmosphere through gravitational sedimentation. The process can be subdivided into two processes. The first is the uptake of soluble species by hydrometeors with large terminal velocities (i.e. rain drops), a process known as precipitation scavenging. The second process involves the uptake of soluble species by smaller cloud particles generally considered by the model to be non-precipitating, which then nevertheless

sediment quickly enough to be important for some gases. Though this process has been not been consistently considered in most global models, Lawrence and Crutzen (1998) found that its inclusion can have a large impact on the budgets of  $\text{HNO}_3$  and  $\text{H}_2\text{O}_2$ . In both cases, the cloud particles can evaporate before reaching the ground (leading to a virga type of rain in the case of normal precipitation), but if the particles reach the ground, effectively removing the trace gas from the atmosphere, then wet deposition is considered to have occurred.

In both processes, the partitioning of the trace gas between its gas and condensate phase is calculated assuming equilibrium conditions and applying Henry's law. The trace gases' concentrations are followed through the entire length of the model's vertical column and the amounts released or taken up are computed every time step from both the cloud water content and the formation and evaporation rates of precipitation. Further details of the wet deposition scheme used in MATCH-MPIC can be found in Lawrence and Crutzen (1998) and Crutzen and Lawrence (2000)

### 2.3.4 Dry Deposition

Dry deposition can be defined as the removal of species from the atmosphere onto the Earth's surface by means other than precipitation. Usually these means involve turbulence, molecular diffusion and gravitational settling. The flux of a species to the surface can be expressed as a function of the product of its deposition velocity and its concentration in the air:

$$F = -V_d C_a \quad (2.3)$$

Usually, the fluxes and concentrations of a certain species are measured in the field and the deposition velocities to be used in models are then calculated from those two parameters. Deposition velocities can also be calculated by using measured uptake resistances to turbulence, diffusion and surface uptake of a certain species according to:

$$V_d = \frac{1}{r_a + r_b + r_c} \quad (2.4)$$

where  $r_a$ ,  $r_b$  and  $r_c$  are the turbulence, diffusion and surface uptake resistances, respectively. For very soluble species, such as  $\text{HNO}_3$ ,  $r_c = 0$ , so the key resistance parameters controlling its uptake are the resistance to turbulence and diffusion. However, for less soluble species, such as PAN,  $r_c$  can be the determining resistance factor in their uptake.  $r_c$  varies according to the conditions and properties of the surface. The dry deposition scheme in MATCH-MPIC calculates the deposition velocities online based on Eq. 2.4 according to the scheme by Ganzeveld and Lelieveld (1995) and Ganzeveld *et al.* (1998). Resistances for species other than  $\text{O}_3$  and  $\text{NO}_x$  are calculated with formulas from Wesely (1989) based on their solubility.

### 2.3.5 Emissions

Emissions of 16 trace gases, of both natural and anthropogenic origin, are considered in MATCH-MPIC. Among them are nitrogen oxides ( $\text{NO}_x$ ), carbon monoxide (CO) and non-methane volatile organic compounds (NMVOC). A brief description of the main sources follows. For more details, the reader is referred to von Kuhlmann (2001).

#### $\text{NO}_x$ Emissions

Table 2.1 details the emission sources of  $\text{NO}_x$  and their magnitudes in MATCH-MPIC for this study. Industrial emissions account for more than half of the total  $\text{NO}_x$  emissions, and these come primarily from the combustion of fossil fuel in internal combustion engines used both for industrial processes, energy plants and transportation vehicles, including sea-going vessels which have been noted to contribute substantially to the  $\text{NO}_x$  budget, particularly in remote marine areas (Lawrence and Crutzen, 1999), and also include aircraft. These emissions (save for ships and aircraft) are taken

Table 2.1: Nitrogen oxides source estimates, uncertainties and location of emissions in Tg(N)/yr, from Lee *et al.* (1997), and in MATCH-MPIC

| Source                | Emission                | Uncertainty              | MATCH | Location              |
|-----------------------|-------------------------|--------------------------|-------|-----------------------|
| Industrial            | 22                      | 13-31                    | 24.1  | NH, midaltitudes      |
| Biomass burning       | 7.9                     | 3-15                     | 7.8   | Trop, continents      |
| Soils                 | 7.0                     | 4-12                     | 5.5   | Nonpolar cont. sfces. |
| lightning             | 5.0                     | 2-20                     | 4.9   | Trop. troposphere     |
| Transport from strat. | 0.64 (NO <sub>y</sub> ) | 0.4-1 (NO <sub>y</sub> ) | 0.1   | Stratosphere          |
| Ammonia oxidation     | 0.9                     | 0.6                      | -     | Trop. cont. sfces.    |
| Aircraft              | 0.85                    | -                        | 0.45  | Tropop., 30°- 60°N    |
| Total                 | 44                      | 23-81                    | 42.85 |                       |

from the Emission Database for Global Atmospheric Research (EDGAR) (Olivier *et al.*, 1999).

Biomass burning emissions rank as the second largest contributor to the global NO<sub>x</sub> budget. Mostly a result of human activities, most biomass burning takes place in developing nations, particularly along the equatorial belt, although substantial (natural) burning also occurs in Canada and Siberia in summer. Biomass burning emissions in MATCH-MPIC are taken from Galanter *et al.* (2000), and include emissions from the burning of forests, Savannah, fuelwood, agricultural residues, domestic crop residues and dried animal waste (dung).

NO<sub>x</sub> soil emissions are the by-product of bacterial metabolic processes. Interestingly, human activity can indirectly increase these emissions through the application of soil fertilizers. Emissions used in MATCH-MPIC are taken from Yienger and Levy (1995) and obtained from the Global Emissions Inventory Activity (GEIA) database.

Aircraft emissions of NO<sub>x</sub> in MATCH-MPIC total 0.45 Tg(N)/yr. The main sources are over Europe and North America and over the corridor over the north Atlantic ocean connecting both continents. Emissions are the strongest at the cruise altitudes used by jet passenger aircraft, usually in the 10-12km range. In the higher latitudes, this means that the emissions are frequently injected directly into the stratosphere. The distribution for aircraft emissions in MATCH is from Baughcum *et al.* (1994). Ship NO<sub>x</sub>

emissions are from Corbett *et al.* (1999)

$\text{NO}_x$  emissions from lightning are one of the most important natural sources of  $\text{NO}_x$  and, depending on the estimate used can surpass soils as the primary natural source. As mentioned in the introduction, the large uncertainty in the source magnitude stems from the uncertainties associated with the different subprocesses leading up to the production of  $\text{NO}_x$  in and around thunderstorms. In MATCH-MPIC,  $\text{LtNO}_x$  emissions are controlled via the parameterization for the horizontal distribution of lightning by Price and Rind (1992) (PR92 hereafter). PR92 developed a simple lightning parameterization based on cloud top height as a predictor of lightning activity. It has been shown that efficient charge buildup and separation processes are strongly dependent on updraft velocity. Cloud top height has in turn been shown to correlate positively with updraft velocity. This, plus the possibility to readily determine cloud top height from direct satellite measurements, was the basis for choosing it as a first suitable predictor of lightning activity. The parameterized relationship between cloud top height and flash frequency is:

$$F_{land} = 3.44 \times 10^5 H^{4.9} \quad (2.5)$$

$$F_{sea} = 6.4 \times 10^4 H^{1.73} \quad (2.6)$$

with Eqs. 2.5 and 2.6 for continental and marine convective clouds, respectively.  $F$  is the flash frequency (in flashes/min/ $8^\circ \times 10^\circ$  box) and  $H$  is the modeled cloud top height (in km). In the model, cloud top heights are calculated directly from the convection parameterization. The flash rate in the model averages between 60 and 70 flashes/s. From that the global amount of NO is calculated assuming a NO yield of  $1.7 \times 10^{26}$  molec.(N)/flash for a 2Tg(N)/yr production rate. For the higher productions rates used in this study, the NO yield per flash is multiplied by a factor that brings the total NO production to the desired amount. A similar production of NO is assumed for both intracloud and cloud to ground flashes, based on the

assumption that, the CG flashes produce several times more NO per flash than IC flashes, but are much times less frequent. This assumption has not been proved and authors such as Gallardo (1996) dispute it, but do not offer a viable alternative yet. The results of the horizontal distribution of flashes stemming from the parameterization of PR92 will be discussed in more detail in chapter 3 of this work, and the overall role of the source magnitude of  $\text{LtNO}_x$  in chapter 4.

### Vertical Distribution of $\text{LtNO}_x$ in MATCH-MPIC

In previous versions of MATCH-MPIC,  $\text{LtNO}_x$  was input as a uniform volume mixing ratio throughout the vertical convective column. This was chosen based on three assumptions; first, intracloud flashes are much more frequent than cloud to ground flashes (Price and Rind, 1994). Second, cloud to ground discharges were thought to be much more energetic than intracloud discharges (Turman, 1978; Kowalczyk and Bauer, 1982) and third,  $\text{NO}_x$  production by lightning was computed to exhibit a strong dependence on the ambient air density, being less for lower densities (Goldenbaum and Dickerson, 1993). The first two can be regarded as canceling each other out to an extent. The third assumption results in an approximately even mixing ratio (i.e., density-weighted) distribution of the emissions in the vertical. While these assumption are hard to prove or disprove, there is recent evidence that the vertical distribution of  $\text{LtNO}_x$  in deep-convective clouds is likely to be quite different than an even mixing ratio in the vertical. Pickering *et al.* (1998) (subsequently P98) used a cloud-resolving model to determine a set of profiles that typifies the vertical distribution of  $\text{LtNO}_x$  after a convective storm for use in specifying the effective lightning  $\text{NO}_x$  source in global and regional chemistry models. Profiles were computed for three different regimes: tropical continental, marine continental and mid-latitude continental. All three profiles from P98 have been implemented in MATCH-MPIC for this study in their respective regions and, since a midlatitude marine profile was not developed in P98, the midlatitude continental

profile has been adopted for all midlatitude areas, including marine areas. The profiles were scaled (stretched or squeezed in the vertical) to fit the depth of convection in each model column.

A recent study by Zhang *et al.* (2003) has shown that simulations of different storms can lead to qualitatively similar but quantitatively different profiles from P98. Thus, more work is needed to determine the most appropriate assumptions for use in global models. Here we examine the basic sensitivity of the simulated tropospheric chemistry to various assumed profiles of  $\text{LtNO}_x$ , which provides an indication of the degree of importance of refining the knowledge and parameterizations of its vertical placement.

## Emissions of Carbon Monoxide and Other Gases

Carbon monoxide emissions represent approximately 1260 Tg(CO)/yr in the model. Main sources are industrial processes, biomass burning and biogenic activities. Oxidation of NMVOC and  $\text{CH}_4$  represent another 1300 Tg(CO)/yr. The distribution from industrial CO comes from the EDGAR. The biomass distribution is taken from Galanter *et al.* (2000). Emissions from oceans come from Bates *et al.* (1995), obtained from measuring direct measurements in the Pacific ocean.

Emissions of volatile organic compounds, or VOCs, are also considered. These compounds are emitted as a result of industrial, biomass burning and biogenic activities. The industrial emissions of non-methane VOCs (NMVOCs) are from the GEIA database, keeping the specified source strength. Biofuels emissions however, are not considered in the emissions. Methanol is emitted under the category “alcohols” in the EDGAR database using a fixed source strength of 2Tg/yr as per Singh *et al.* (2000), as is acetone ( $\text{CH}_3\text{COCH}_3$ ), where the distribution of ketones was used, scaled to a total production rate of 2Tg/yr.

There is a poor knowledge of the total global emission of biogenic VOCs, except for isoprene, methane, monoterpenes and dimethylsulfide. Emissions

of many of these compounds have been measured under laboratory conditions, but the global emission estimates based on extrapolations of these measurements are highly uncertain (Fall, 1999). Of these compounds, isoprene ( $C_5H_8$ ) is emitted in larger amounts than any other biogenic compound and is the one whose production mechanism in plants is best understood. The distribution of Guenther *et al.* (1995) suggests a production estimate of 503 Tg(C)/yr, however, a production rate of 350Tg(c)/yr is used in the the model, based on the findings of Houweling *et al.* (1998), and previous simulations in MATCH-MPIC (von Kuhlmann, 2001), which showed that computed values using higher emission rates were generally higher than observed values. The distribution is obtained as monthly averages from the GEIA database.

Other NMVOCs accounted for in the model emissions include methanol ( $CH_3OH$ ); the lower limit of the estimates by Singh *et al.* (2000) of  $50 \pm 10$  Tg/yr are used in the model. Ethene ( $C_2H_4$ ), a volatile plant hormone also emitted by as a result of soil activity, is also considered; a source strength of 10 Tg/yr is used in MATCH-MPIC, of which a production of 3 Tg/yr is assumed from soils. Acetone ( $CH_3COCH_3$ ), produced from the decay of plant matter and also directly emitted by plants is considered, with a total source strength of 40 Tg/yr. Emissions of formic acid ( $HCOOH$ ), by both plants and savanna soils are included with a source strength of 5.6 Tg/yr (Bode *et al.*, 1997; Helas and Kesselmeier, 1993). Emission of acetic acid ( $CH_3COOH$ ) are from the same authors; a source strength of 3.14 Tg/yr is used, of which 2 Tg/yr are from vegetation and 1.4 Tg/yr from soils.

Oceanic sources taken into account are emitted with the CO distribution (von Kuhlmann, 2001). There is considerable disparity between different estimates. This arises from the discrepancy between flux estimates derived from measurements of concentrations in sea water and surface air; for example, while Bonsang *et al.* (1988) arrived at an estimate of 52 tg(C)/yr of hydrocarbons from the sea, more recent estimates point toward more moderate fluxes; Plass-Dülmer *et al.* (1995) estimated an upper limit of 5.5 Tg/yr. In the model, the upper 90% limit of the Plass-Dülmer *et al.* (1995)

Table 2.2: MATCH-MPIC runs done for this study

| RUN                 | LtNO <sub>x</sub> production<br>(Tg(N)/yr) | Vertical distribution          |
|---------------------|--|--------------------------------|
| NoLtNO <sub>x</sub> | 0  | Density-weighted <sup>a</sup>  |
| EVEN2               | 2  | Density-weighted <sup>a</sup>  |
| EVEN5               | 5  | Density-weighted <sup>a</sup>  |
| EVEN10              | 10   | Density-weighted <sup>a</sup>  |
| PICK2               | 2  | Pickering et al (1998)         |
| PICK5               | 5  | Pickering et al (1998)         |
| PICK10              | 10   | Pickering et al (1998)         |
| PICK20              | 20   | Pickering et al (1998)         |
| ANVIL2              | 2  | Five uppermost layers of cloud |
| ANVIL5              | 5  | Five uppermost layers of cloud |

<sup>a</sup>Evenly-distributed mixing ratio

estimates is used as a compromise.

## 2.4 Sensitivity Studies

In order to assess the impact of LtNO<sub>x</sub> and its vertical placement on tropospheric chemistry, a set of sensitivity runs was carried out where a number of different assumptions concerning the source strength and the vertical distribution of the lightning NO<sub>x</sub> source were implemented, as summarized in Table 2.2.

First, a run in which the lightning NO<sub>x</sub> source was turned off (NoLtNO<sub>x</sub> run) was carried out. Although a zero LtNO<sub>x</sub> production rate is not realistic, this run serves as a *Gedankenexperiment* to compare other runs to, in order to be able to assess the net impact of the lightning NO<sub>x</sub> source on the model's NO<sub>x</sub> distribution and budget.

Second, a series of runs with various LtNO<sub>x</sub> source magnitudes was done with 3 vertical distributions: 1) a density-weighted distribution as in previous versions of MATCH-MPIC, from cloud top to ground (or cloud bottom

over the oceans), which we will refer to as the EVEN distribution; 2) the distribution according to the vertical profiles developed by Pickering *et al.* (1998), hereafter referred to as the PICK distribution; 3) a distribution in which all of the LtNO<sub>x</sub> is deposited in the five top-most layers of the convective column, intended to represent the upper limit of upward transport of LtNO<sub>x</sub> by convective updrafts which we will call the ANVIL distribution.

The mean vertical profiles of the lightning NO<sub>x</sub> source in MATCH-MPIC based on these three assumptions for a run with a 2 Tg(N)/yr production rate are plotted in Fig. 2.1. The EVEN distribution simulates an even-mixing ratio profile in the vertical, which means decreasing fluxes with altitude, as plotted in all 3 cases. The PICK midlatitude continental distribution deposits the largest amount of LtNO<sub>x</sub> in the LT, more than 100% greater than the EVEN distribution. Interestingly, the fluxes at the surface are nearly twice as large as those at the high altitude peak. In the tropical continental and tropical marine cases, while the PICK distribution still simulates relatively large fluxes at the lower levels, those are  $\sim 15\%$  and  $\sim 60\%$  lower, respectively, than those of the EVEN distribution at the same levels. The ANVIL distribution simulates, as expected, little or no fluxes at the lower levels and peaks at  $\sim 400$  hPa in all three cases. Due to this and the large fluxes of the PICK continental distributions in the LT, the ANVIL distribution values are higher, by over 20%, than the PICK values at high altitudes in these two cases.

Different LtNO<sub>x</sub> source magnitudes, spanning the currently accepted range of uncertainty in the source, were used for these distributions; 2, 5, and 10Tg(N)/yr for the EVEN distribution (hereafter EVEN2, EVEN5 and EVEN10), 2, 5, 10 and 20Tg(N)/yr (hereafter PICK2, PICK5, PICK10 and PICK 20 runs) and 2 and 5 Tg(N)/yr for the ANVIL distribution (ANVIL2 and ANVIL5 runs); the largest source (20Tg(N)/yr), which we consider to be relatively unlikely, was only examined for the “best” vertical distribution (i.e, PICK20). In this study, we will analyze the effects of these different vertical distributions and source magnitudes on NO<sub>x</sub>, O<sub>3</sub>, OH, HNO<sub>3</sub> and peroxyacetyl nitrate (PAN, hereafter). We will focus our discussion on the

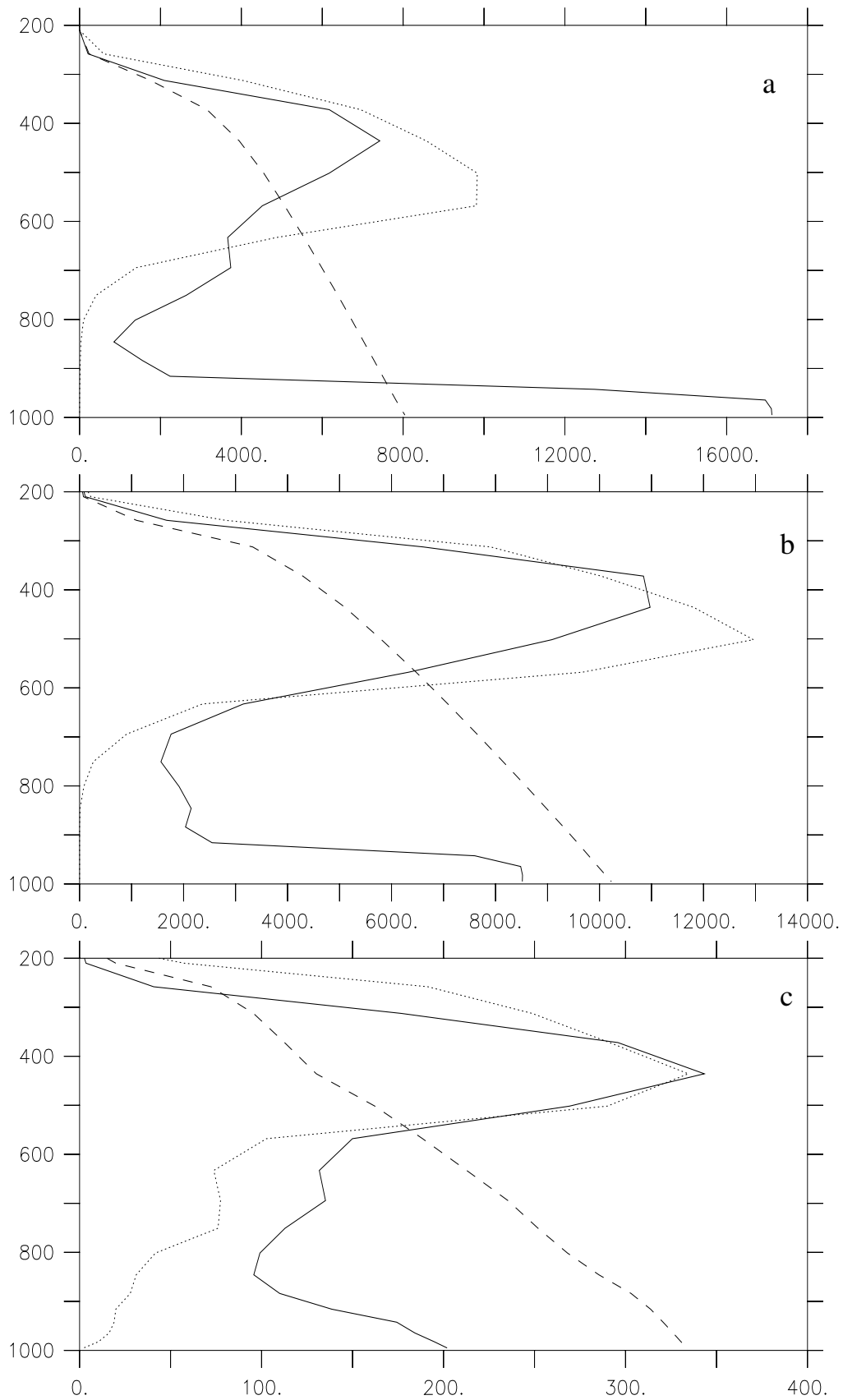


Figure 2.1: Global mean vertical distribution profiles, in  $\text{kg/m}^3/\text{sec}$ , for the three vertical distributions in this study, PICK (solid line), ANVIL (dotted line) and EVEN (dashed line), for the PICK distribution's three cases: a) midlatitude continental, b) tropical continental and c) tropical marine (bottom). Vertical axis scale in hPa.

PICK5 run, since it best reflects the currently accepted estimate for  $\text{LtNO}_x$  and the most physically-based vertical distribution in the literature.



## Chapter 3

# Horizontal Distribution of Modeled Lightning in MATCH-MPIC

One of the most critical parameters in assessing the impact of lightning-produced nitrogen oxides in tropospheric chemistry is the global horizontal distribution of lightning. The questions of the prevalence of lightning, its distribution between continents and sea, its variability in coastal areas and its seasonal variability are such that their answers are critical in determining an accurate budget of  $\text{LtNO}_x$ , and thus of  $\text{O}_3$ . Unfortunately, the scientific community is not currently in a position to give positive, detailed answers to this questions. However, with the advent of high quality space-borne lightning detecting sensors, a clearer picture of the global horizontal distribution of lightning is starting to emerge, making it possible to asses the performance of the lightning parameterizations currently in use in global models. In this chapter, the global flash distribution resulting from the Price and Rind (1992) cloud-top height lightning parameterization in MATCH-MPIC is assessed by comparing the modeled flash distribution with a satellite observations. Furthermore, the results of the implementation of a recently-developed lightning parameterization based on convective mass fluxes in MATCH-MPIC are discussed.

### 3.1 The Optical Transient Detector and the Lightning Imaging Sensor

With the launch of the MicroLab 1 (later renamed OV-1) satellite in April 1995, a new era in lightning research was ushered in. Onboard the satellite was a payload specifically designed and built to observe and record flash activity from low Earth orbit. That instrument was the Optical Transient Detector (OTD hereafter). MICROLAB 1 orbited the Earth at an altitude of approximately 740 km with an orbital inclination of  $69.99^\circ$  (Christian *et al.*, 1999).

The OTD sensor assembly comprised three main components; an optical telescope, a charged coupled device array (CCD array) and a narrow-band filter. The fast ( $f/1.6$ ) optical telescope provided a  $75^\circ \times 75^\circ$  angle field of view. The electronics consisted of the focal plane array, or CCD, made up of an array of  $128 \times 128$  elements.

The specific characteristics of the sensor design resulted from the need to optimize the signal-to-noise ratio associated with the occurrence of lightning flashes during daylight conditions, when the background illumination from sunlight reflecting from the cloud tops is much brighter than that produced by lightning. The filter was designed in such a way as to take the maximum advantage of the significant differences in spatial, temporal and spectral characteristics between the lightning signal and the background noise i.e., reflected sunlight (Christian *et al.*, 2003).

The instrument's temporal resolution was 2 ms and its spatial resolution was 6 km at nadir. It had a footprint or viewing area of approximately  $1300 \times 1300$  km during both day and night conditions. Detection efficiency was approximately 50%.

The combination of the satellite's orbital altitude and inclination, along with the sensor's  $10^\circ \times 10^\circ$  field of view, allowed it to record lightning activity between  $75^\circ$  north to  $75^\circ$  south. In a period of a year, most regions of the Earth were viewed approximately 400 times for a period of  $\sim 2$  min.

The OTD Mission ended in March 2000. Although highly successful, it was basically a proof of concept mission for a more sensitive instrument to follow, namely the Lightning Imaging Sensor, or LIS (Christian *et al.*, 1999). The LIS was launched in November 1997 as part of the United States National Aeronautics and Space Administration (NASA) Tropical Rainfall Measuring Mission satellite, or TRMM. TRMM orbits the Earth at an altitude of 350 km with an orbital inclination of  $35^\circ$ , which allows it to observe lightning activity primarily over the tropical regions. The basic layout of the instrument is similar to that of the OTD, although its sensitivity is greater, allowing for a spatial resolution of 3 km at nadir, while maintaining the same temporal resolution. The detection efficiency is close to 90%.

Neither instrument is able to discriminate between CG and IC flashes, detecting total or “bulk” lightning while surveying an individual storm for approximately 90 seconds as the satellite passes overhead.

For the purpose of evaluation of MATCH-MPIC’s lightning parameterization, the LIS/OTD 2.5 degree Low Resolution Time Series (LRTS), provided by NASA’s Global Hydrology and Climate Center (GHCC), was used. The product is a  $2.5^\circ \times 2.5^\circ$  gridded composite of daily time-series of total (IC+CG) lightning, expressed in flashes/km<sup>2</sup>/day. Individual time series are included from the 5 year OTD (4/95-3/00) and 5 year LIS (12/97-2/03) missions, as well as a combined OTD+LIS product. Lowpass temporal filtering (110-day for OTD, and 98-day for LIS, 110-day for combined) yielding approximately 3-month windows, and spatial moving average filtering (7.5 deg) have been applied, as well as best available detection efficiency corrections and instrument cross-normalizations.

The dataset, originally in NASA’s Hierarchical Data Format (HDF), was converted to NETCDF format and gridded to a T21 spatial resolution to match MATCH-MPIC output resolution. In order to make a valid comparison between the observed data and the model output, the yearly flash count in the MATCH-MPIC output was scaled to the value obtained from

the LIS/OTD dataset, approximately 46 flashes/sec.

## 3.2 Comparisons Between Modeled Flash Activity and OTD/LIS Data

Figure 3.1 shows the OTD/ LIS averaged global flash density distributions for 1995-2003 and the 1997 density distributions for OTD and MATCH-MPIC with the PR92 lightning parameterization. Unless otherwise noted and in order to render the flash rates comparable, the bias in the modeled flash distribution has been removed by scaling the simulated annual flash rate to the that OTD, of 48 fl/s. Satellite data for 1997 is only available from the OTD, since the LIS entered service at the end of that year. In order to give a qualitative idea of the observed flash density of that particular year, the top panel of the figure depicts the average flash density of the entire LRTS dataset.

From the satellite data (Fig. 3.1a and b) , it can be seen that, in general, the highest flash densities occur in coastal areas, as well as in tropical continental landmasses. Mountain ranges provide a constant source of heat and therefore spawn thunderstorms on a regular basis. As a result, high flash densities can be observed from the plots in large mountainous regions such as the Alps, the Himalayas and the Andes. According to Christian *et al.* (2003), continental, coastal and island regions contribute 88% of the total global flash production. Landmasses are more effective than oceans at heating the air above them and therefore trigger stronger convection, which in turns leads to a larger mixed phase particle distribution and a more efficient charge separation inside the cloud. In the tropics, flash densities are particularly high over equatorial Africa and South America, the Indian subcontinent, South-East Asia, Indonesia and northern Australia, with densities in the 8-50 flashes/km<sup>2</sup>yr. In Africa, an area encompassing 3 million km<sup>2</sup> known as the Congo basin, shows highest observed flash density, in excess of 50 flashes/km<sup>2</sup>yr. The area is bound on its eastern flank by a

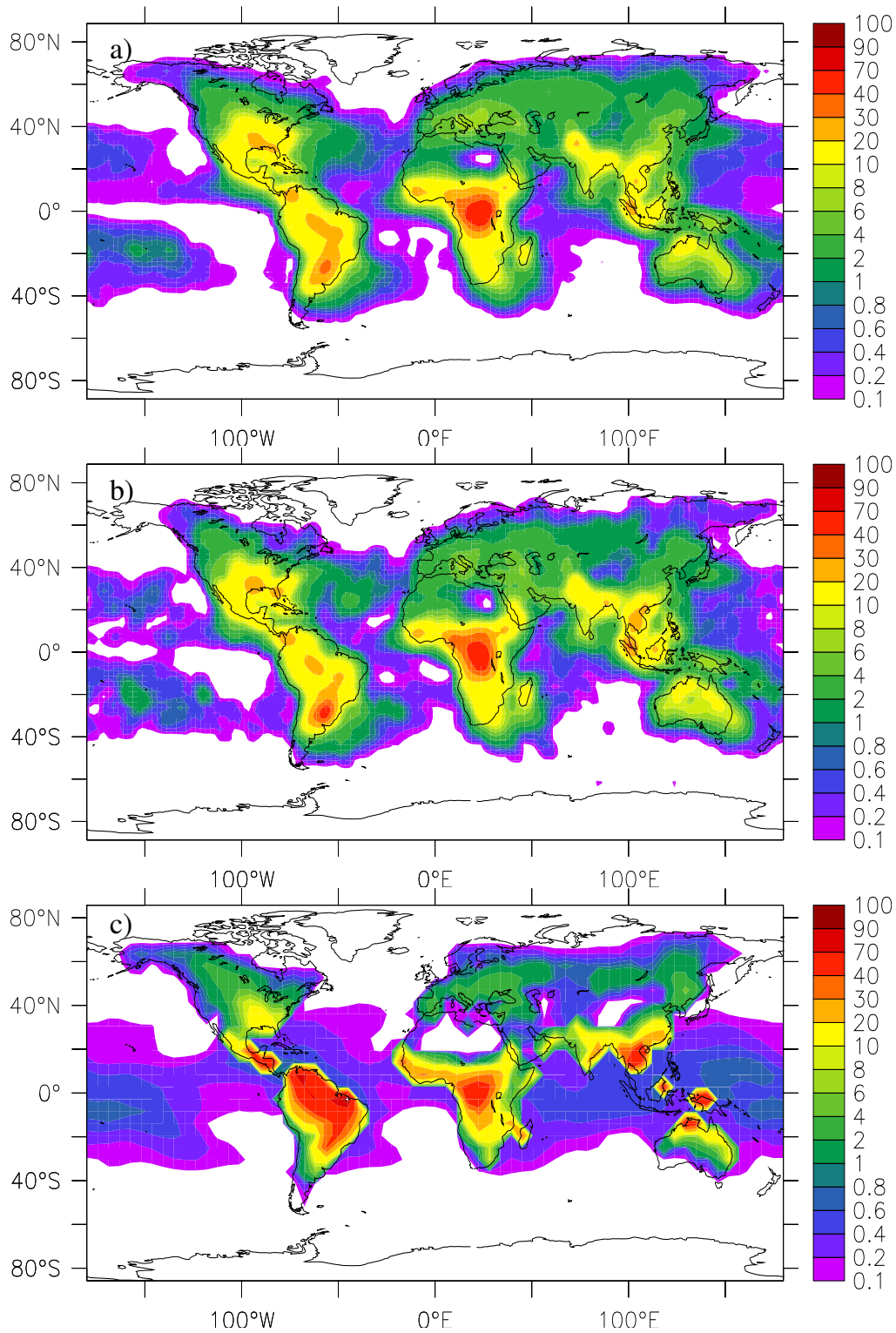


Figure 3.1: Averaged OTD/LIS flash density distribution for the period July 1995–February 2003 (a), and 1997 averaged flash density distribution for OTD (b), and MATCH-MPIC with the Price and Rind (1992) cloudtop height-based lightning parameterization, scaled to OTD's annual flash rate (c). Scale in flashes/km<sup>2</sup>/yr.

north-south running mountain range that blocks low-level moisture air flow from the Indian ocean as well as winds that may induce shear that hinders the development of deep convective towers. Similarly, the mountains may play a role in blocking large maritime cloud-condensation nuclei that may enhance coalescence of large liquid-phase particles. The formation of these particles occur at the expense of smaller ice-phase particles, necessary for an effective charge separation inside the cloud.

In the midlatitudes, high flash densities are observed in the Gulf of Mexico, and the central south and south-eastern United States, with densities comparable to those of the tropical continental areas. This has to do with the inflow of warm, moisture-laden air masses from the gulf of Mexico that encounter synoptic-scale frontal system on their way north, creating unstable conditions and strong convection. The southern and south-eastern U.S. are known for the formation of severe thunderstorms spawning tornadoes. The observed flash densities correlate well with the area of greater storm occurrence. Flash densities are noticeably high along the eastern seaboard of the US, reaching well into the central Atlantic ocean. While there may be development of local storms in these marine areas, a contribution from storms originally formed over the continent or over coastal areas and which then drift off-shore with the prevailing winds is also likely. Western and eastern Europe including the Mediterranean basin, as well as north-western Asia, present a fairly homogeneous flash pattern during the year, averaging from 2 to 6 flashes/km<sup>2</sup>yr.

The Indian subcontinent shows the highest flash densities in its northernmost portion, particularly over the Himalayas and southern portion of Tibetan plateau. This results in part from storm development caused by orographic lifting of the moist air mass coming from the Indian Ocean during the summer monsoon period, although aerosols may also play a role. Southeast Asia and south-eastern China also show high flash densities, also associated with monsoon type of convection.

Over the oceans, lightning is predominant in the north Atlantic and

western Pacific ocean basins all year round where instability is produced when cold air masses pass over relatively warmer waters. Densities are lower in the eastern tropical Pacific and Indian ocean basins, where the overlying airmasses are warmer. However, oceanic lightning densities are generally much lower than those over land. While high marine flash densities are observed in coastal areas, with values comparable to those in continental areas in some cases, densities decrease sharply farther offshore. Examples of this are the westernmost south Atlantic basin, off the coasts of Brazil and Argentina, the central and north Atlantic off the east coast of the US, the southern Indian Ocean off the coast of South Africa and Madagascar and the western south Pacific, off the coasts of Papua-New Guinea and Australia.

Relatively high flash densities far from coastal regions are observed in Polynesia, in the south-central Pacific ocean at approximately  $20^\circ$  south latitude (0.2 to 2 flashes/ $\text{km}^2\text{yr}$ ), in the Hawaii islands in the Pacific ( $\sim 0.4$ - $0.6$  flashes/ $\text{km}^2\text{yr}$ ) and the north-central Atlantic ocean ( $\sim 2$  to 6 flashes/ $\text{km}^2\text{yr}$ )

In general, the flash density pattern over most of the world is well captured by the model's lightning parameterization. As in the observations, flash densities are higher over landmasses, particularly over the tropics, although there is a noticeable trend towards overestimation of the flash activity there, particularly over central and northern South America, Central America, South-East Asia, Borneo and northern Australia, where modeled flash densities are approximately one order of magnitude too high compared with observations. Although not to the same extent, modeled flash activity is also overestimated over the Indian subcontinent, although the annual average is relatively well reproduced. The high flash density feature over the Congo basin in Africa is particularly well reproduced. Towards the mid and high latitudes, however, a tendency to underestimate flash densities becomes evident. Of note is the area of north Africa, where the model mostly simulates densities below scale while observed densities are mostly in the 1-4 flashes/ $\text{km}^2\text{yr}$  range, a factor of 3-4 higher. While the pattern over the south-central and south-eastern US is well simulated, the extent of it is not

well captured; towards the north-west, the simulated densities fall more sharply than the observed ones. The overestimation (underestimation) over tropical (midlatitude) continental areas by the Price and Rind (1992) parameterization can be partly explained by the fact that flash rates during midlatitude continental thunderstorms were found to exceed flash rates during tropical continental storms, despite the fact that the latter have higher cloudtops (Ushio *et al.*, 2001). Price and Rind (1992) developed their parameterization using data for midlatitude continental storms, particularly from the U.S.

Although the general pattern over western and eastern Europe is well simulated, the model clearly underestimates the flash activity over the Mediterranean basin by one order of magnitude. This could prove critical when using the model to assess the concentration of pollutants over that area; higher flash densities than simulated may result in lower simulated  $\text{NO}_x$  and  $\text{O}_3$  signals over the basin. Likewise, flash densities over most of central and south-central Asia as well as Siberia and westernmost China are also underestimated.

Among the most salient features of the modeled flash activity, is the propensity of the PR92 parameterization to underestimate flash densities over the oceans. This trend is particularly noticeable over the entire Atlantic basin, where modeled flash activities are close to an order of magnitude too low. Activity over the Pacific Ocean is also underestimated, particularly in the western Pacific, in the regions adjacent to major coastlines, such as the coast of eastern Australia and eastern Asia. In the light of the high flash densities observed in coastal areas, this underestimation is one of the weaker points of the Price and Rind (1992) parameterization. The problem near the coasts is due to the fact that, in coastal areas, mixed land-sea gridcells are treated as either land or sea gridcells. This will result in the sharp contrast between flash densities over land and over sea seen in the model data, as opposed to the more gradual shift from continental to marine flash densities seen in the satellite data. Flash activity over Indonesia and the south China sea is underestimated by more than an order of magnitude,

save for specific islands, such as Borneo and Papua-New Guinea, where it is overestimated by approximately a factor of 2. Activity over the Indian ocean is underestimated, although to a lesser extent than in the Atlantic and Pacific oceans.

A final interesting characteristic to note in the observations is the fact that 1997 was an El Niño year. During the last quarter of the year, as well into early 1998, dry conditions in the western Pacific rim sparked strong wildfires in Indonesia, while heavy rains led to floods on the western coast of equatorial South America. This leads to the question of whether typical El Niño conditions are reflected in the flash density distributions. From Fig. 3.1 it can be seen that the yearly averaged flash density distribution pattern for 1997 is remarkably similar to the average of all 8 years for which observations are available; densities in Indonesia, Papua-New Guinea the Philippines and Australia are very approximately the same in both cases. Interestingly, flash densities over Indochina are about a factor of 2 higher for 1997. There is no appreciable difference in the flash density distribution on the western coast of the South or Central America that would indicate stronger convection and increased precipitation associated with the El Niño event that year.

Given that the 1997 El Niño peaked later in the year, a comparison of data for the the September-November period against the average of the same period for the entire LIS/OTD dataset ( Figure 3.2) could highlight features otherwise not discernible in the yearly-averaged plot. Even in that period, the flash density patterns continue to be remarkably similar. Contrary to what may be expected, flash densities over a portion of the Indochina Peninsula, Borneo, and parts of northern Australia, typically affected by drought conditions during El Niño events, are higher by about a factor of 2 compared to the average for the entire dataset. Densities over northern India are also higher than the average for the period.

Using LIS data, Hamid *et al.* (2001) also found that flash numbers over Indonesia were higher during the peak period of the 1997-98 El Niño than

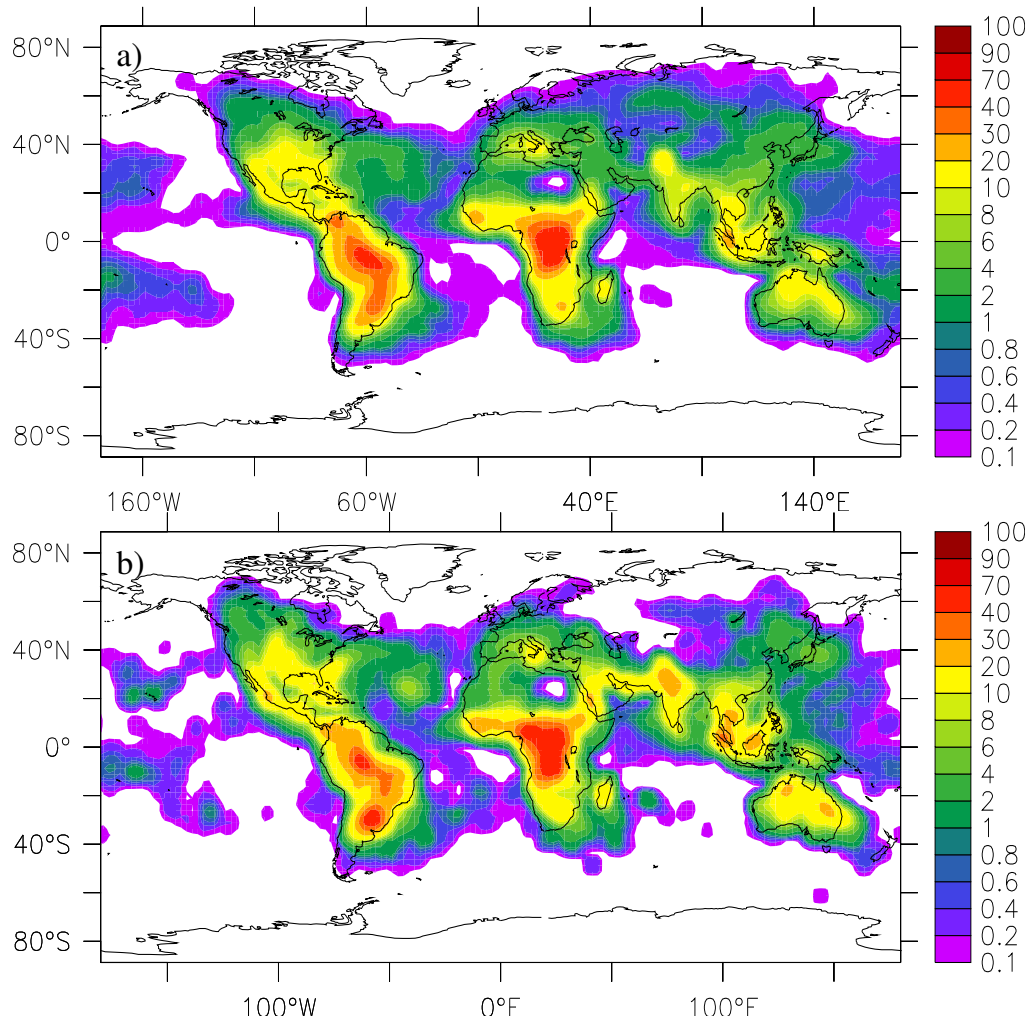


Figure 3.2: Averaged OTD/LIS observed flash density distributions for the SON periods from 1995 to 2002(a), and for SON 1997 (b), in flashes/km<sup>2</sup>/yr.

during the 1999 non-El Niño period. The authors point out that over land and coastal areas during an El Niño event, the number of convective storms decreased while the number of lightning flashes increased compared to a normal, non-El Niño period. Over the oceans, however, the number of convective storms decreased while the number of flashes remained low. Continental storms during an El Niño period were shown to have higher vertical development and thicker ice-phase precipitation zones. Surface air temperatures during an El Niño are higher. Given the strong sensitivity of lightning frequencies to small increases in surface air temperature (Williams, 1992) and that the surface air temperature over tropical lands seems to increase during an El Niño event, then a stronger lightning activity can be expected to occur during the peak phase of an El Niño event. Larger surface air temperatures produce large CAPE which in turn leads to deeper clouds and larger updraft velocities in deep convective events.

On the other hand, there is clear lack of a signal in the flash densities over the eastern Pacific Ocean and the coast of equatorial South America during SON 1997 that could be attributed to El Niño. This opens up the question: does this lack of a signal indicate that the event does not trigger lightning-active thunderstorms in that region?

A few other differences between 1997 and the period between 1997-2003 are in the tropics, where a  $\sim 50\%$  lower flash density at the center of the Congo Basin and a  $\sim 20\%$  higher density in SE Brazil as well as a slightly higher density over the Malay peninsula and SE Asia for 1997 are discernible. In the extratropics, southern Europe and the Mediterranean basin had a lower density in 1997 (50-100%) than the average of the whole dataset.

### 3.2.1 Seasonal Variations

Figure 3.3 shows the seasonally-averaged (DJF: December 1976, January and February 1997; JJA: June, July and August 1997; SON: September, October and November 1997) flash densities for the year 1997 from the

LRTS dataset and MATCH-MPIC. From the figures, it can be seen that flash densities are generally higher in the respective hemisphere spring and summer seasons over land and year round in coastal areas. Over the tropics, the maximum flash activity is modulated by the migration of the Inter Tropical Convergence zone (ITZC).

The tendency of the lightning parameterization to underestimate observed flash densities is particularly noticeable during the DJF period, both over land and over the oceans. While the observed flash densities over the central Atlantic and Pacific Oceans are in the 1-6 and 0.2-4 flashes/km<sup>2</sup>/yr range respectively, modeled densities are in the 0.1 flashes/km<sup>2</sup>/yr or below scale in both oceans. Likewise, densities over southern Europe, the middle East south-central Asia and India, in the 2-8 flashes/km<sup>2</sup>/yr range are severely underestimated. Though the tendency of the parameterization to underestimate midlatitude flash densities is still discernible in the remaining periods, it is not as evident as in the DJF period.

During JJA, midlatitude flash densities in the winter (southern) hemisphere are also underestimated, particularly over Australia, where observed flash densities in the  $\sim$ 0.4-4 flashes/km<sup>2</sup>/yr range are simulated over the western and eastern Australian coasts and where modeled densities are  $\sim$ 0.1-0.4 flashes/km<sup>2</sup>/yr. This may also be linked with the overall tendency of the model to underestimate coastal lightning. Modeled flash densities over South Africa and southern South America for the same period are underestimated as well.

In South America, the highest observed flash densities occur during SON and DJF, coinciding with the ITCZ being positioned over the widest portion of the continent during that period. During MAM and JJA, maximum flash densities over South America show a bipolar mode, with two distinct maxima over northwestern South America, particularly in the Colombian Andes and the Sierra de Santa Marta, and over southeastern South America, close to the Brazil-Argentina-Uruguay borders. Interestingly, the model captures this bi-polar mode flash distribution during the JJA period, although the

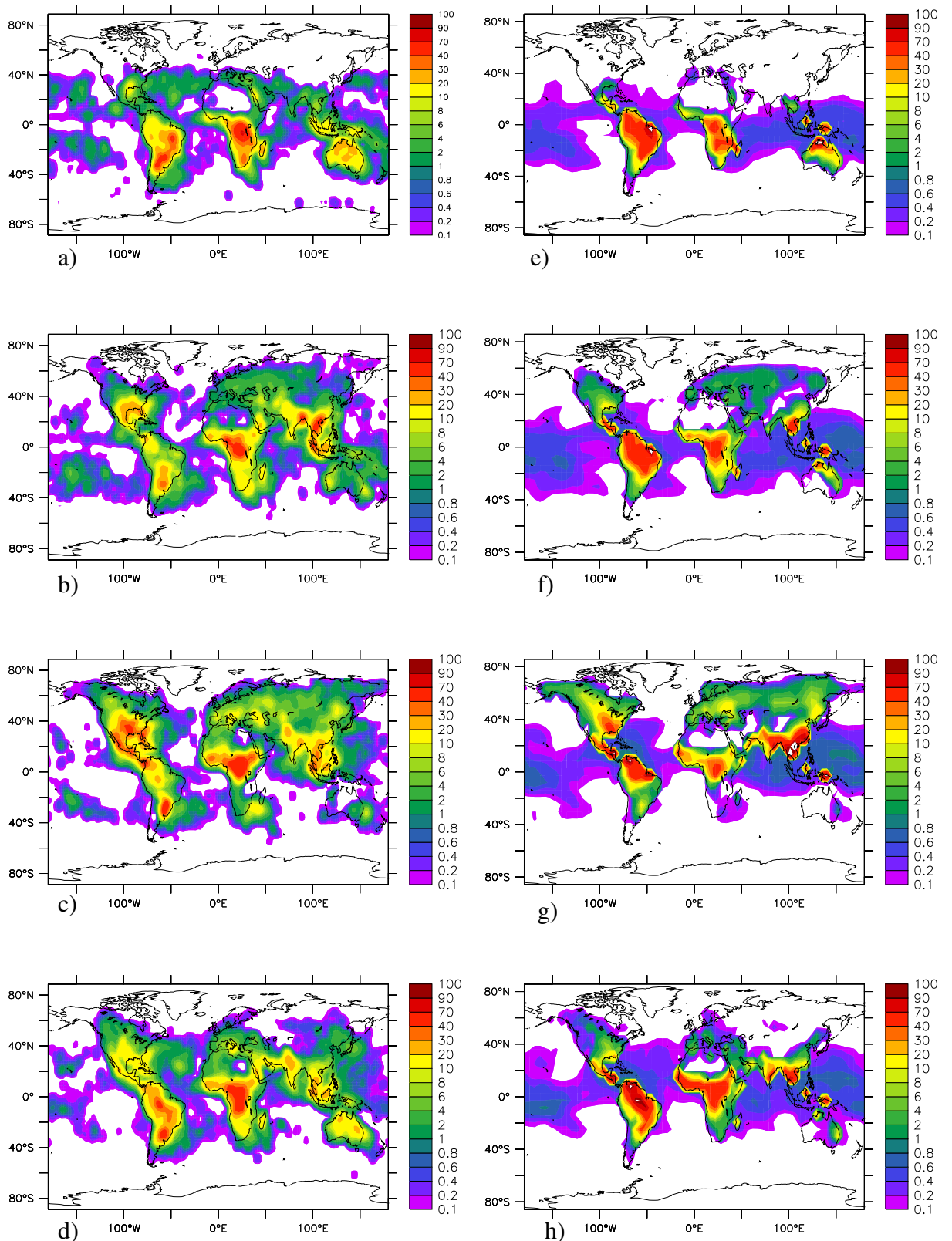


Figure 3.3: Seasonally averaged OTD flash density distribution for DJF (a), MAM (b), JJA (c), and SON (d) 1997, and for the same periods (e-h) for a MATCH-MPIC run with the Price and Rind (1992) cloudtop height-based lightning parameterization and scaled to OTD's flash rate for the respective periods. Scale in flashes/km<sup>2</sup>.yr.

maxima in northern S. America, in the 10-30 fl/km<sup>2</sup>/yr range, is overestimated by approximately a factor of 3. During the MMA period, the feature is not well simulated; instead, large flash densities, of the order of 40-70 fl/km<sup>2</sup>/yr, are simulated in the entire Amazonia.

In the Amazon river basin, the highest flash rates occur during the transitional SON period. According to Boccipio *et al.* (2000) and Petersen and Rutledge (2001), this is associated with synoptic-scale frontal systems making their way northwards into the basin and resulting in stronger, deeper storms with larger vertical velocities and a more developed mixed-phase region with abundant ice particle concentration. Of all the factors modulating flash activity over the Amazon river basin, Petersen *et al.* (2002) cite low-level easterly wind flow (and associated frontal intrusion into the Amazon river basin) to be the most important, since easterly regimes appear to have the highest flash counts. These authors also note that lower flash counts over Amazonia are associated with decreases in CCN concentration and convective available potential energy (CAPE) when regimes are westerly.

Although the Congo basin shows all year-round high flash densities, there is a shift of the maximum flash activity north across the equator around MAM. This is most likely coupled with the migration of the ITCZ, though Barnes and Newton (1982) point out that factors such as synoptic scale forcing (wind, pressure, convergence) and large CAPE values in excess of 2000 J/Kg over equatorial Africa may also play a role. The maximum centers again over equatorial Africa in the JJA period, and moves south during the SON period. The modeled flash densities over the Congo basin are high during all four periods, consistent with the observations. The northward migration of the flash activity in MAM is not well simulated, however, and densities over subsaharan Africa are underestimated in all four periods. Flash densities over Madagascar are well simulated in all four periods, including the peaks in DJF and MAM as well as the decrease, albeit with some degree of underestimation, during JJA and SON. In all four periods, the relatively high densities off the eastern coast of South Africa

and Mozambique, south of Madagascar, in the 1-20 fl/km<sup>2</sup>/yr range, are underestimated by the model by at least one order of magnitude, although the pattern is relatively well captured. This is consistent with the general tendency of the parameterization to underestimate coastal lightning.

It can be seen from the plots that, in contrast with central Africa, flash densities over the Amazonian basin show a marked seasonal variation, with a pronounced minimum in MAM. McCollum *et al.* (2000) identified a series of factors that could account for such differences, among them the fact that African clouds have on average 50% smaller droplet radii, more abundant continental CCN and a lower count of large-size marine CCN (blocked from their origin in the Indian ocean by the mountain range east of the basin), as well as a lower total water vapor column, less precipitable water content, drier sub-cloud air and higher cloud bases.

The integrated annual flash count for the observed flashes for 1997 resulted in 48.49 fl/s, whereas the model's lightning parameterization produced a total of 67.69 fl/s. This represents an overestimate of about 40% with respect to the observed flash rates. On the other hand, the modeled flash annual rate is within 15% of those obtained with the same parameterization by Price and Rind (1994) (77 fl/s), Price *et al.* (1997a,b) (71 fl/s) and Allen and Pickering (2002)(73 fl/s). Price and Rind (1992) compared their modeled flash rates with dawn-dusk averages for January-March 1978 by Turman and Edgar (1982) and obtained flash rates between the the observed 40 and 120 fl/s. The agreement between different models (and thus different convection parameterizations) marks a tendency in the lightning parameterization towards overestimation. Figure 3.4 shows the monthly averaged flash count for 1997 for the OTD and MATCH-MPIC for the 90°S-90°N and 30°S-30°N regions. The observed flash counts shows an annual cycle, wherein flash count peaks in July ( $\sim 56$  fl/sec), and reaches a minimum in January ( $\sim 40$  fl/sec). This is consistent with the flash maxima observed in summer (JJA) in the northern hemisphere, where total landmass surface area is larger compared to the southern hemisphere. The modeled flash count fails overall to capture both the shape and the ampli-

tude of the observed annual cycle, showing instead two distinct maxima, one in about January (anticorrelated with the observed flash count), and another during July-August, which coincides with the observed maximum. On the other hand, the modeled flash counts shows a relative minimum during May-June, not seen in the observations. From Figure 3.4b and 3.3, it can be seen that the main factor modulating the differences between flash patterns is the modeled flash count in the tropics. During DJF, when the observed general activity over the tropics is relatively low, the model overestimates flash densities over north and central South America considerably and over central and South Africa to a smaller extent. On the other hand, it is quite interesting to notice, also from Figure 3.4b, that the maximum in July in the observed flash count is not attributable to the tropics, but to the high flash densities in the northern hemisphere during that month. In the model, however, while activity has increased in the northern hemisphere as well, the tropics contribute significantly to the maximum. From October onwards, the observed flash counts drop as the NH summer draws to a close; the modeled activity, however, keeps increasing until November, when it starts to decrease as well. This is a result of overestimation in the tropics (Fig.3.3 d and e and Fig.3.4b).

Fig. 3.4b indicates that the largest differences between modeled and observed flash count are in the tropics, where the modeled counts are higher almost throughout the year. Largest differences are in the earlier and latter parts of the year. While the observed flash count in the tropics peaks in about October, when activity over the Congo basin is at its peak, the modeled flash count exhibits a cycle not present in the observations. The driving factors for this cycle are the overestimations in South America during DJF, SON and JJA (Fig. 3.3 e, g and h).

Fig. 3.5 shows the the average zonal flash distribution for 1997. It can be seen the observed flash densities peak approximately at the equatorial regions, with two relative maxima at approximately  $40^\circ$  north and south. The two relative maxima correspond to the midlatitude continental areas in the U.S., particularly the south-east (fig.3.1a), and to southern Brazil,

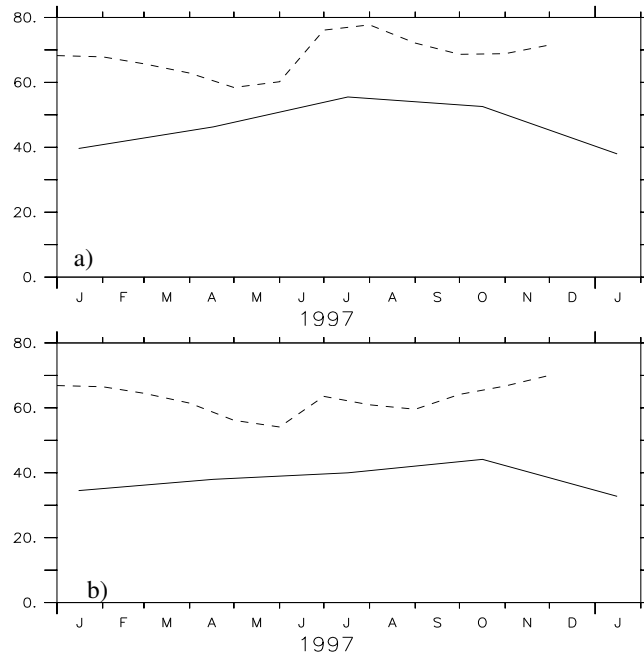


Figure 3.4: Flash rates, in flashes/sec., from the OTD sensor (solid line) and from MATCH-MPIC output, not normalized to OTD’s annual flash rate (dashed line) for the year 1997 for the 90°S-90°N (a) and the 30°S-30°N (right) regions (b).

South Africa and Australia (fig.3.1b). The model flash densities reproduce to an extent this pattern, however, the peak at the equatorial region is significantly more pronounced (about 40%), and the amplitude is considerably smaller. The model simulates peak flash densities exactly over the equator, whereas the observed peak is between 0° and 20° north. The observed distribution shows a much smoother pattern that, while still centered on the tropics, evidences the contribution of the midlatitude continental landmasses.

The yearly averaged meridional density distribution for OTD and MATCH-MPIC scaled to OTD’s count (figs.3.6 a and b) show that, on average, the lightning parameterization does a relatively good job of capturing the general meridional flash pattern. While the over- and underestimates seen in the tropics and midlatitudes, respectively, are seen in this distribution, they are less evident in the global distribution plot (figs.3.6 a). The distribution shows peaks in the the observed densities in the 100° west longitude area,

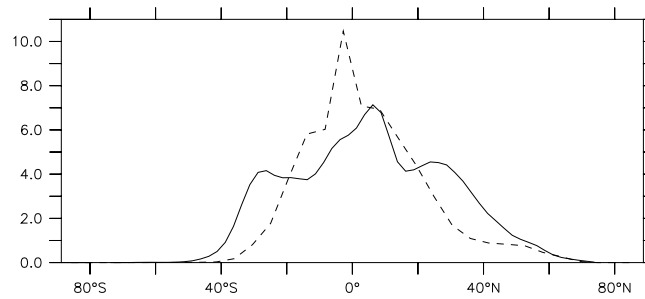


Figure 3.5: 1997 yearly-averaged zonal distribution of flash activity, in flashes/km/yr, for OTD (solid line) and MATCH-MPIC scaled to OTD's flash count (dashed line) for the year 1997.

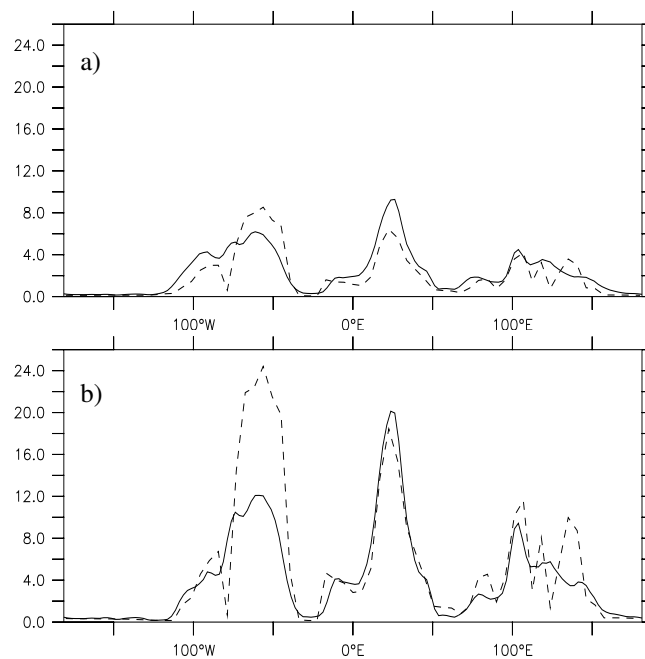


Figure 3.6: 1997 yearly-averaged meridional flash density distributions, in flashes/km/yr, from OTD (solid line) and MATCH-MPIC scaled to OTD's flash count (dashed line) for the 90°S-90°N (a) and 30°S-30°N regions (b)

corresponding to high densities in Central America and the southeastern U.S., as well as in the 50-70° west region, corresponding to the observed peak in SE Brazil and the overall high densities in the Amazon basin (fig.3.1b). Similarly, peaks in the satellite observation are at about 25° east longitude, corresponding to the flash maximum in central South Africa and Europe, and at about 100° east longitude, corresponding to high densities in Southeast Asia. In general the model is able to capture the meridional density distribution reasonably well.

By confining the distribution to the region between 30°N and 30°S (fig.3.6b), however, the discrepancies are more apparent and again, it is possible to see that the major differences lie in the tropical regions. The difference in the peak at 50-80° east is now close to 100%, whereas the differences in the 100-150° west, barely noticeable in the whole globe distribution, now show the model overestimating the densities in that region by as much as 100% as well. Interestingly, the difference in the peak at 25° east is considerably lower, since high densities now are accounted for by densities in central Africa, which the model reproduces much better.

### **3.3 Sensitivity Runs with the Allen and Pickering (2002) Convective Mass Flux Lightning Parameterization**

Given the current availability of accurate and detailed satellite lightning climatologies, one could ask, why not prescribe flash rates in global models based directly on these distributions? Allen and Pickering (2002) point out that such an approach is not advisable, since the production of O<sub>3</sub> varies nonlinearly with the concentrations of its precursors. Since O<sub>3</sub> precursors with low level sources such odd hydrogen (HO<sub>x</sub>) and its precursors are enhanced in regions of upward motion where lightning occurs, it is therefore more sensible to parameterize flash rates in terms of model calculated fields related to convection, such that lightning occurs at the same times and locations as the vertical transport of O<sub>3</sub> precursors. The flash rates are thus dependent on the characteristics of the convection parameterization used.

As a first step towards testing other parameterizations possibilities, the convective mass flux (CMF) -based flash rate parameterization developed by Allen and Pickering (2002) was implemented in MATCH-MPIC and the resulting flash rates were compared with the flash distribution from the

LRTS dataset.

Zipser (1994) pointed out that observations show larger flash rates and vertical velocities in continental storms than in marine storm. This association between large flash rates and strong updrafts is consistent with the notion that the production of lightning is dependent on the amount of mixed-phase particles carried aloft by convective updrafts. Thus, model-calculated CMFs might be useful as a proxy for calculating lightning flash rates.

Allen and Pickering (2002) developed their parameterization by examining the relationship between 1997 observed flash rates from both the U.S. National Lightning Detection Network (NLDN) (Orville and Huffines, 2001) and the U.S. Long Range Flash Network (LRF) (Cramer and Cummins, 1999) and CMF calculated with the Goddard Earth Observing System Data Assimilation System (GEOS DAS) (Schubert *et al.*, 1993) for the area between 10°-60°N and 60°-120°W (equivalent to the continental US). The authors assumed that all the flashes detected by the sensing network are CG. Given that most, but not all of the flashes recorded by the network are CG, this assumption results in a small overestimation of the order of 10% of the CG rate. Time series data for almost all of 1997 the NLDN/LRF flash rate and GEOS DAS-calculated CMF were grouped by surface type (water, land, or either), observation time (0, 06, 12, 18UT or all hours) and seasons (winter, spring, summer and fall). The relationships between flash rates and CMF were investigated by plotting the NLDN/LRF flash rates as a function of the values of the convective parameter. A fourth order polynomial was then fit to all grid points, regardless of land surface, time of day or season:

$$\begin{aligned} \text{LF}_{\text{CG}} &= \nabla x \nabla y (a + bM + cM^2 + dM^3 + eM^4) / A & (3.1) \\ 0 &< M < 9.6 \text{kg/m}^2 \text{min}^1, \end{aligned}$$

where  $LF_{CG}$  is the flash rate in flashes/min for each grid box,  $M$  is the upward cloud mass flux at 0.44 sigma in  $\text{kg/m}^2$ ,  $\nabla x \nabla y$  is the area of each gridbox and  $A$  is the area of a gridbox centered at  $30^\circ\text{N}$ . The value of the coefficients are  $a = -2.34 \times 10^{-02}$ ,  $b = 3.08 \times 10^{-01}$ ,  $c = -7.91 \times 10^{01}$ ,  $d = 5.23 \times 10^{-01}$  and  $e = -3.71 \times 10^{-02}$ .

Despite the limitations imposed by the fact that the lightning parameterization was developed from flash data and CMF fields for the continental US, it was decided that it would be very informative to implement it in MATCH-MPIC and compare the results to those of Allen and Pickering (2002) as well as test it against OTD observed flash densities.

The integrated annual flash count for the CMF-based lightning parameterization implemented in MATCH-MPIC resulted in 188 fl/sec. This is in strong contrast with the result from Allen and Pickering (2002), who obtained 34 fl/s. Apart from CMF, the authors also compared flash distributions from parameterizations based on both cloud-top height and convective precipitation against observed flash rates. In their study, the CMF approach yielded the closest annual flash count (34 fl/s) to that of OTD and was best able to capture the variations and overall shape of the observed distribution. It has to be borne in mind, however, that this parameterization was developed using lightning data from sensor in the continental U.S. and that most likely biases will be present when applying it globally. Figure 3.7 shows the seasonal JJA 1997 flash density distribution for OTD and MATCH-MPIC with the CMF-based lightning parameterization. Figure 3.8 shows the modeled CMF for the run with CMF-based lightning parameterization. It can readily be seen that modeled flash distribution closely follows that of the CMFs. The large differences between observed and modeled flash density distributions in Fig. 3.7 are obvious.

One of the main features is the strong overestimation of marine flash densities, with differences of up to an order of magnitude over large regions such as the Indian Ocean. This can be explained by the fact that, while marine storms have weaker updrafts, they can cover much larger areas than

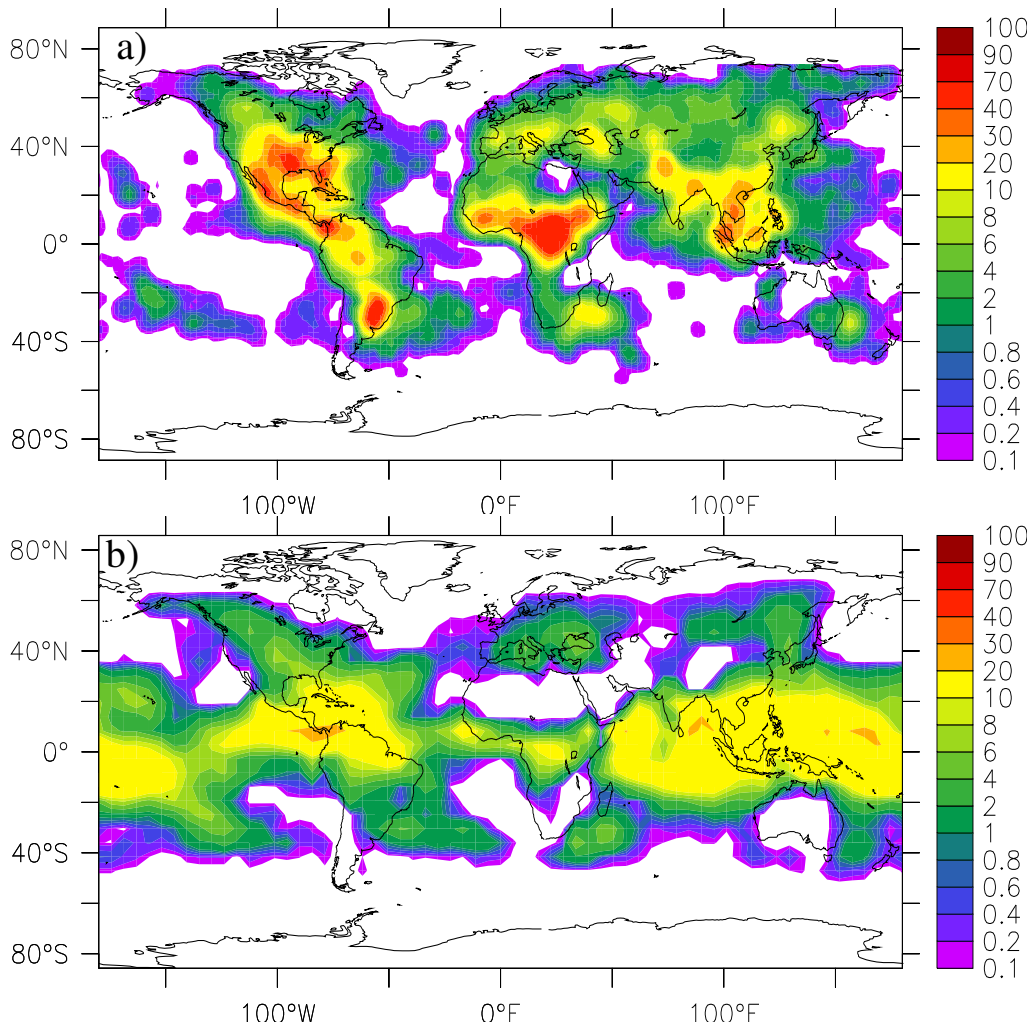


Figure 3.7: Averaged JJA 1997 flash density distribution from the OTD (a), and from MATCH-MPIC with the Allen and Pickering (2002) convective mass fluxes-based lightning parameterization (b). Scale in flashes/km<sup>2</sup>/yr.

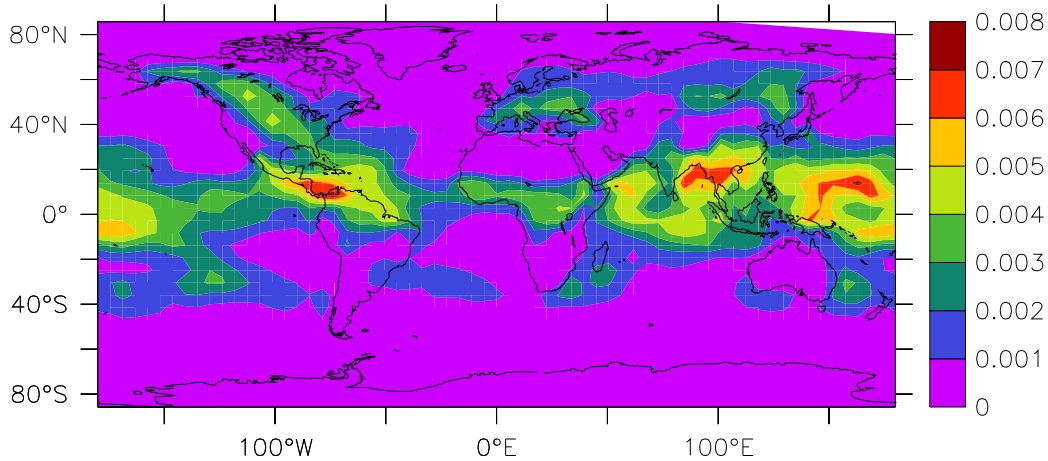


Figure 3.8: Averaged JJA 1997 convective mass fluxes, in  $\text{kg}/\text{m}^2\text{sec}$ , from MATCH-MPIC with the Allen and Pickering (2002) convective mass fluxes lightning parameterization (b). Scale in  $\text{flashes}/\text{km}^2/\text{yr}$ .

continental storms, leading to relatively similar CMFs, and therefore flash densities, over both oceans and land, as seen in the figure. In contrast, the the CMF-based modeled flash distribution underestimates continental flash densities both in midlatitude and tropical regions, again by upwards of a factor of 10 (e.g. South America). Allen and Pickering (2002) found flash densities in Central and South Africa upwards of a factor of 3 too low compared to observations and attributed this to regional differences in the intensity of convection in the tropics as well as to storm cell spacing. It would then be the case that the model's convection parameterization fails to capture these differences. Similarly, the authors also found that marine flash densities were generally overestimated, particularly over the western tropical Pacific, where densities were a full order of magnitude higher than in the observations and higher than those simulated in continental tropical regions, such as the Indian subcontinent. They attributed this to differences in number, spacing and microphysics in marine storms vs. continental storms that the parameterization is unable to reproduce. Apparently, marine storms have weaker updrafts and are spaced farther apart than continental storms. This result underscores the need for separate land and sea lightning parameterization, if CMF is the main parameter being employed.

Allen and Pickering (2002) speculate that better results could be ob-

tained by implementing a hybrid cloud-top height and CMF lightning parameterization. This would help improve the land-sea contrast in the CMF-based parameterization as well as in the cloud-top height based parameterization. Likewise the authors point out that improvements in tropical flash rate distributions will occur as biases in simulated convective fields are reduced. This can be done through advances in modeled physics or assimilation. Due to the additional steps that will apparently be needed to develop a significantly improved parameterization, and to the basic quality of the Price and Rind (1992) parameterization as already shown in this chapter, it has been decided to continue with the scientific studies in the following chapters using the established Price and Rind (1992) parameterization.

## Chapter 4

# Effects of Lightning-Produced Nitrogen Oxides on Tropospheric Chemistry

### 4.1 Basic significance of $\text{LtNO}_x$ for $\text{NO}_x$ and Other Tropospheric Trace Gas Concentrations.

Given the wide range of uncertainty present in the burden of lightning-produced nitrogen oxides, one might ask the question, what kind of effect, if any, does this source of nitrogen have on atmospheric chemistry? How would the burden of trace gases, in particular  $\text{O}_3$ , of which  $\text{NO}_x$  is a direct precursor, and OH, which controls the oxidizing efficiency of the atmosphere, respond to this source? These questions are all the more relevant given that  $\text{LtNO}_x$  is produced in and around thunderstorms, where convection acts to vertically redistribute air in timescales of hours or less, significantly affecting their lifetimes and their potential for long-range transport. In this chapter, the basic significance of lightning-produced  $\text{NO}_x$  on atmospheric chemistry is analyzed. To that end, the effects on a set of tropospheric trace gases

that include NO<sub>x</sub>, O<sub>3</sub>, OH, HNO<sub>3</sub> and PAN are discussed by comparing the enhancements of a run in which LtNO<sub>x</sub> has been “turned off” (NoLtNO<sub>x</sub> run) with the PICK5 run (see Table 1.1), the reference run for this study, with a production rate of 5Tg(N)/yr. Then, the effects of different source magnitudes are investigated by comparing the effects of runs with 2, 5, 10 and 20Tg(N)/yr production rates for LtNO<sub>x</sub> with the NoLtNO<sub>x</sub> run.

#### 4.1.1 Effects on NO<sub>x</sub>

Figs. 4.1 and 4.2 depict the ratios of the seasonal (DJF and JJA 1997) zonal means and seasonal horizontal distributions of the PICK5 vs NoLtNO<sub>x</sub> runs. During both seasons, adding LtNO<sub>x</sub> enhances the UT NO<sub>x</sub> concentrations by a factor of up to 5 during DJF and by a factor of up to 3 during JJA. Most of the enhancement due to LtNO<sub>x</sub> takes place in the tropical mid and upper troposphere during both seasons, approximately between the equator and 40° south during DJF, and between 20° north and south during JJA with a substantial enhancement also in the summer NH midlatitude UT. However, enhancements of 20% with respect to the NoLtNO<sub>x</sub> run are already present at ~900 hPa during DJF between 0° and 20° south and at ~700 hPa during JJA between 0° and 20° north. The latitudinal variation of the maximum tropospheric enhancement in total NO<sub>x</sub> follows the motion of the Inter Tropical Convergence Zone (ITCZ).

The largest enhancements in the tropical upper troposphere (UT) are consistent with lightning activity, which is heavily weighted toward the tropics and continental regions (Christian *et al.*, 2003), especially over equatorial South America, central Africa, and Indonesia. However, as seen in Chapter 3, comparisons with OTD data indicate that the enhancements in NO<sub>x</sub> might be biased high due to a tendency of the lightning parameterization to overestimate flash activity in the tropics, and should in turn be larger over the extratropics. Despite the fact that the PICK5 vertical distribution of LtNO<sub>x</sub> prescribes around 20% of the total LtNO<sub>x</sub> to be released in the first 2km above the continental landmasses, the enhancement there is relatively

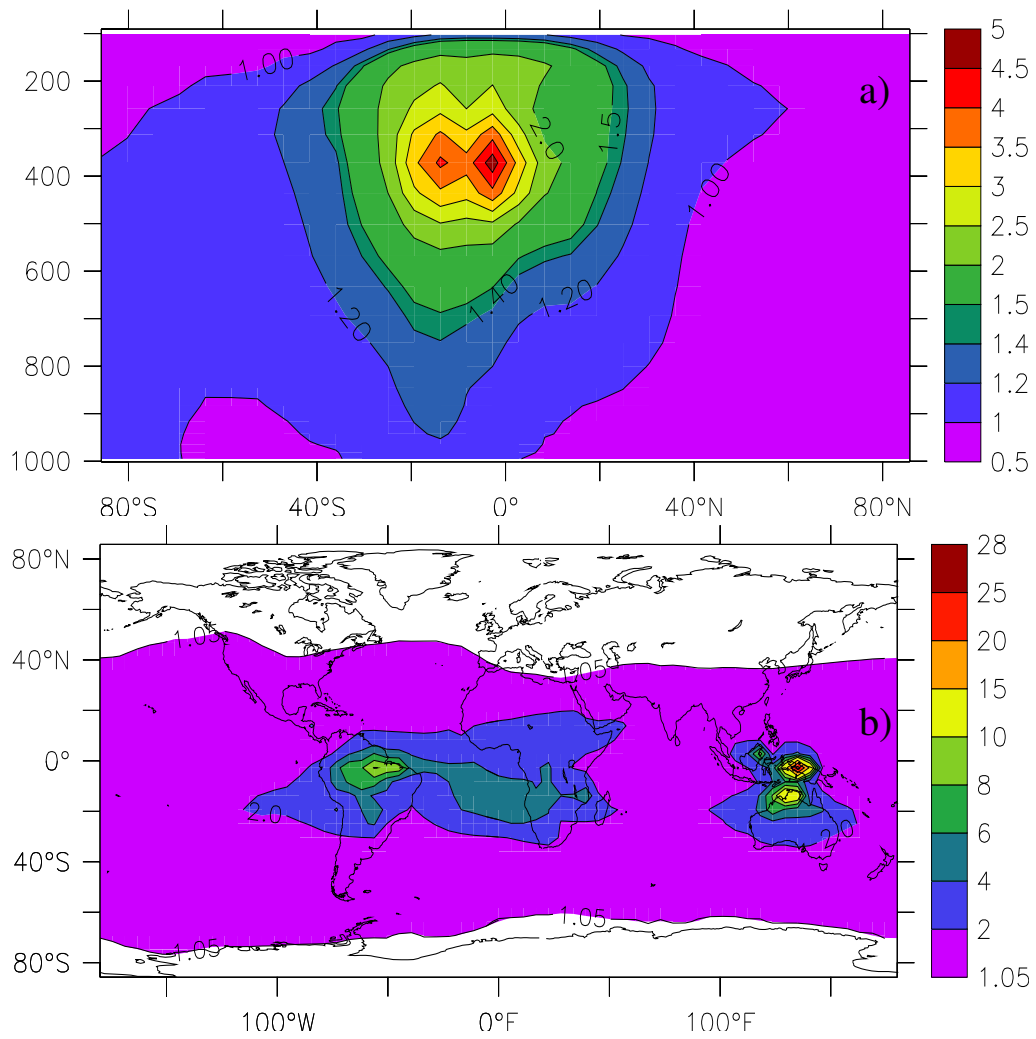


Figure 4.1: Ratio of DJF seasonal zonal means (a) and of the horizontal distributions at 300hPa (b) of  $\text{NO}_x$  for the PICK5 vs. NoLt $\text{NO}_x$  runs.

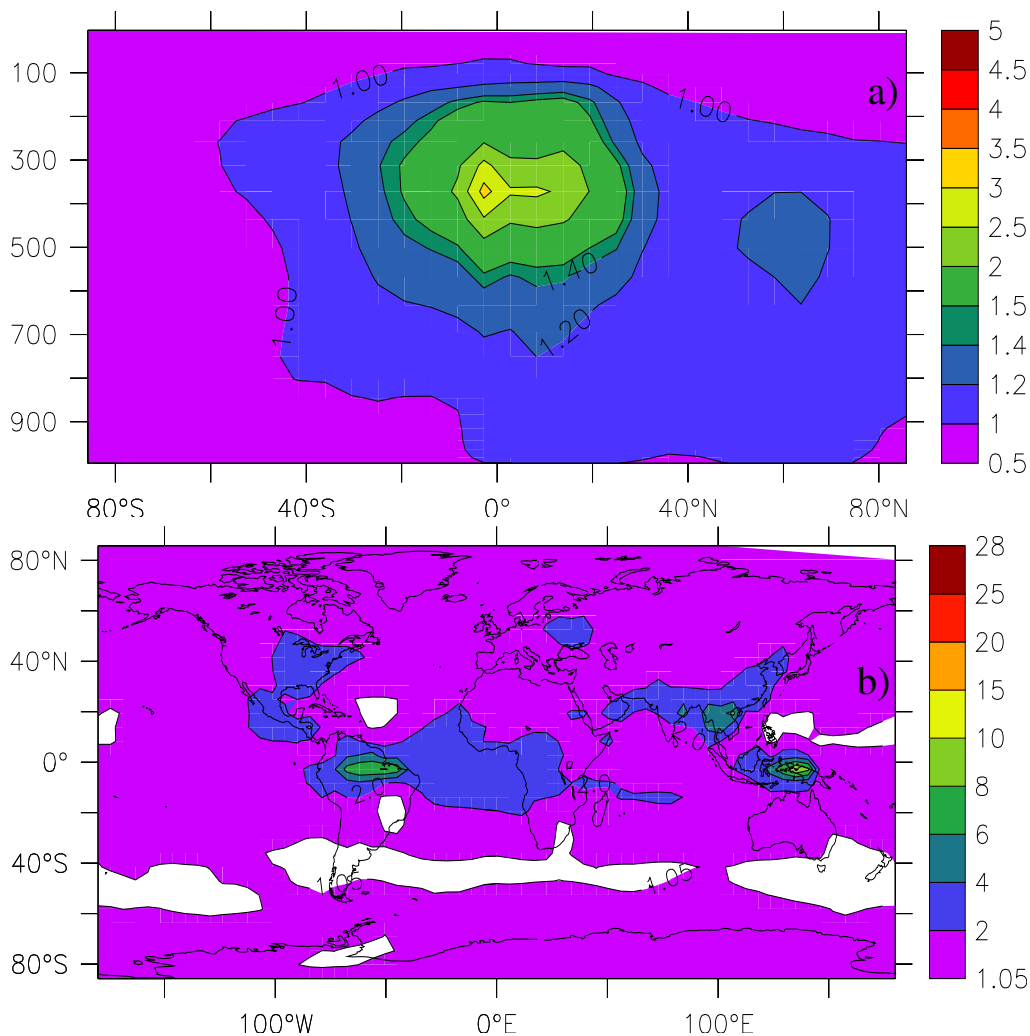


Figure 4.2: Ratio of JJA seasonal zonal mean (a) and of the horizontal distributions (b) at 300hPa of NO<sub>x</sub> for the PICK5 versus NoLtNO<sub>x</sub> runs.

small. This is mainly due to the fact that, near the surface, LtNO<sub>x</sub> must compete against other surface sources, such as soils, biomass burning and urban and industrial fossil fuel burning emissions.

Interestingly, the addition of LtNO<sub>x</sub> causes surface level NO<sub>x</sub> mixing ratios to decrease by  $\sim 5\%$ , throughout much of the extratropics (Fig. 4.3a). Stockwell *et al.* (1999) found the same result, particularly over Europe and North America, and attributed it to increases in OH due to the general increase in O<sub>3</sub> when lightning is included in their model simulations. There are actually two mechanisms to account for the computed NO<sub>x</sub> losses, namely the reaction of OH with NO<sub>2</sub> to form HNO<sub>3</sub> and the conversion of N<sub>2</sub>O<sub>5</sub>

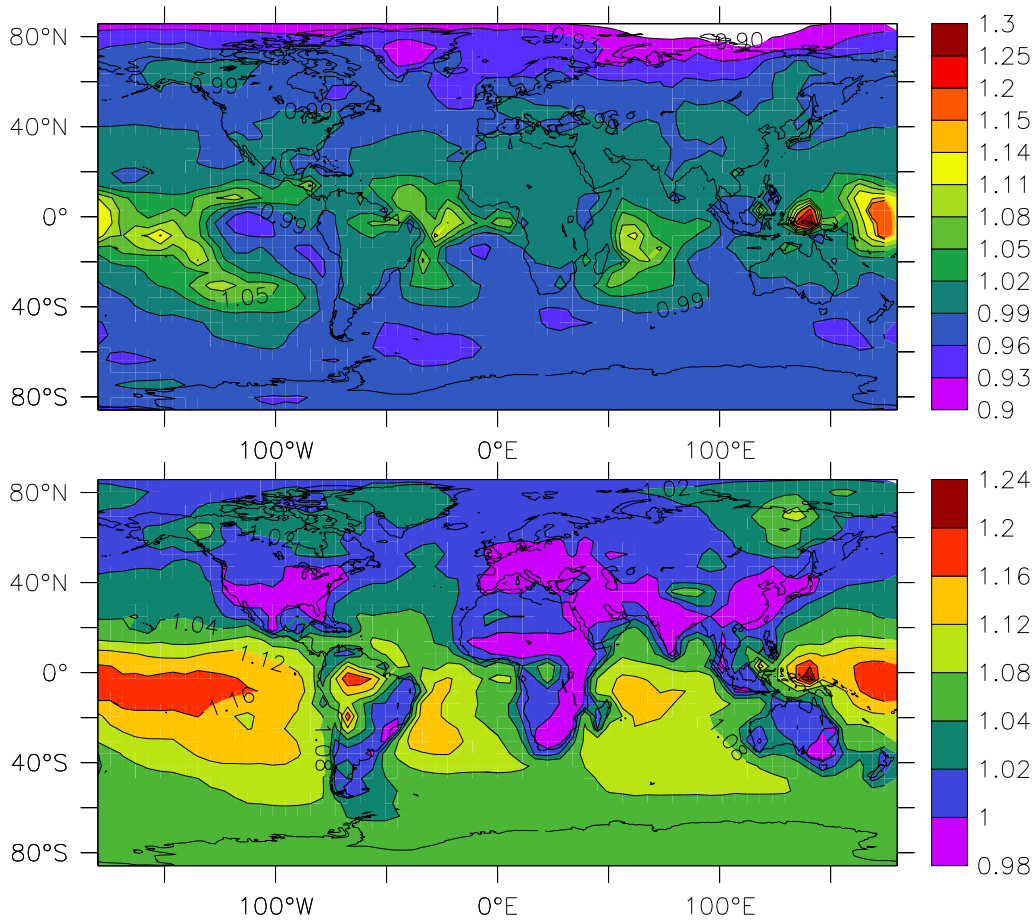


Figure 4.3: Ratios of the annual horizontal distributions at 1000 hPa of NO<sub>x</sub> (top) and OH (bottom) for the PICK5 and NoLtNO<sub>x</sub> runs.

into HNO<sub>3</sub> via hydrolysis on aerosols (Dentener and Crutzen, 1993). Fig. 4.3b shows the annual mean surface ratio of OH for the PICK5 and the NoLtNO<sub>x</sub> runs. A general decrease of  $\sim 1\%$  in surface OH is simulated over most midlatitude and some tropical landmasses when LtNO<sub>x</sub> is included in the simulations, mainly between 50° N and 40° S, rendering the first mechanism unsuitable to explain the loss in those regions (NO<sub>2</sub> levels do increase slightly but not enough to compensate for the decrease in OH).

Stockwell *et al.* (1999)'s explanation can be used to interpret this result outside of that latitude range where, in the simulations, surface OH increases when adding LtNO<sub>x</sub>. On the other hand, wherever there is a decrease in surface OH the negative NO<sub>x</sub> feedback can only be explained by an increase in the NO<sub>x</sub> loss rate via the second loss reaction. This mechanism

depends partly on O<sub>3</sub> levels, which control the formation of NO<sub>3</sub> and therefore N<sub>2</sub>O<sub>5</sub>. An increase in O<sub>3</sub> surface concentration of ~5% is computed for the midlatitude continental areas (Fig.4.3), largely due to downward convective mixing of O<sub>3</sub> produced by LtNO<sub>x</sub> aloft (Lawrence *et al.*, 2003). This enhances the loss of NO<sub>y</sub> via hydrolysis of N<sub>2</sub>O<sub>5</sub>, and ultimately leads to the computed reduction in NO<sub>x</sub> levels.

### 4.1.2 Effects on O<sub>3</sub>

Enhancements in zonal mean O<sub>3</sub> of up to 55% and 40% with respect to the NoLtNO<sub>x</sub> run are simulated during the DJF and JJA, respectively, when LtNO<sub>x</sub> is included in the model calculations (Figs 4.4 and 4.5, top). These enhancements are predominantly in the tropical UT and, in both cases, coincide with the computed NO<sub>x</sub> maxima described above.

Interestingly, O<sub>3</sub> shows a much stronger sensitivity to increases in LtNO<sub>x</sub> in the lower tropical troposphere than in the UT; while the magnitude of the enhancement in the tropical UT is much smaller than that of NO<sub>x</sub> itself, the enhancements in the lower tropical troposphere are comparable (Fig.4.6), with increases of ~20-25% and ~ 10-15% at 900 hPa during DJF and JJA, respectively. On the one hand, this is due to with the low O<sub>3</sub> background levels present in remote areas such as the Amazon river basin in winter and central Africa and parts of Indonesia during summer, which make O<sub>3</sub> particularly sensitive to enhancements in NO<sub>x</sub> compared to polluted areas.

It can also be seen from Fig.4.6 that part of this enhancement, in areas such as the eastern tropical Pacific is the result of transport of O<sub>3</sub> produced in tropical South America. This result underscores the importance of LtNO<sub>x</sub> as an O<sub>3</sub> precursor in remote and pristine regions, particularly in the tropics and the longer lifetime of O<sub>3</sub>, allowing it to be transported further (vertically and horizontally) from the prime source regions of LtNO<sub>x</sub>. Figs. 4.4 and 4.5, bottom, show that the enhancements at 300 hPa, about where the maxima occur, are well correlated with the maximum enhancements in NO<sub>x</sub>, namely, over south-central South America, the equatorial

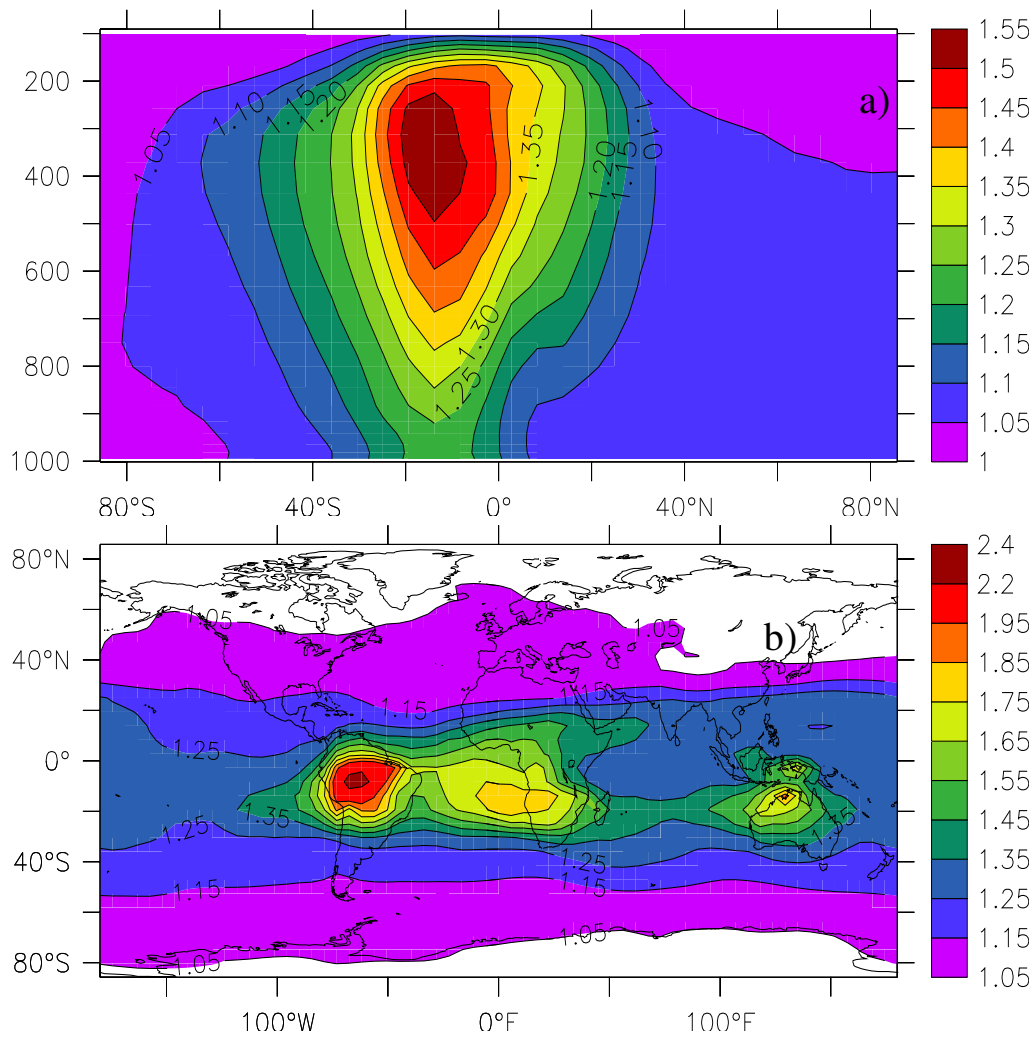


Figure 4.4: Ratio of DJF seasonal zonal means (a) and of the horizontal distributions at 300hPa (b) of  $O_3$  for the PICK5 vs. NoLtNO<sub>x</sub> runs.

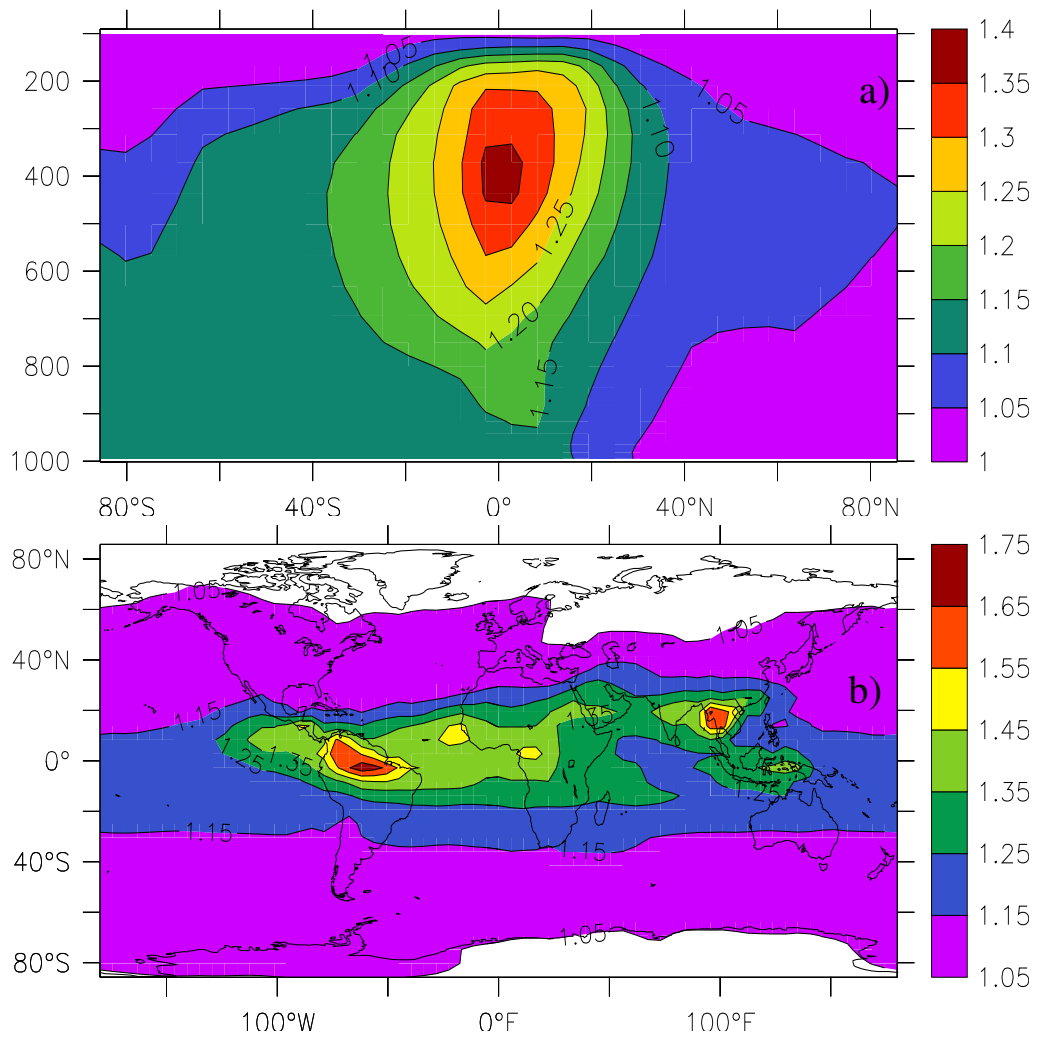


Figure 4.5: Ratio of JJA seasonal zonal means (a) and of the horizontal distributions (b) at 300hPa of O<sub>3</sub> for the PICK5 vs. NoLtNO<sub>x</sub> runs.

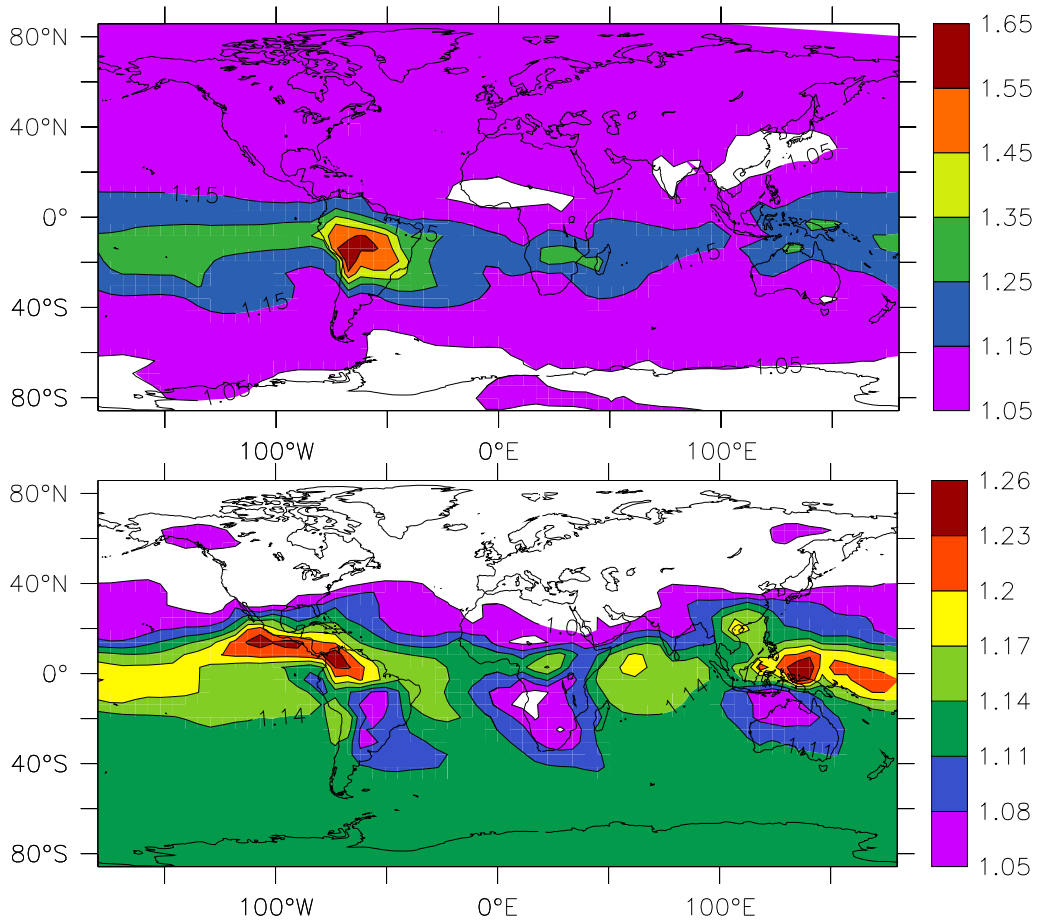


Figure 4.6: Ratio of the seasonal horizontal distribution of  $O_3$  for the PICK5 vs. NoLtNO $_x$  runs for DJF 1997 (top) and for JJA 1997 (top) at 900hPa.

Atlantic ocean, South Africa, northern Australia and southern Indonesia during the DJF, and over equatorial South America, the equatorial Atlantic ocean, equatorial Africa, South-East Asia and Indonesia during JJA, but that the enhancements are spread over larger regions, again due to the longer lifetime of  $O_3$ .

### 4.1.3 Effects on HNO $_3$

There is a very sensitive response of nitric acid (HNO $_3$ ), one of the main reservoirs through which reactive nitrogen is lost (via dry and wet deposition), to LtNO $_x$ . Enhancements of greater than a factor of 7 and 5 with respect to the NoLtNO $_x$  run are simulated during DJF and JJA, respec-

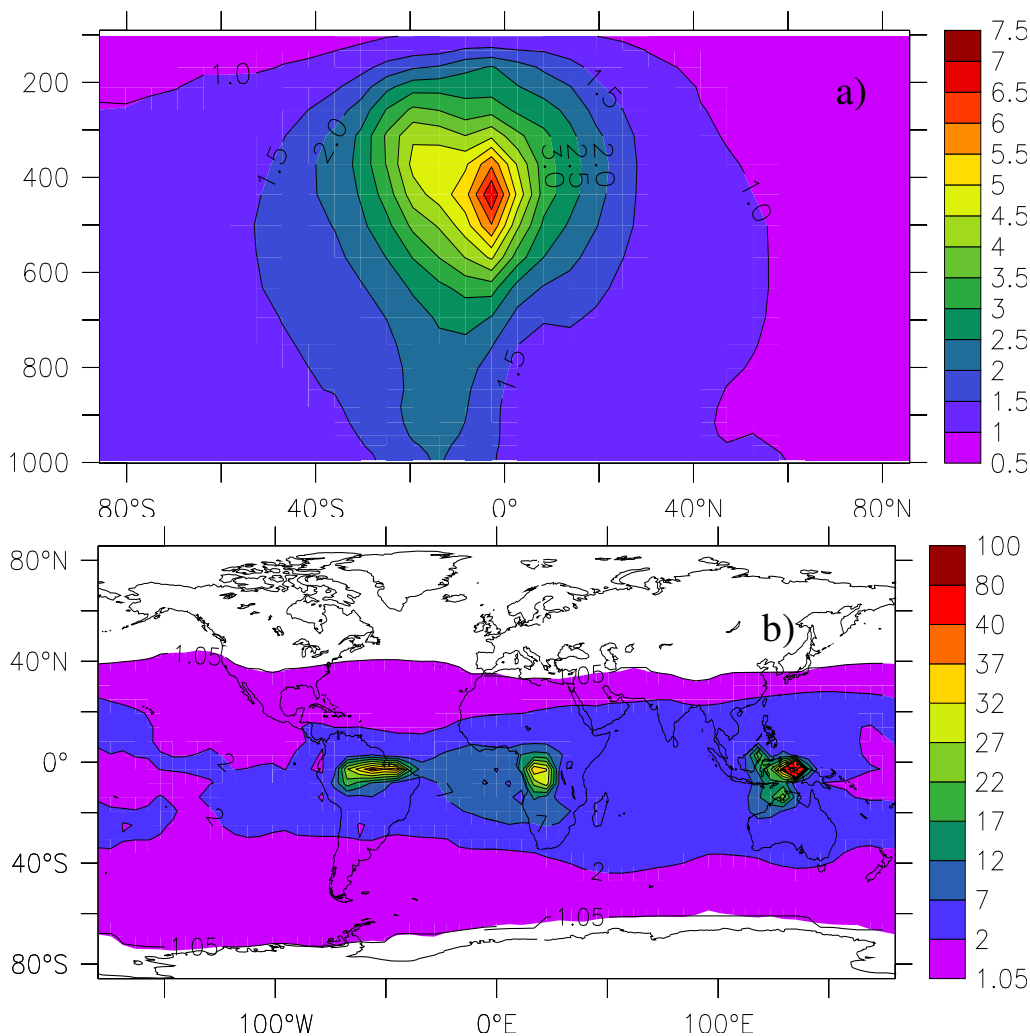


Figure 4.7: Ratio of DJF seasonal zonal means (a) and of the horizontal distributions at 300hPa (b) of  $\text{HNO}_3$  for the PICK5 vs. NoLtNO<sub>x</sub> runs.

tively, as can be seen in Figs. 4.7 and 4.8.

The particularly sensitive response is due to the fact that increases in LtNO<sub>x</sub> result in increases of both NO<sub>2</sub> and OH, two key precursors of nitric acid. Compared to most other trace gases discussed, the maximum enhancements in nitric acid occur at a somewhat lower altitude, i.e., between 400 and 500 hPa in DJF and between 300 and 400 hPa in JJA. Two main reasons account for this fact: first, the enhancement coincides with the maximum absolute enhancement in OH as seen in Fig. 4.13. Second, in the highest part of the UT, there is a buffering effect of PAN, which is enhanced at the expense of HNO<sub>3</sub>.

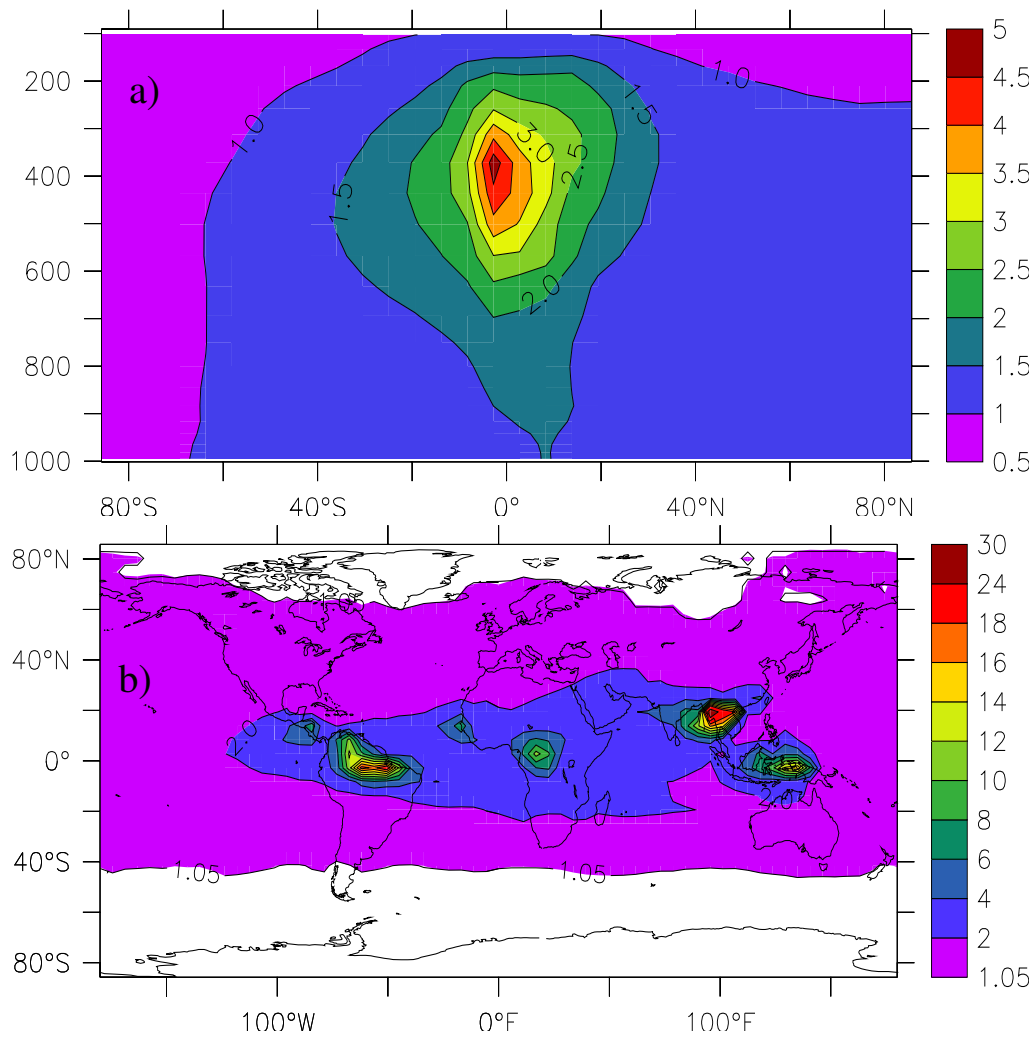


Figure 4.8: Ratio of JJA seasonal zonal means (a) and of the horizontal distributions at 300hPa (b) of  $\text{HNO}_3$  for the PICK5 vs. NoLtNO<sub>x</sub> runs.

The horizontal distribution plots at 300 hPa show the enhancements are well correlated with enhancements in NO<sub>x</sub>; over central South America, the central Atlantic ocean, east-central Africa, northern Australia and Borneo in DJF (Fig. 4.7b), and over northern South America, the central Atlantic ocean, eastern and central Africa, South-East Asia and Indonesia in JJA (fig 4.8b). The magnitude of the peak enhancement at this altitude is, however, much larger than that of any trace gas for the reasons mentioned; during DJF, HNO<sub>3</sub> is enhanced by over a factor of 30-40 with respect to the NoLtNO<sub>x</sub> run over South America, compared to a maximum factor of ~10-15 and ~10-12 for NO<sub>x</sub> and OH, respectively, for the same region. For other regions, the large enhancement in HNO<sub>3</sub> is similar, ranging up to a maximum factor larger than 80 over Borneo.

#### 4.1.4 Effects on PAN

Peroxyacetyl nitrate (PAN) acts as reservoir of NO<sub>x</sub>, thus extending its effective lifetime and range of influence. If produced in the NO<sub>x</sub>-enhanced environment in and around storms, PAN can be rapidly transported to the UT where cold temperatures and its non photodegradability make it very stable. Moreover, PAN is considerably less soluble than HNO<sub>3</sub>, so that aqueous-phase scavenging is not expected to be an important removal path for it (Seinfeld and Pandis, 1998). Once in the UT, it is subject to long-range transport (Crutzen, 1979), thus making it an efficient source of nitrogen in remote areas with low background levels, where it can be cycled back into NO<sub>2</sub> through thermal degradation, especially in subsiding airmasses. In midlatitude continental areas, PAN is formed over forested areas when NO<sub>x</sub> is available mainly from anthropogenic sources. Over the tropics, and particularly over pristine areas such as the Amazon river basin, where anthropogenic NO<sub>x</sub> does not occur in high concentrations, and where lightning rates are high, lightning produced NO<sub>x</sub> can exert a controlling effect on the formation of PAN. In the simulations, upon adding LtNO<sub>x</sub> PAN is enhanced mainly over the tropics where most of the lightning activity is

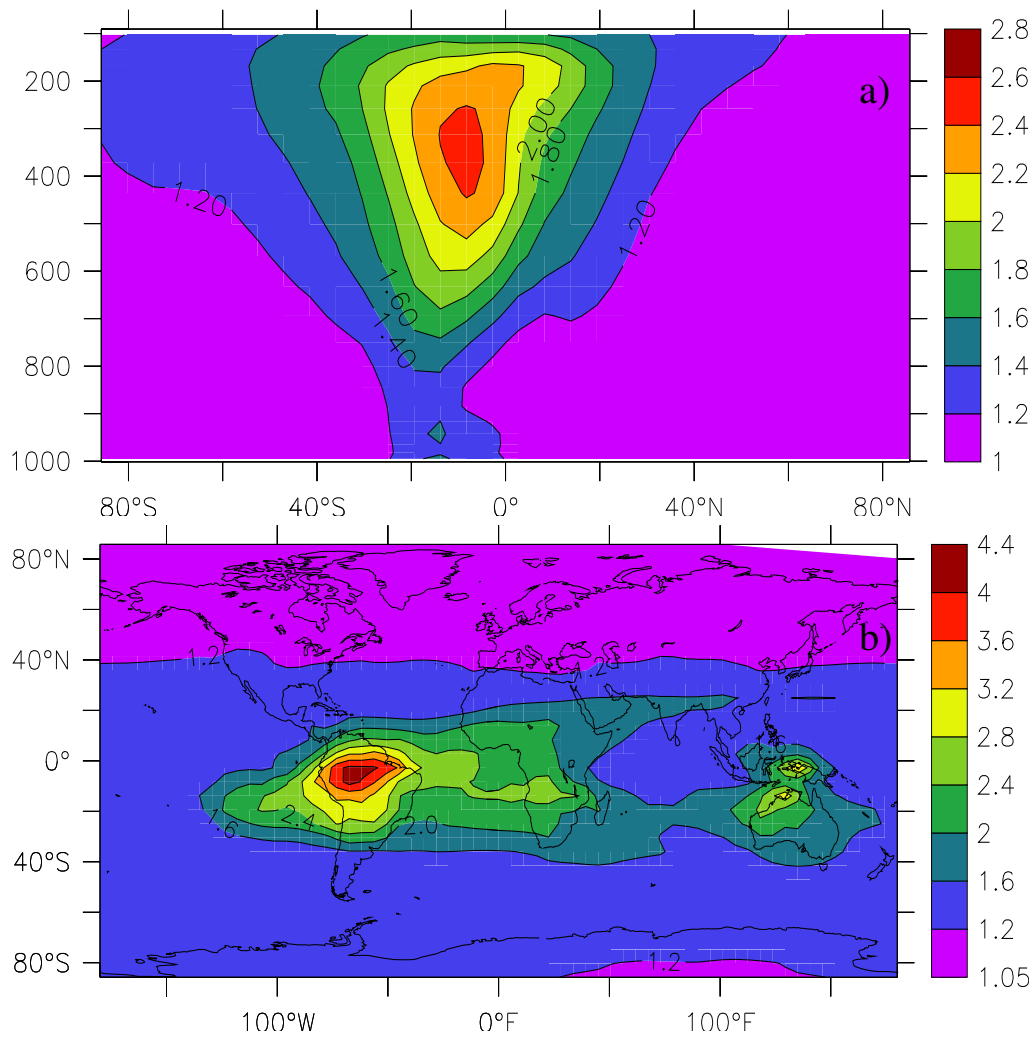


Figure 4.9: Ratio of DJF seasonal zonal means (a) and of the horizontal distributions at 300hPa (b) of PAN for the PICK5 vs. NoLtNO<sub>x</sub> runs.

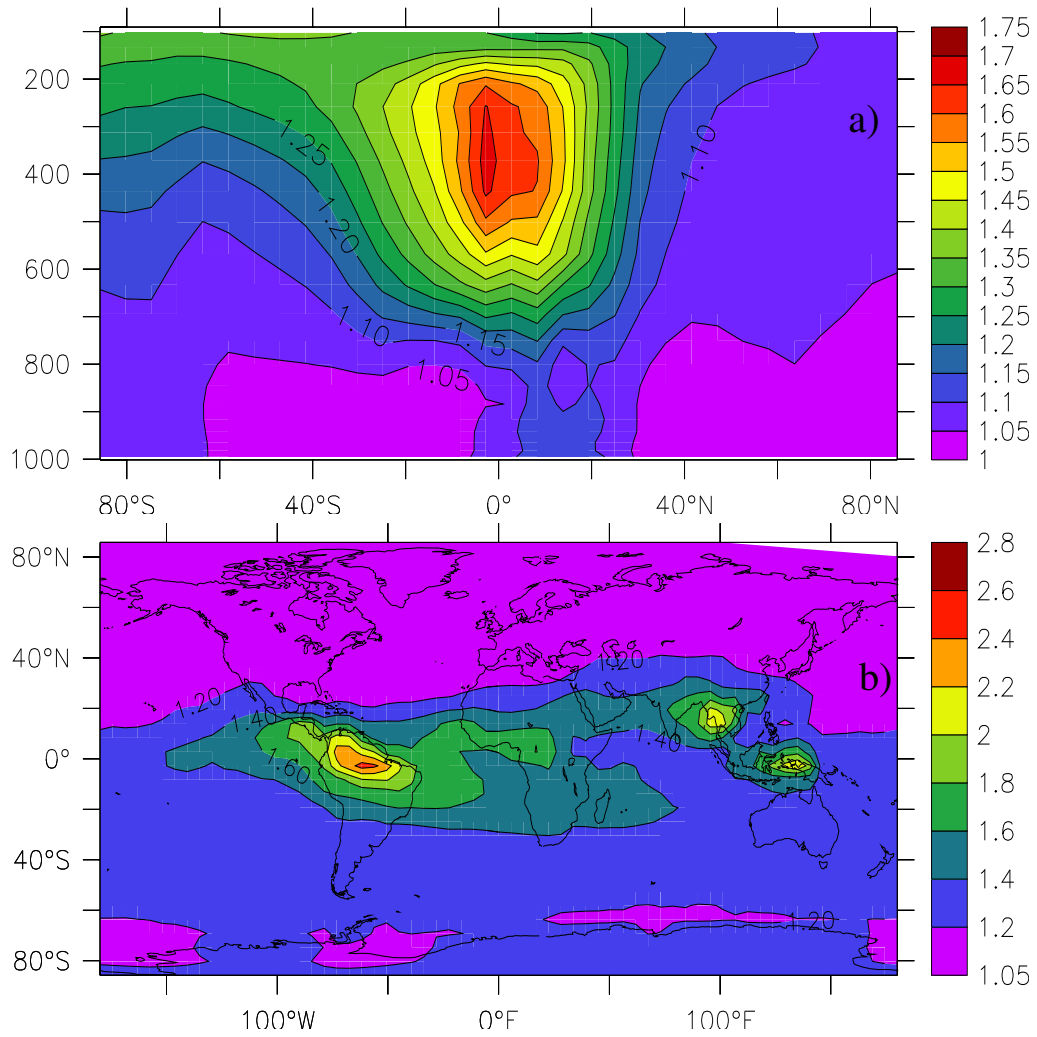


Figure 4.10: Ratio of JJA seasonal zonal mean (a) and of the horizontal distributions at 300hPa (b) of PAN for the PICK5 vs. NoLtNO<sub>x</sub> runs.

present. Maximum enhancements occur in the tropical UT for both seasons, with the latitude and the magnitude of the enhancement as the main differences between the two seasons. In the NH winter season (Figs.4.9), the largest enhancements with respect to the NoLtNO<sub>x</sub> occur approximately between the equator and 20° south, consistent with the position of the ITZC at that time of the year. Despite the strong temperature dependency of the degradation reaction of PAN, enhancements of between 20 and 40% are present at 1000 hPa, whereas at 800 hPa the enhancement factor reaches between 40 and 60%. The maximum enhancement factor, larger than 2, occurs in the UT, between 200 and 400 hPa, well correlated with the NO<sub>x</sub> enhancement maximum. Transport of PAN is also notable; increases of more than 60% with respect to the NOLtNO<sub>x</sub> run are simulated well into the eastern Pacific ocean, downwind of the source in central South America, as well as over most of the central Atlantic and southern Indian Oceans as a result of transport from in-situ production from central and southern Africa. The large enhancements over Papua-New Guinea and north-central Australia are also well correlated with strong lightning activity over the region (Fig. 4.9).

During summer conditions, the largest enhancement factors, though still occurring in the tropical UT, are now displaced further north (Figs.4.10). Enhancements are of the order of 50-75% with respect to the NOLtNO<sub>x</sub> run, mainly between 200 and 500 hPa and between approximately the equator and 20° north. Surface levels at the tropics are enhanced by approximately 10-15%. Geographically, the largest enhancements occur over central northern South America, where the ITCZ has moved north and coincides with the region where the model simulates the strongest flash activity for the season. Maximum enhancements are of the order of a factor of 2-3 there. Over Africa enhancements are lower, consistent with a weaker flash activity as simulated by the model. Over Asia, the largest enhancements occur over South-East Asia and Indonesia, consistent with the largest flash activity predicted by the model there. Again, a transport signal is simulated into the eastern Pacific with about 40% increase all the way to 150° west and

Table 4.1: OH mass- and volume-weighted tropospheric mean concentrations (in molec/cm<sup>3</sup>) and lifetimes of CH<sub>4</sub> and MCF for the 5 different model runs.

|   | NoLtNO <sub>x</sub> | PICK2 | PICK5 | PICK10 | PICK20 |
|---|---------------------|-------|-------|--------|--------|
| (OH) <sub>m</sub> (×10 <sup>6</sup> )             | 0.82                | 0.89  | 1.0   | 1.1    | 1.23   |
| (OH) <sub>v</sub> (×10 <sup>6</sup> )             | 0.73                | 0.83  | 0.94  | 1.05   | 1.19   |
| τ <sub>(CH<sub>4</sub>)</sub> (yrs.) <sup>a</sup> | 10.26               | 9.47  | 8.79  | 8.07   | 7.34   |
| τ <sub>(CH<sub>4</sub>)</sub> (yrs.) <sup>b</sup> | 10.82               | 9.93  | 9.13  | 8.39   | 7.59   |
| τ <sub>(MCF)</sub> (yrs.)                         | 6.6                 | 6.04  | 5.55  | 5.09   | 4.6    |

<sup>a</sup>Calculated using online budgets

<sup>b</sup>Approximated with monthly mean model output(see text)

across the entire central Atlantic and southern Indian oceans as a result of transport from Africa.

#### 4.1.5 Effects on OH and the Tropospheric Oxidizing Efficiency

The effects of LtNO<sub>x</sub> on OH radical concentration and the oxidizing efficiency of the atmosphere have not received as much attention as those on O<sub>3</sub>. One might then pose the question: how does LtNO<sub>x</sub> affect global OH concentrations and consequently the oxidizing efficiency of the atmosphere? This has been considered in Labrador *et al.* (2004b). It is not immediately clear that the effect would be significant compared to the effect on O<sub>3</sub>, particularly given that the the largest effects on NO<sub>x</sub> occur in the UT (Figs. 4.1 and 4.2), where colder temperatures make most photooxidation reactions less efficient.

The overall effect on OH can be considered in terms of the mass- and volume-weighted concentrations ([OH]<sub>m</sub> and [OH]<sub>v</sub> hereafter) (Lawrence *et al.*, 2001); Table 4.1 shows that [OH]<sub>m</sub> ([OH]<sub>v</sub>) increases by about 50% (> 63%) from the NoLtNO<sub>x</sub> to the PICK20 run.

For every 5Tg(N)yr<sup>-1</sup> increase in the LtNO<sub>x</sub> source strength, [OH]<sub>m</sub> ([OH]<sub>v</sub>) increases by about 25% (29%) between the NoLtNO<sub>x</sub> and PICK5 runs, 10% (12%) between the PICK5 and PICK10 runs, and 6%(6%) be-

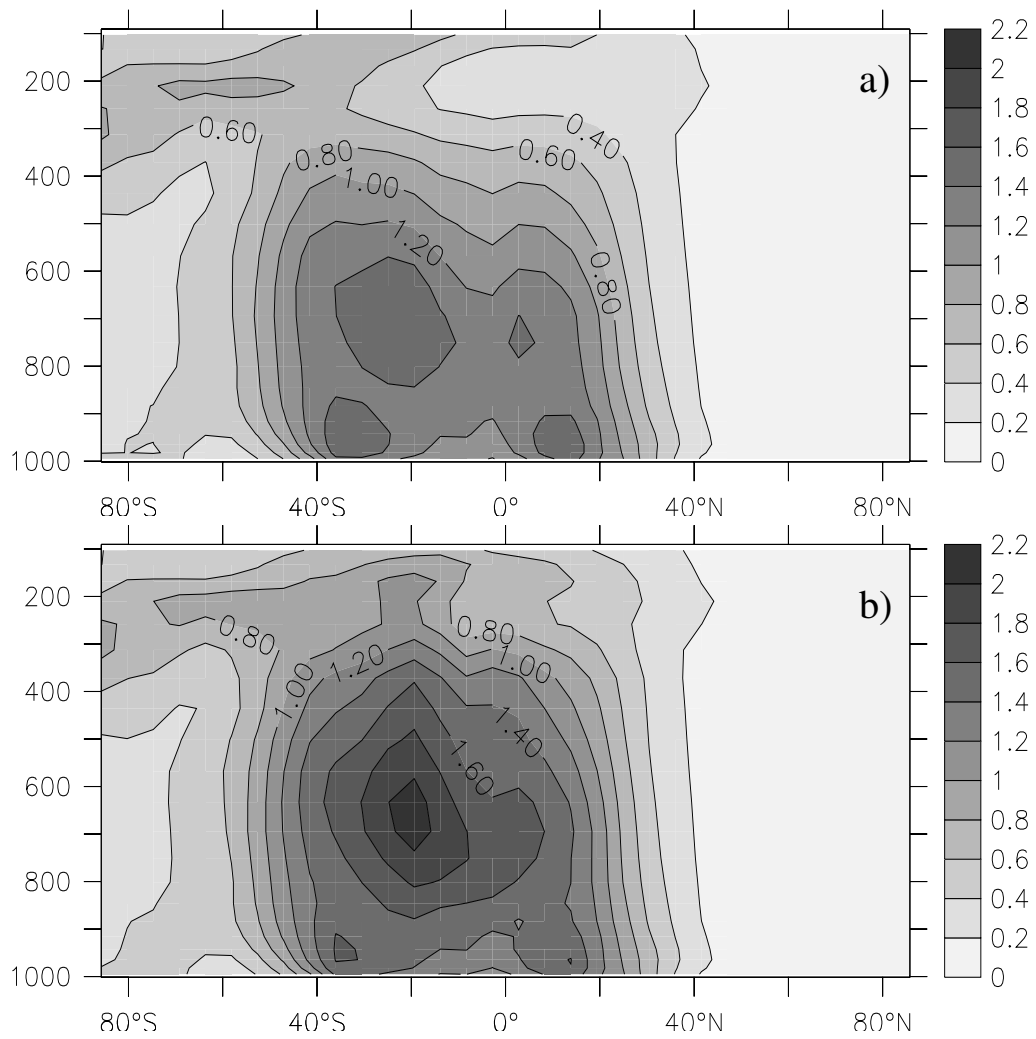


Figure 4.11: Zonal mean DJF 97 average OH concentration (in  $\times 10^6$  molec/cm<sup>3</sup>) for the NoLtNO<sub>x</sub> (a) and Pick5 (b) runs.

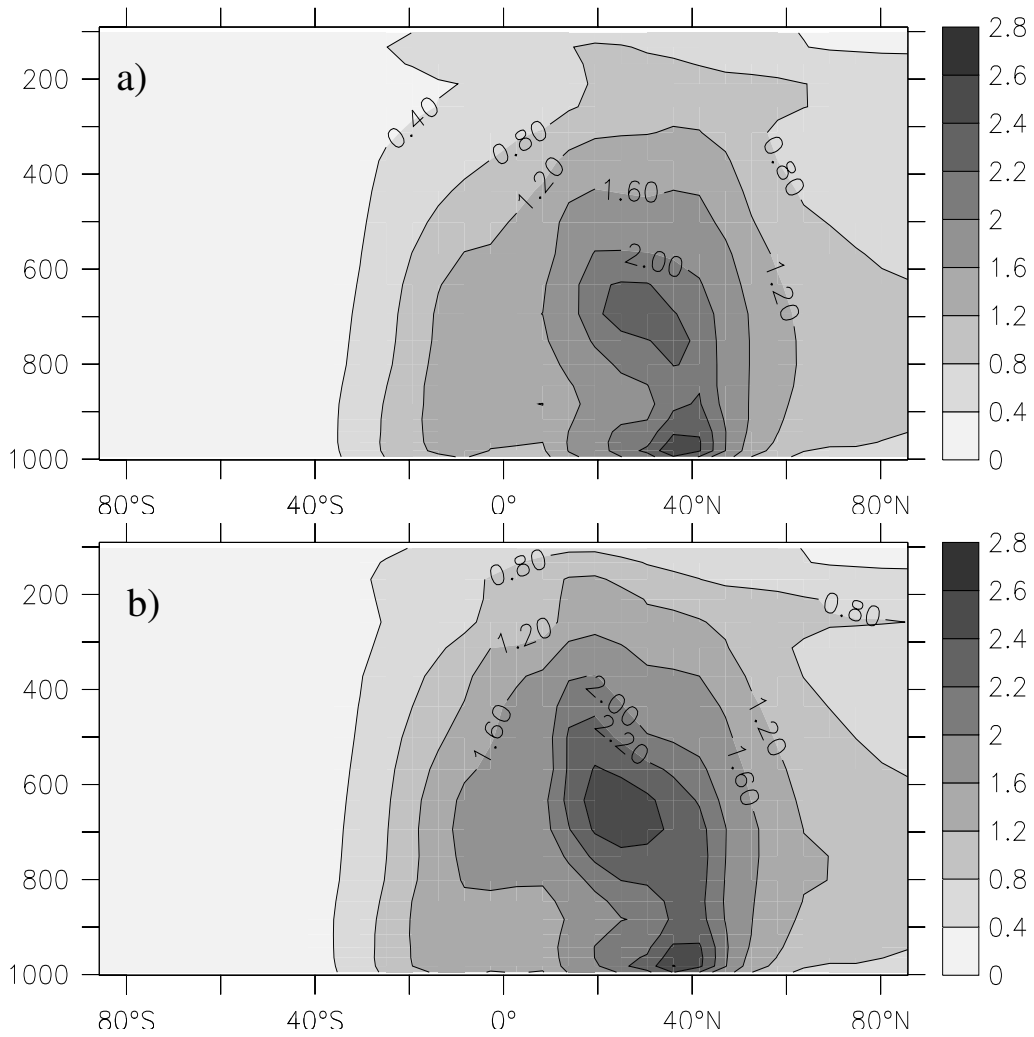


Figure 4.12: Zonal mean JJA 97 average OH concentration (in  $\times 10^6$  molec/cm<sup>3</sup>) for the NoLtNO<sub>x</sub> (a) and Pick5 (b) runs.

Table 4.2: Lifetimes of CH<sub>4</sub> and MCF and their corresponding LtNO<sub>x</sub> production range according to various studies.

| REFERENCE                        | $\tau_{(CH_4)}$<br>yrs               | LtNO <sub>x</sub><br>Tg/yr | $\tau_{(MCF)}$<br>yrs               | LtNO <sub>x</sub><br>Tg/yr |
|----------------------------------|--------------------------------------|----------------------------|-------------------------------------|----------------------------|
| Spivakovsky <i>et al.</i> (2000) | 9.6                                  | ~2                         | 4.6                                 | 10-20                      |
| Prinn <i>et al.</i> (1995)       | 8.9 <sup>+1.6</sup> <sub>-0.8</sub>  | 0-10                       | 4.6±0.3                             | 10-20                      |
| Prinn <i>et al.</i> (2001)       | 10.1 <sup>+1.7</sup> <sub>-1.2</sub> | 0-5                        | 6.0 <sup>+1</sup> <sub>-0.7</sub>   | 0-5                        |
| Krol <i>et al.</i> (1998)        | 8.6 <sup>+1.6</sup> <sub>-0.8</sub>  | 0-10                       | 4.5±0.1                             | 10-20                      |
| Montzka <i>et al.</i> (2000)     | —                                    | —                          | 5.2 <sup>+0.2</sup> <sub>-0.3</sub> | 5-10                       |
| Dentener <i>et al.</i> (2003)    | 9.0±0.1                              | ~2-5                       | —                                   | —                          |

tween the PICK10 and PICK20 runs, indicating a tendency towards saturation. The vertical distribution of OH and its regional changes due to LtNO<sub>x</sub> are depicted in Figures 4.11 - 4.15. From Figs 4.11, 4.12 and 4.13 it can be seen that the largest absolute increase in OH due to LtNO<sub>x</sub> in both seasons occurs in the middle troposphere (MT), approximately between 400-500 hPa, while the largest relative enhancements occur in the UT (~200-300 hPa), (Figs. 4.14(top) and 4.15 (top)), corresponding with the regions where NO<sub>x</sub> is increased most strongly due to lightning .

The reason for this is twofold; first, the extremely low OH concentrations in the cold and dry tropical UT in the NoLtNO<sub>x</sub> run (Fig. 4.11 (top) and 4.12 (top)) cause even a small absolute increase in OH to translate into a large relative increase in that region. Second, near the tropopause, OH production by O(<sup>1</sup>D)+H<sub>2</sub>O is slow, so that secondary sources such as the reaction of NO with HO<sub>2</sub> become relatively more important than at lower altitudes.

Also, HO<sub>x</sub> yields for reactions such as photolysis of acetone and oxidation of methane are enhanced in the presence of NO<sub>x</sub> (Folkins and Chatfield, 2000). As with other trace gases, a good correlation is found between the areas where NO<sub>x</sub> and OH are enhanced.

How do these changes in OH affect the oxidizing efficiency of the atmosphere? We examine this with respect to two long-lived trace gases, methane (CH<sub>4</sub>) and methyl-chloroform (CH<sub>3</sub>CCl<sub>3</sub>, or MCF for short). Their lifetimes ( $\tau_{(CH_4)}$  and  $\tau_{(MCF)}$ ) for the five runs are given in Table 4.1. While  $\tau_{(CH_4)}$  =

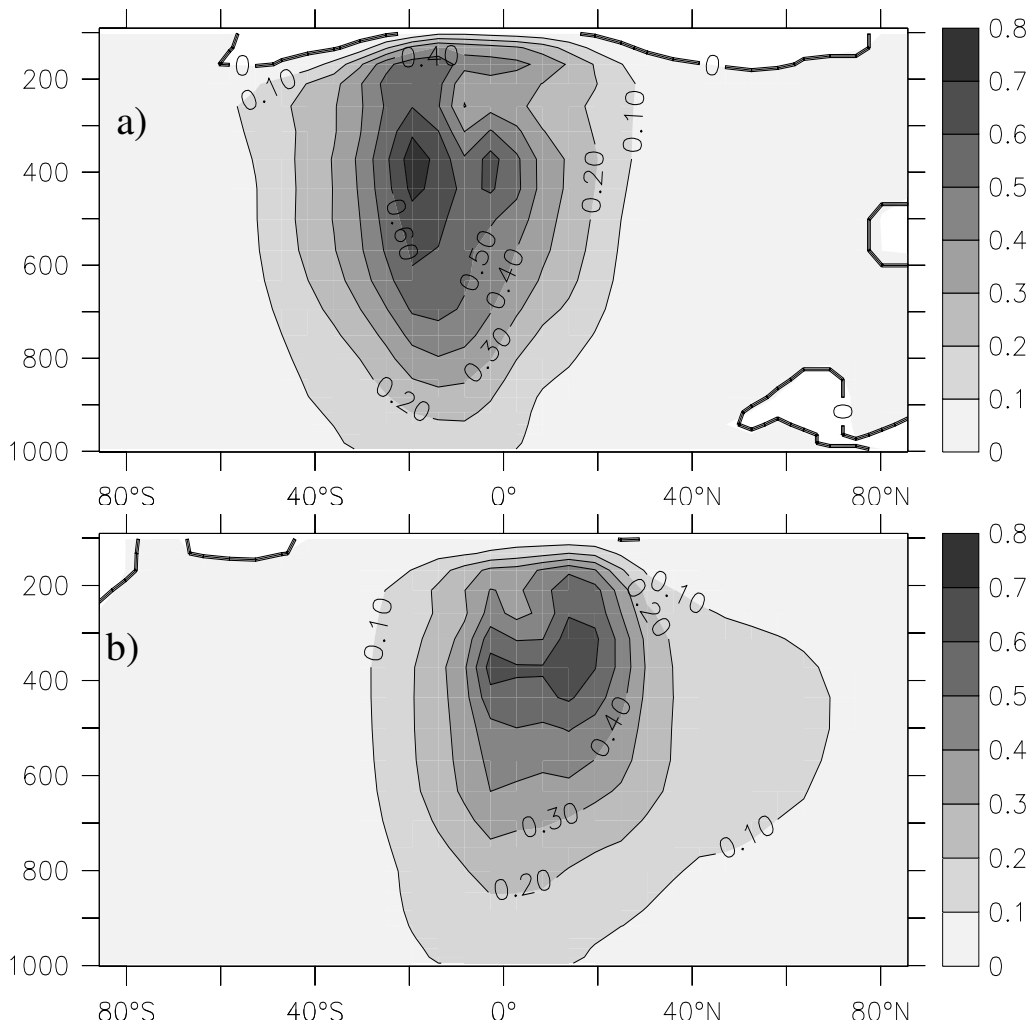


Figure 4.13: Absolute DJF 97 (a) and JJA (b) difference of the annual zonal mean OH concentration (in  $\times 10^6$  molec/cm<sup>3</sup>) of the PICK5 and NoLtNO<sub>x</sub> runs.

10.26 years is computed for the NoLtNO<sub>x</sub> run, the PICK5 run yields  $\tau_{(CH_4)} = 8.79$  years, a reduction of nearly 15%. A similar relative reduction in  $\tau_{(MCF)}$  is also computed. Note that since CH<sub>4</sub> is simulated in the model, we can use the online model budget routines to compute  $\tau_{(CH_4)}$  (using the tropopause based on the temperature lapse rate criterion). However, since we do not simulate MCF, we approximate  $\tau_{(MCF)}$  using monthly mean OH and temperature fields from the model output, a climatological tropopause, and a uniform distribution in the troposphere. We verify that the error in this approximation is small by doing the same for  $\tau_{(CH_4)}$  and comparing to the online budget values (Table 4.1), showing that the offline estimates are biased  $\sim 5.5\%$  and  $\sim 3.9\%$  high in the NoLtNO<sub>x</sub> and PICK5 run, respectively; thus  $\tau_{(MCF)}$  values in Table 1 are also expected to be slightly overestimated.

Comparing the computed lifetimes to recent estimates given in the literature (Table 4.2), it can be seen that at both ends of the LtNO<sub>x</sub> source magnitude spectrum, the computed  $\tau_{(CH_4)}$  and  $\tau_{(MCF)}$  values are still barely within the current range of uncertainty. A tendency is hard to discern, indicating the uncertainty in factors other than LtNO<sub>x</sub> that also affect OH and therefore  $\tau_{(CH_4)}$  and  $\tau_{(MCF)}$ . However, it can be noticed that  $\tau_{(CH_4)}$  in all five references corresponds to or includes the 2-5 Tg yr<sup>-1</sup> LtNO<sub>x</sub> production range.  $\tau_{(MCF)}$  values correspond to the higher end of the spectrum, even after accounting for the slight high bias in the offline estimates. The inconsistency between the implied LtNO<sub>x</sub> source magnitudes based on  $\tau_{(CH_4)}$  and  $\tau_{(MCF)}$  is related to the different OH spatial distributions used in the different studies as well as to the different temperature dependences of the reaction rates of the two gases with OH.

Finally the question of which part of the atmosphere is mainly responsible for the computed changes in the lifetimes is considered. The troposphere was divided into compartments (following Lawrence *et al.* (2001)) and the amounts of oxidized CH<sub>4</sub> as well as the fraction (in %) of the total tropospheric CH<sub>4</sub> burden oxidized in each compartment were computed for both the NoLtNO<sub>x</sub> and PICK5 runs (Fig. 4.16). In absolute as well as relative

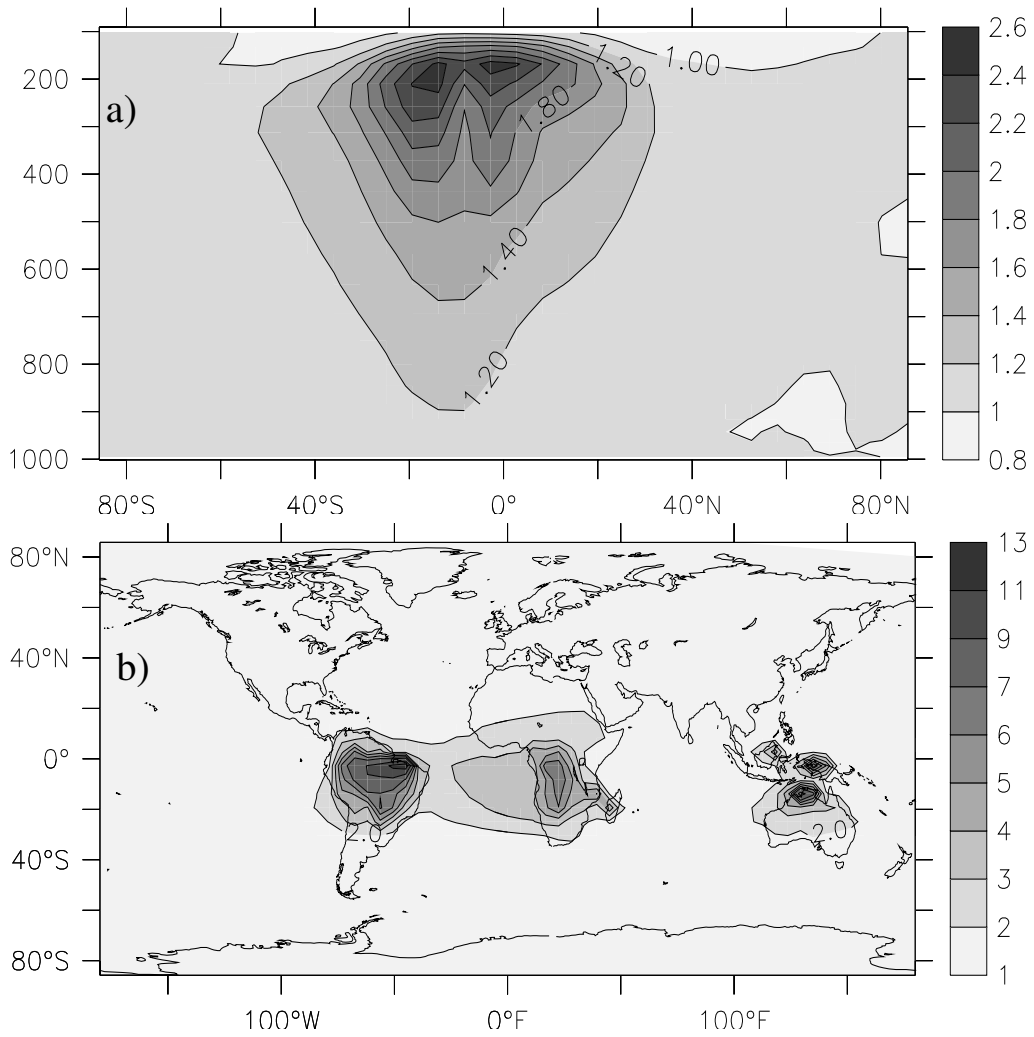


Figure 4.14: Ratio of DJF seasonal zonal means (top) and of the horizontal distributions at 300hPa (bottom) of OH for the PICK5 and NoLtNO<sub>x</sub> runs.

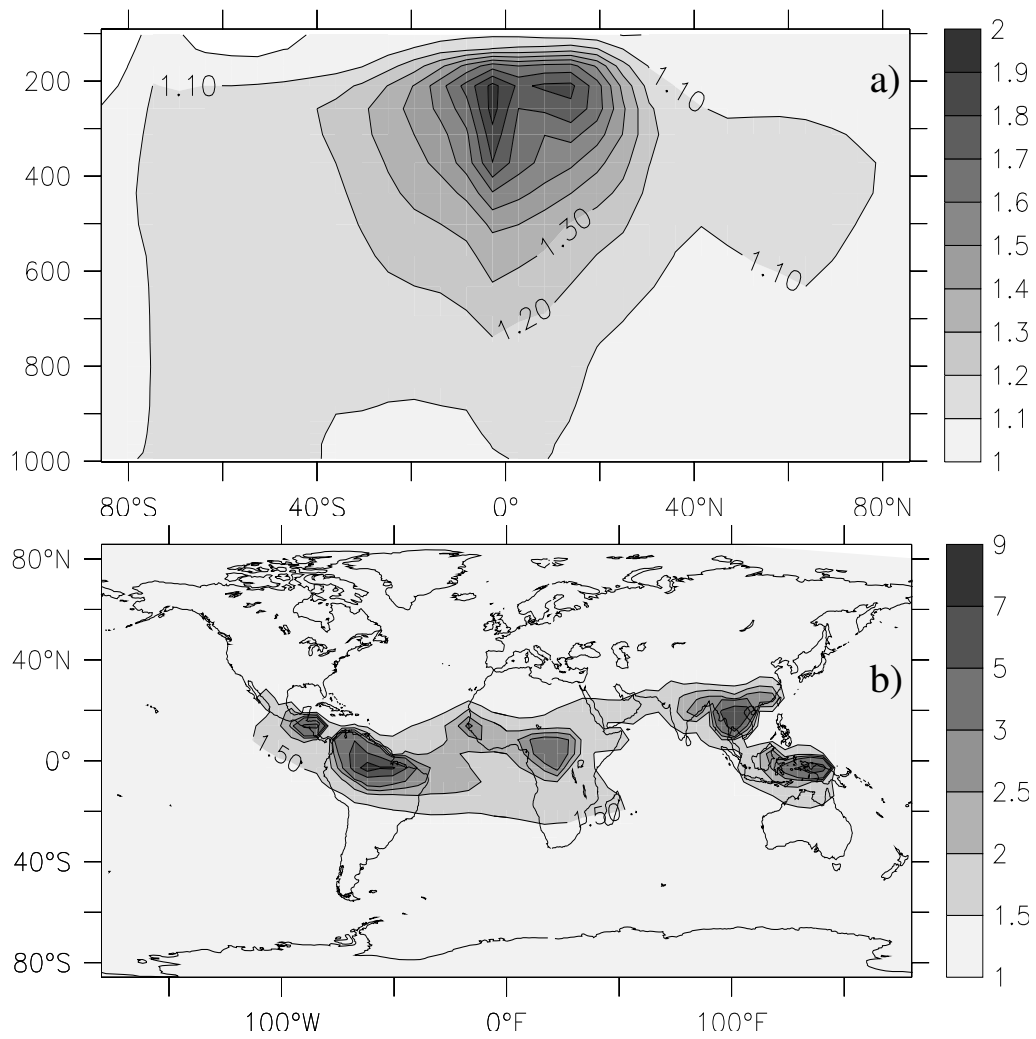


Figure 4.15: Ratio of JJA seasonal zonal means (a) and of the horizontal distributions at 300hPa (b) of OH for the PICK5 and NoLtNO<sub>x</sub> runs.

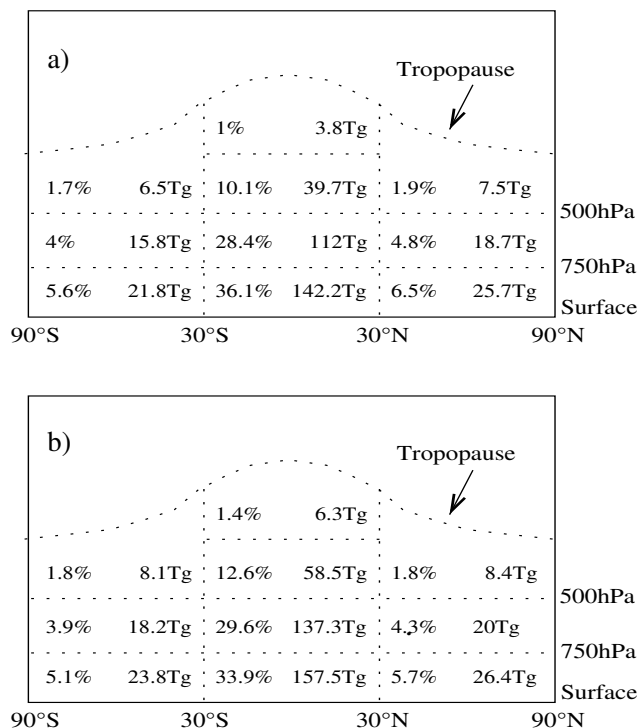


Figure 4.16: Percentages and total  $\text{CH}_4$  oxidized in tropospheric subdomains in the NoLtNO<sub>x</sub> (a) and PICK5 runs (b).

terms, most of the  $\text{CH}_4$  is oxidized in the tropical troposphere, especially in the LT. The largest absolute increase in the amount of  $\text{CH}_4$  oxidized occurs in the two lowermost compartments of the tropical troposphere due to the strong temperature dependence of the oxidation reaction, whereas the largest relative increases occur above 500 hPa (with increases of  $\sim 65\%$  and  $\sim 47\%$ , respectively, in the upper two tropical compartments) due to the larger relative increase in OH there (Figs. 4.14 and 4.15).

These effects can be compared to the effects of LtNO<sub>x</sub> on O<sub>3</sub>. It is found that in the runs carried out, the tropospheric burden of O<sub>3</sub> increases from 377 to 430 Tg, or  $\sim 14\%$ , between the NoLtNO<sub>x</sub> and PICK5 runs. Thus, the effects of LtNO<sub>x</sub> on the oxidizing efficiency are similar in magnitude to the relative effects on O<sub>3</sub>, while the effects on  $[\text{OH}]_m$  and  $[\text{OH}]_v$  are even larger.

These results show that the OH concentration and the tropospheric oxidizing efficiency are strongly sensitive to the global LtNO<sub>x</sub> source mag-

nitude, comparable to or larger than the effect of LtNO<sub>x</sub> on O<sub>3</sub>. In this modeling study, the uncertainty in LtNO<sub>x</sub> alone translates into an uncertainty in the simulated  $\tau_{(CH_4)}$  and  $\tau_{(MCF)}$  which is about as large as their overall uncertainty based on other recent studies using various approaches to estimate their lifetimes. Based on this, it is tempting to suggest that improved estimates of the lifetimes of traces gases such as CH<sub>4</sub> and MCF could be used to constrain the global source of NO<sub>x</sub> from lightning. However, this is currently impractical, due to the many other uncertainties involved. For instance, the LtNO<sub>x</sub> parameterization introduces an unquantified error in both its horizontal and vertical distribution, which is important because the sensitivity of OH to additional NO<sub>x</sub> varies regionally. The competition of LtNO<sub>x</sub> with other NO<sub>x</sub> sources (e.g., biomass burning) will be influenced by uncertainties in their magnitudes and in their convective lofting to the upper troposphere; this also applies to other competing HO<sub>x</sub> precursors (e.g., acetone). Finally, there are still uncertainties in many key reaction rates, such as PAN formation and thermal degradation. Reduction in these uncertainties will lead to quantitative changes in the effects of LtNO<sub>x</sub> on OH and on the oxidizing efficiency computed with improved models in future studies. However, this is not likely to result in a qualitative change in the main conclusion, that is, that the strong effect of LtNO<sub>x</sub> on OH and the tropospheric oxidizing efficiency should be considered alongside its effects on O<sub>3</sub>, and reinforces the need for a more accurate determination of the source of NO<sub>x</sub> from lightning in future studies.

## 4.2 Sensitivity of Tropospheric Chemistry to Increases in the Magnitude of the Source of NO<sub>x</sub> from Lightning

The range of uncertainty in the source of NO<sub>x</sub> from lightning spans a full order of magnitude. One can therefore ask what kind of response would different burdens of LtNO<sub>x</sub> within this range have on tropospheric chemistry;

is one to expect a linear response in trace gases to increases in lightning-produced  $NO_x$ ? Will burdens of trace gases stop responding to increases in  $LtNO_x$ , i.e., become saturated? The answer is of particular importance since, as seen in Chapter 3, lightning is prevalent in the tropics and in many pristine areas where both  $NO_x$  and other trace gases' originally low background concentrations can be very low, thus rendering them extremely sensitive to inputs from another  $NO_x$  source. One can therefore expect the largest enhancements over these regions where, furthermore, the transport patterns present, such as the trade winds and the Hadley circulation, can redistribute newly formed or enhanced species from, for example, tropical continental regions to remote marine areas. In this section, the responses of  $NO_x$ , as well as  $O_3$ ,  $OH$ ,  $HNO_3$  and PAN to increases in the source magnitude of  $LtNO_x$  are studied. Since lightning is more frequent over the tropics, special consideration has been given to this region; the burdens of these trace gases were calculated for the whole globe ( $90^\circ$  north to  $90^\circ$  south), the tropics (between  $25^\circ$  north and south), and the extratropics ( $90^\circ$  to  $25^\circ$  south and  $25^\circ$  to  $90^\circ$  north), for the EVEN2, 5 and 10 and PICK2, 5, 10 and 20 runs. Since the PICK and ANVIL runs produce generally similar results, as discussed in the next chapter, the comparisons will be constrained to the EVEN and PICK set of runs.

Figs. 4.17-4.19 show the burdens for the EVEN and PICK runs for  $NO_x$ ,  $O_3$ ,  $OH$ ,  $HNO_3$  and PAN, as a function of the  $LtNO_x$  source magnitude. A consistent tendency was for the PICK runs to result in higher burdens for all trace gases than the EVEN runs due to the lifetime of  $LtNO_x$  in the UT, where the PICK runs simulate the release of larger amounts than the EVEN runs, generally being longer than in the LT.

Globally, adding  $LtNO_x$  produces a tendency towards saturation in the 2 - 5Tg(N)/yr range, which becomes very clear by the time the 20 Tg(N)/yr production rate is reached. The response of the EVEN set of runs is similar to the PICK runs, although the magnitude of the absolute increase in total  $NO_x$  is somewhat less than the PICK runs.

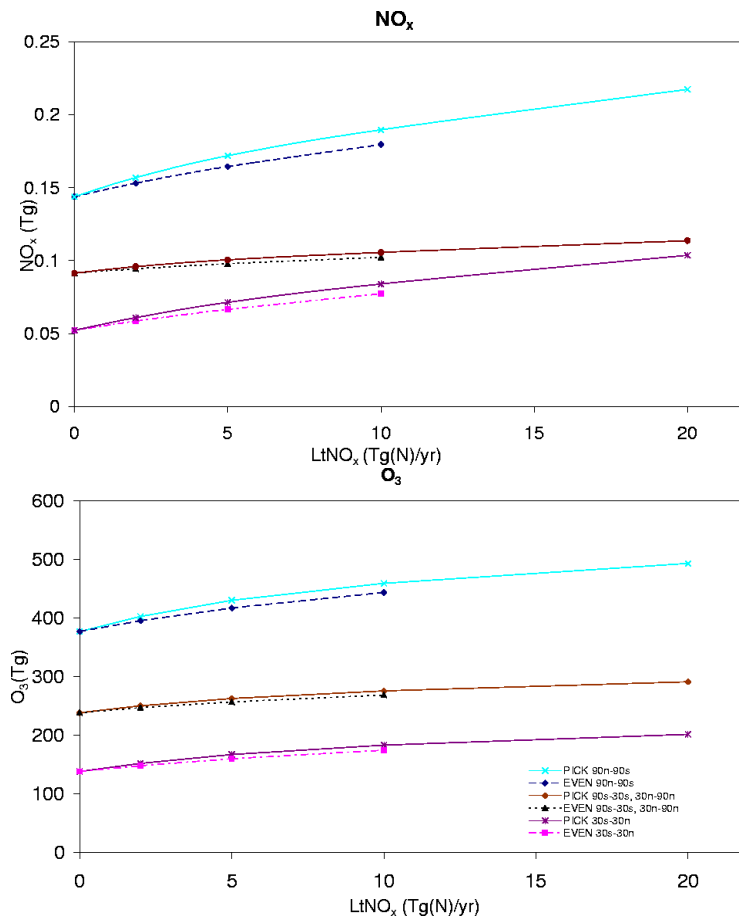


Figure 4.17: Burdens of NO<sub>x</sub> and O<sub>3</sub>, for the PICK (solid lines) and EVEN (dotted and dashed lines) series of runs for the tropics and extratropics.

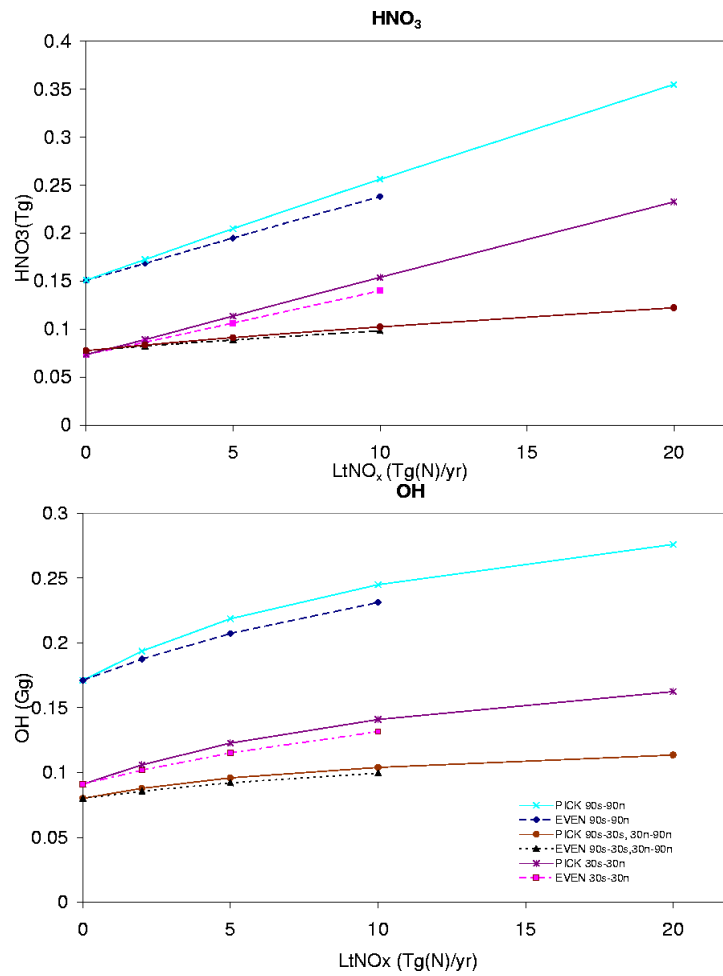


Figure 4.18: Burdens of  $HNO_3$  and  $OH$  for the PICK (solid lines) and EVEN (dotted and dashed lines) series of runs for the tropics and extratropics.

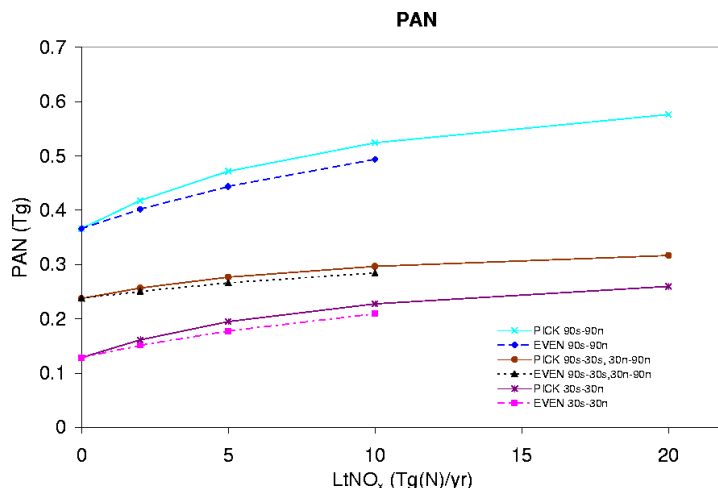


Figure 4.19: Burden of PAN, for the PICK (solid lines) and EVEN (dotted and dashed lines) series of runs for the tropics and extratropics.

The tropical regions show a more sensitive response, due in large part to the fact that most of the lightning activity in the model is concentrated there (3.1) and because the other competing sources (especially fossil-fuel burning) tend to be smaller in the tropics than in the extratropics. Though the same non-linear response as in the whole globe is also present, increases in total NO<sub>x</sub> are larger in the tropics.

As with NO<sub>x</sub>, ozone shows a non-linear response to increases in LtNO<sub>x</sub>, tending towards saturation at the highest end of the range in both sets of runs. The PICK runs simulate larger enhancements throughout the entire production range, particularly in the tropical regions (Fig. 4.17b and Table 4.3). Globally, the PICK20 run simulates an average increase of 30% with respect to the NoLtNO<sub>x</sub> run, while in the tropics ozone is enhanced by 45% for the same run. These enhancements are all the more important considering that they take place in the UT, where longer lifetimes and the Hadley circulation can transport this ozone to higher latitudes and because O<sub>3</sub> is more efficient as a greenhouse gas at higher altitudes. This increase of O<sub>3</sub> at higher altitudes, followed by downward transport, is responsible for the reduction of surface NO<sub>x</sub> levels simulated at high latitudes in Figure 2a and 4a.

Fig. 4.17c shows that the relative change in the global OH burden is

Table 4.3: Global annual burdens of the NoLtNO<sub>x</sub> run for different trace gases (in Tg for NO<sub>x</sub>, O<sub>3</sub>, HNO<sub>3</sub> and PAN and in  $\times 10^6$  molec for OH) and relative increases (in percent) of the burdens for the whole globe and tropics (T) for the different runs with respect to the LtNO<sub>x</sub> runs

| Trace<br>gas         | Burden in<br>NoLtNO <sub>x</sub> run | Relative increase vs. NoLtNO <sub>x</sub> run |      |       |       |      |      |      |
|----------------------|--------------------------------------|---|------|-------|-------|------|------|------|
|                      |                                      | P2  | P5   | P10   | P20   | E2   | E5   | E10  |
| NO <sub>x</sub>      | 0.14                                 | 9.1   | 19.5 | 31.9  | 51.2  | 6.4  | 14.4 | 24.9 |
| NO <sub>x</sub> (T)  | 0.05                                 | 16.6  | 36.4 | 60.6  | 98.2  | 11.9 | 27.3 | 47.8 |
| Ozone                | 377.1                                | 6.8   | 14.1 | 21.8  | 30.7  | 4.9  | 10.6 | 17.6 |
| Ozone (T)            | 138.5                                | 9.9   | 20.8 | 32.3  | 45.6  | 7.1  | 15.7 | 26.2 |
| OH                   | 0.17                                 | 13.2  | 27.8 | 43.1  | 61.3  | 9.6  | 21.1 | 35.1 |
| OH (T)               | 0.09                                 | 16.4  | 34.8 | 54.8  | 78.4  | 11.9 | 26.5 | 44.6 |
| HNO <sub>3</sub>     | 0.15                                 | 14.2  | 35.6 | 69.6  | 135.2 | 11.6 | 29.1 | 59.8 |
| HNO <sub>3</sub> (T) | 0.07                                 | 21.4  | 54.7 | 109.6 | 217   | 17.6 | 44.7 | 90.7 |
| PAN                  | 0.37                                 | 14.2  | 28.9 | 43.2  | 57.4  | 9.7  | 21.3 | 34.9 |
| PAN (T)              | 0.13                                 | 8.1   | 51.7 | 24.8  | 33.2  | 5.5  | 12.0 | 19.8 |

greater than that of O<sub>3</sub> and even exceeds that of NO<sub>x</sub> due to the fact that both NO<sub>x</sub> and O<sub>3</sub>, both precursors of OH, are also increased. Table 4.4 shows the regional annual mass-weighted OH mean concentrations, as suggested by Lawrence *et al.* (2001), for the EVEN5 and PICK5 runs as well as the relative increases of the two vertical distributions versus the NoLtNO<sub>x</sub> run.

The largest OH increases in all three distributions are in the southern hemisphere, despite the lightning activity being dominant in the northern hemisphere (Christian *et al.*, 2003). For instance, in the EVEN5 distribution, the enhancements in the 90°S-30°S domains at all altitudes are about a factor of two larger than those in the equivalent domains in the northern hemisphere, whereas in the 30°S-0° domains, they are about 50% larger than in the 0°-30°N ones. In the PICK distribution the enhancements in the 90°S-30°S regions below 750 hPa are a factor of three larger, and in the 750-500 hPa and 500-250 hPa domains approximately a factor of two larger than the equivalent northern hemisphere domains. In the 30°S-0° domains, the enhancements are about 50% larger than in the 0°-30°N do-

Table 4.4: Regional annual mean airmass-weighted OH concentrations ( $\times 10^6$  molec/cm<sup>3</sup>) and relative increases vs. NoLtNO<sub>x</sub> (in parenthesis) for the different LtNO<sub>x</sub> vertical distributions

| REGION                  | NoLtNO <sub>x</sub> | EVEN5         | PICK5         |
|-------------------------|---------------------|---------------|---------------|
| Below 750 hPa 90°S-30°S | 0.54                | 0.58 (+7.4%)  | 0.59 (+9.3%)  |
| Below 750 hPa 30°S-0°   | 1.25                | 1.45 (+16%)   | 1.43 (+14.4%) |
| Below 750 hPa 0°-30°N   | 1.44                | 1.59 (+10.4%) | 1.56 (+8.3%)  |
| Below 750 hPa 30°N-90°N | 0.82                | 0.85 (+3.7%)  | 0.85 (+3.7%)  |
| 750-500 hPa 90°S-30°S   | 0.48                | 0.55 (+14.6%) | 0.56 (+17%)   |
| 750-500 hPa 30°S-0°     | 1.21                | 1.53 (+26.4%) | 1.56 (+28.9%) |
| 750-500 hPa 0°-30°N     | 1.44                | 1.71 (+18.8%) | 1.72 (+19.4%) |
| 750-500 hPa 30°N-90°N   | 0.72                | 0.77 (+6.9%)  | 0.77 (+6.9%)  |
| 500-250 hPa 90°S-30°S   | 0.34                | 0.40 (+17.6%) | 0.42 (+23.5%) |
| 500-250 hPa 30°S-0°     | 0.67                | 0.93 (+38.8%) | 1.07 (+59.7%) |
| 500-250 hPa 0°-30°N     | 0.87                | 1.13 (+29.9%) | 1.27 (+46%)   |
| 500-250 hPa 30°N-90°N   | 0.52                | 0.57 (+9.6%)  | 0.58 (+11.5%) |

mains. This marked sensitivity of the southern hemisphere to LtNO<sub>x</sub> is a result of smaller total NO<sub>x</sub> emissions from other sources, which makes OH more sensitive to increases in NO<sub>x</sub> there.

Adding LtNO<sub>x</sub> causes the HNO<sub>3</sub> burden to increase nearly linearly, the slope of the increase is much more pronounced than that of other trace gases (Figure 4.17d). The reason for this very strong response of HNO<sub>3</sub> is, as indicated previously, the increase in its two main precursors, NO<sub>2</sub> and OH. From Table 4.3 it can be seen that, in the PICK series of runs, for every 5Tg of NO<sub>x</sub> from lightning added to the annual global burden, HNO<sub>3</sub> burdens increase by approximately 33% globally with respect to the NOLtNO<sub>x</sub> run, from the PICK5 to the PICK20 runs. In the tropics this increase is more pronounced; for every 5 Tg of NO<sub>x</sub>, the burden of HNO<sub>3</sub> increases by approximately 53% with respect to the NOLtNO<sub>x</sub> run from the PICK5 to the PICK20 runs. The EVEN series of runs show a less sensitive response to increases in LtNO<sub>x</sub> than the PICK runs, both globally and in the tropics. Globally, the HNO<sub>3</sub> burden increases by 29% with respect to the NOLtNO<sub>x</sub> run for every 5 Tg of LtNO<sub>x</sub> added between the NOLtNO<sub>x</sub>

and the EVEN10 runs. In the tropics the EVEN distributions increase by 44.7% between the same set of runs.

From Table 4.3 and Figure 4.17e it can be seen that the burden of PAN can be increased by over 50% versus the NoLtNO<sub>x</sub> run in the tropical UT when the PICK vertical distribution is assumed. However, the tendency towards saturation is much stronger for PAN than for other trace gases: for every 5 Tg(N)/yr LtNO<sub>x</sub>, PAN is enhanced by almost 52% between the NoLtNO<sub>x</sub> and PICK5 runs, or about 14% more than NO<sub>x</sub> (Table 4.3). Then, for every additional 5 Tg(N)/yr, PAN is enhanced by 17% between the PICK10 and 20 runs, or about half the increase in NO<sub>x</sub> for the same range. The strong response at the lower end of the LtNO<sub>x</sub> production range in the tropics can be accounted for by the very strong emissions of isoprene in MATCH-MPIC runs in the tropics (von Kuhlmann *et al.*, 2004). The formation of PAN depends, among other factors, on the availability of the peroxyacetyl radical, the dominant producer of which in our runs in the tropical regions is isoprene. As LtNO<sub>x</sub> is further increased, however, one moves into a hydrocarbon-limited PAN formation regime. While NO<sub>x</sub> is increased through LtNO<sub>x</sub>, isoprene emissions, and other PAN precursors are kept constant in our runs, leading to the rapid saturation signal.

### 4.3 Comparisons of Model Output with Observations

Comparisons with measurement campaign results constitute the best way to evaluate model output. However, biases may be introduced when comparing the large concentrations of trace gases measured in areas typically targeted by campaigns, such as convective outflow regions, with averaged output from model results. Likewise, the dates of campaigns and model year simulations do not always coincide when making comparisons. Running model simulations that match the dates in which campaigns take place would produce the most comparable results and minimize differences in

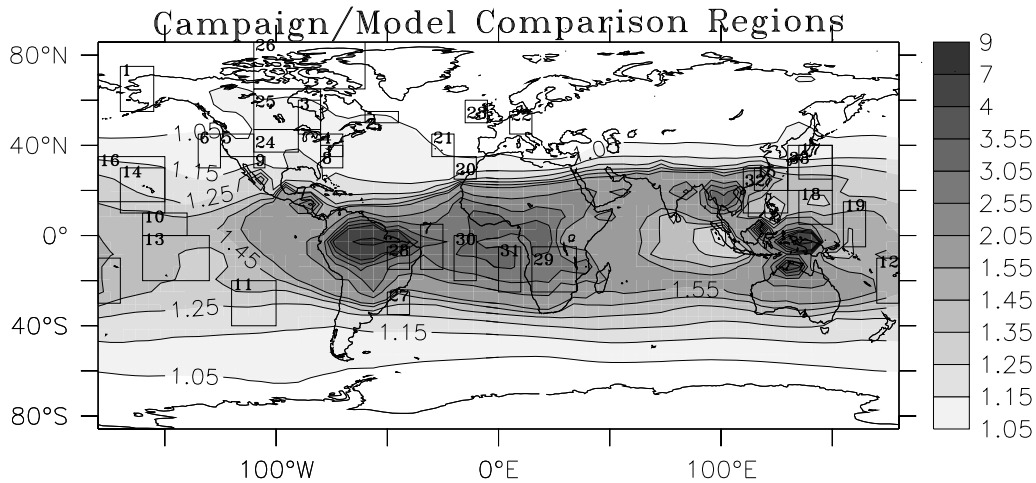


Figure 4.20: Campaign regions (within boxes), superimposed on the ratio of the annual horizontal distribution of  $\text{NO}_x$  from the PICK5 and NoLt $\text{NO}_x$  runs at 300 hPA.

output attributable to different meteorologies in different years. However, doing this would be prohibitively expensive time- and computational-wise. Furthermore, lightning produced  $\text{NO}_x$  was not the primary target species focused on for most of the campaign flight data used in this study. Measuring Lt $\text{NO}_x$  requires flying around the convective core of thunderstorms where it is produced, from the boundary layer to the upper troposphere. Flying in this type of environment demands a considerable logistical and tactical effort and also poses a risk to the airborne platform, its crew and its instruments. Thus, when comparing modeled Lt $\text{NO}_x$  enhancements with campaigns whose main target is not Lt $\text{NO}_x$ , the results may be biased by enhancements by  $\text{NO}_x$  sources other than lightning. There is little choice at present, however, except for settling to compare model results with whatever limited campaign data are available, and taking into account the biases introduced by the factors such as those described.

In this section, model output for total  $\text{NO}_x$  from the sensitivity runs carried out for this study are compared with the composites of airborne field campaign observations of Emmons *et al.* (2000). Table 4.5 and Figure 4.20 show the selected set of observation campaign regions sampled. 13 airborne campaigns sampling a total of 34 regions of the globe are included in the comparisons. In some instances, the same region was sampled more

Table 4.5: Set of campaign, dates, names of region sampled and coordinates used in this study to compare against model output.

| Campaign      | Date                     | Region name       | Coordinates, deg. |
|---------------|--------------------------|-------------------|-------------------|
| ABLE3-A       | Jul. 7- Aug. 17, 1998    | Alaska            | 55N-75N, 190-205  |
| ABLE3-B       | Jul 6- Aug. 15, 1990     | Labrador          | 50N-55N, 300-315  |
|               |                          | Ontario           | 45N-60N, 270-280  |
|               |                          | US-E Coast        | 35N-45N, 280-290  |
| CITE-2        | Aug. 11 - Sept. 5, 1986  | California        | 35N-45N, 235-250  |
|               |                          | Pacific           | 30N-45N, 225-235  |
| CITE-3        | Aug. 22 - Sept. 29, 1989 | Natal             | 15S-5N, 325-335   |
|               |                          | Wallops           | 30N-40N, 280-290  |
| ELCHEM        | Aug.                     | New Mexico        | 30N-35N, 250-255  |
| PEM-Tropics-A | Aug. 15- Oct. 5, 1996    | Christmas Island  | 0-10N, 200-220    |
|               |                          | Easter Island     | 40S-20S, 240-260  |
|               |                          | Fiji              | 30S-10S, 170-190  |
|               |                          | Tahiti            | 20S-0, 200-230    |
| PEM-Tropics-B | March. - Apr.            | Christmas Island  | 0-10N, 200-220    |
|               |                          | Easter Island     | 40S-20S, 240-260  |
|               |                          | Fiji              | 30S-10S, 170-190  |
|               |                          | Hawai             | 10N-30N, 190-210  |
| PEM-West-A    | Sept. 16- Oct.21, 1991   | Tahiti            | 20S-0, 200-230    |
|               |                          | China Coast       | 20N-30N, 115-130  |
|               |                          | Hawai             | 15N-35N, 180-210  |
|               |                          | Japan             | 25N-40N, 135-150  |
|               |                          | Philippine-sea    | 5N-20N, 135-150   |
| PEM-West-B    | Feb.7-March.14, 1994     | Pacific-Tropics-W | 5S-15N, 155-165   |
|               |                          | China Coast       | 20N-30N, 115-130  |
|               |                          | Japan             | 25N-40N, 135-150  |
|               |                          | Phillipine Sea    | 5N-20N, 135-150   |
| POLINAT-2     | Sept. - Oct.             | Canary Islands    | 25N-35N, 340-350  |
|               |                          | E-Atlantic        | 35N-45N, 330-340  |
|               |                          | Europe            | 45N-55N, 5-15     |
|               |                          | Ireland           | 50N-60N, 345-355  |
| TOPSE         | Feb.                     | Boulder           | 37N-47N, 250-270  |
|               |                          | Churchill         | 47N-65N, 250-280  |
|               |                          | Thule             | 65N-90N, 250-300  |
| TRACE-A       | Sept. 21-Oct. 26, 1992   | E-Brazil Coast    | 35S-25S, 310-320  |
|               |                          | E-Brazil          | 15S-5S, 310-320   |
|               |                          | S-Africa          | 25S-5S, 15-35     |
|               |                          | S-Atlantic        | 20S-0, 340-350    |
| TRACE-P       | Feb. - Apr.              | W-Africa-Coast    | 25S-5S, 0-10      |
|               |                          | China             | 10N-30N, 110-130  |
|               |                          | Guam              | 10N-20N, 140-150  |
|               |                          | Hawai             | 10N-30n, 190-210  |
|               |                          | Japan             | 20N-40N, 130-150  |

than once either during the same campaign (regions 13 and 14 during PEM-West B, regions 24, 25 and 26 during TOPSE, and regions 32 and 33, during TRACE-A) or during different campaigns (regions 10, 11, 12 and 13 during PEM-WEST A and B). A total of 14 regions lie altogether or partially in the tropics, (regions 7, 10, 11, 12, 13, 14, 15, 18, 19, 28, 29, 30, 31 and 32), 11 of which are marine regions (Fig 4.20). Observations for tropical continental areas, where lightning activity is prevalent and where enhancements in  $\text{NO}_x$  due to lightning are most likely to be observed, are available only for 3 regions (7, 28 and 29).

Figure 4.21-4.23 shows the vertical profiles of  $\text{NO}_x$  for the measurements of each campaign region plotted (box-whiskers plots) as well as those of the model output for the NoLt $\text{NO}_x$ , EVEN5, PICK5 and PICK20 runs for the sampled regions. The plotted runs were chosen to highlight both the differences between vertical distributions and production ranges.

One of the first things to notice is the clear lack of separation between the different modeled profiles below approximately 4 km and particularly in the midlatitudes, despite the large difference at the extremes of the range of the Lt $\text{NO}_x$  production range. This could be explained by the bias towards the tropics in flash activity in the Price and Rind (1992) parameterization, as well as by the fact that the largest enhancements in total  $\text{NO}_x$  due to Lt $\text{NO}_x$  take place in the UT, as noted in chapter 4 and earlier in this chapter. Noteworthy as well is the large scatter in the observations, particularly in the high levels (regions 9, 10, 12, 16, 18 and 19) as reflected by the error bars in the plots. This makes it particularly hard to discern a trend in the model runs that would indicate any particular run as best fitting the observations.

Starting with the 3 continental regions sampled in the tropics, it can be seen that in region 29, in South Africa, there is no clear separation of the modeled profiles save for the PICK20 run which clearly overestimates observations above 4 km. The remaining 3 runs fall within the error in the measurements. This region was sampled during the TRACE-A campaign,

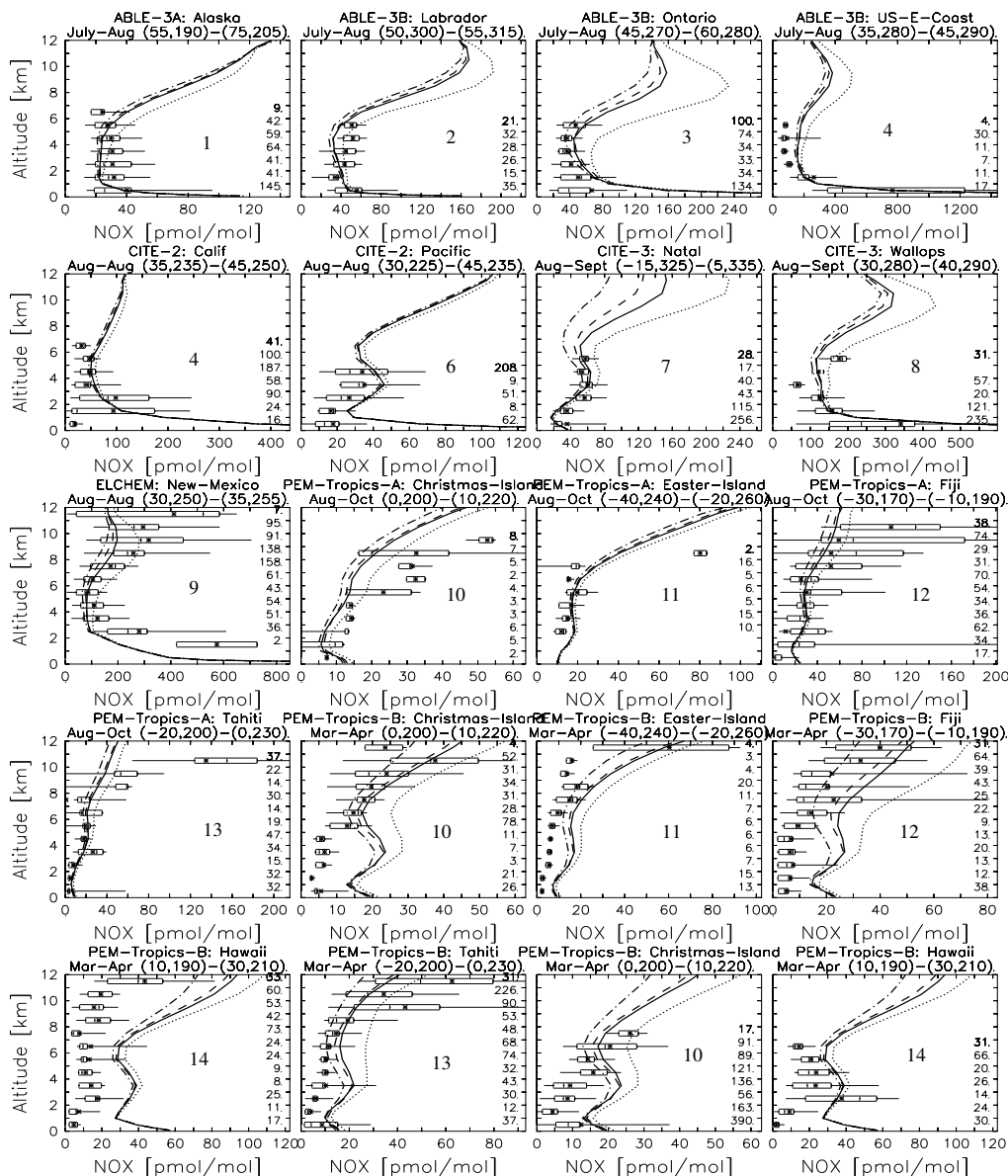


Figure 4.21: NO<sub>x</sub> profiles for different campaign regions and for NoLtNO<sub>x</sub> (dash-dotted line), EVEN5(dashed line), PICK5(solid line) and PICK20 (dotted line) runs. The boxes and whiskers contain the central and side 40% of the observations. On the right-hand side are the number of observations at each altitude. The median and mean are represented by an asterisk and vertical line, respectively. Part1.

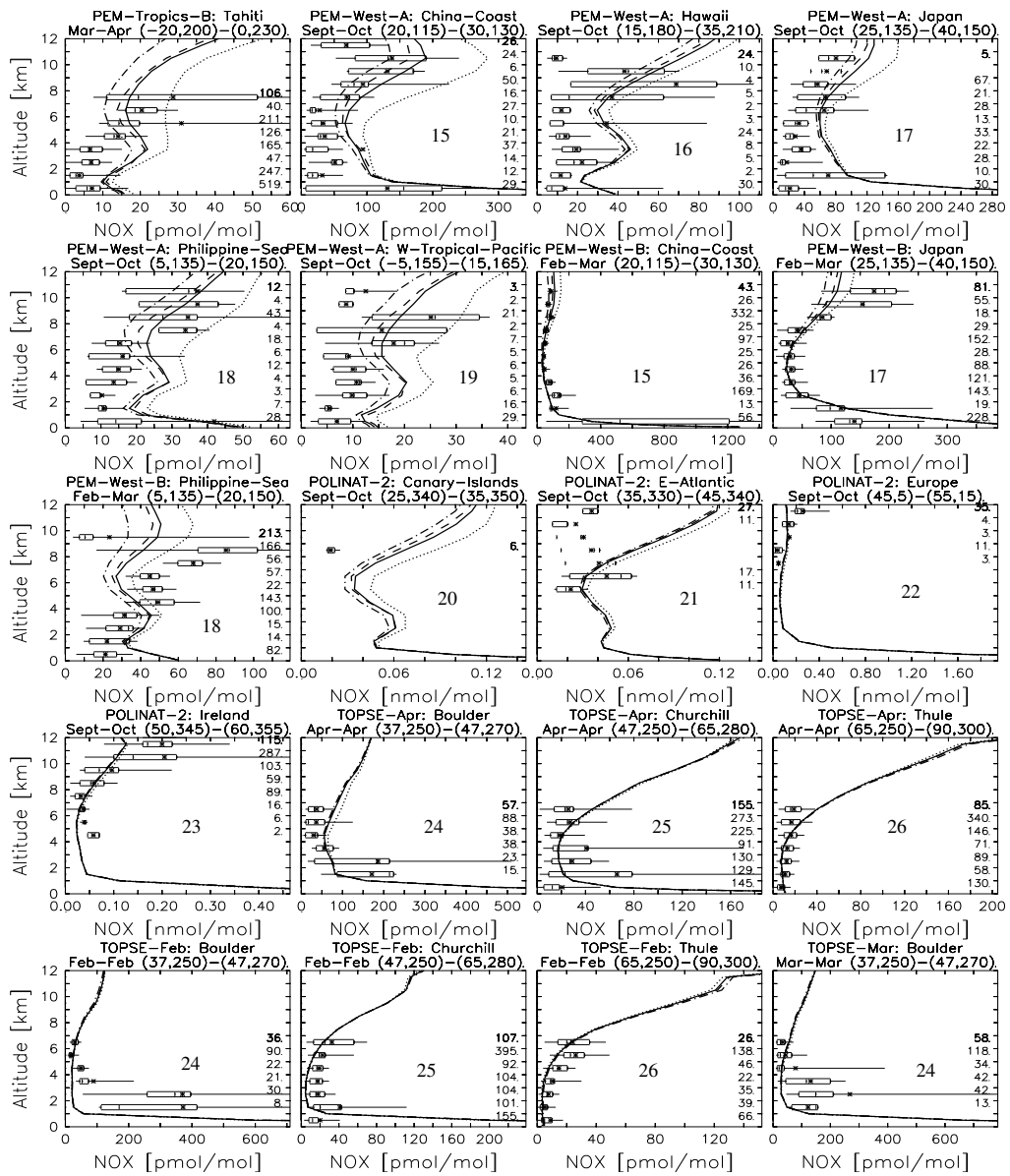


Figure 4.22: NO<sub>x</sub> profiles for different campaign regions and for NoLtNO<sub>x</sub> (dash-dotted line), EVEN5(dashed line), PICK5(solid line) and PICK20 (dotted line) runs. Part2.

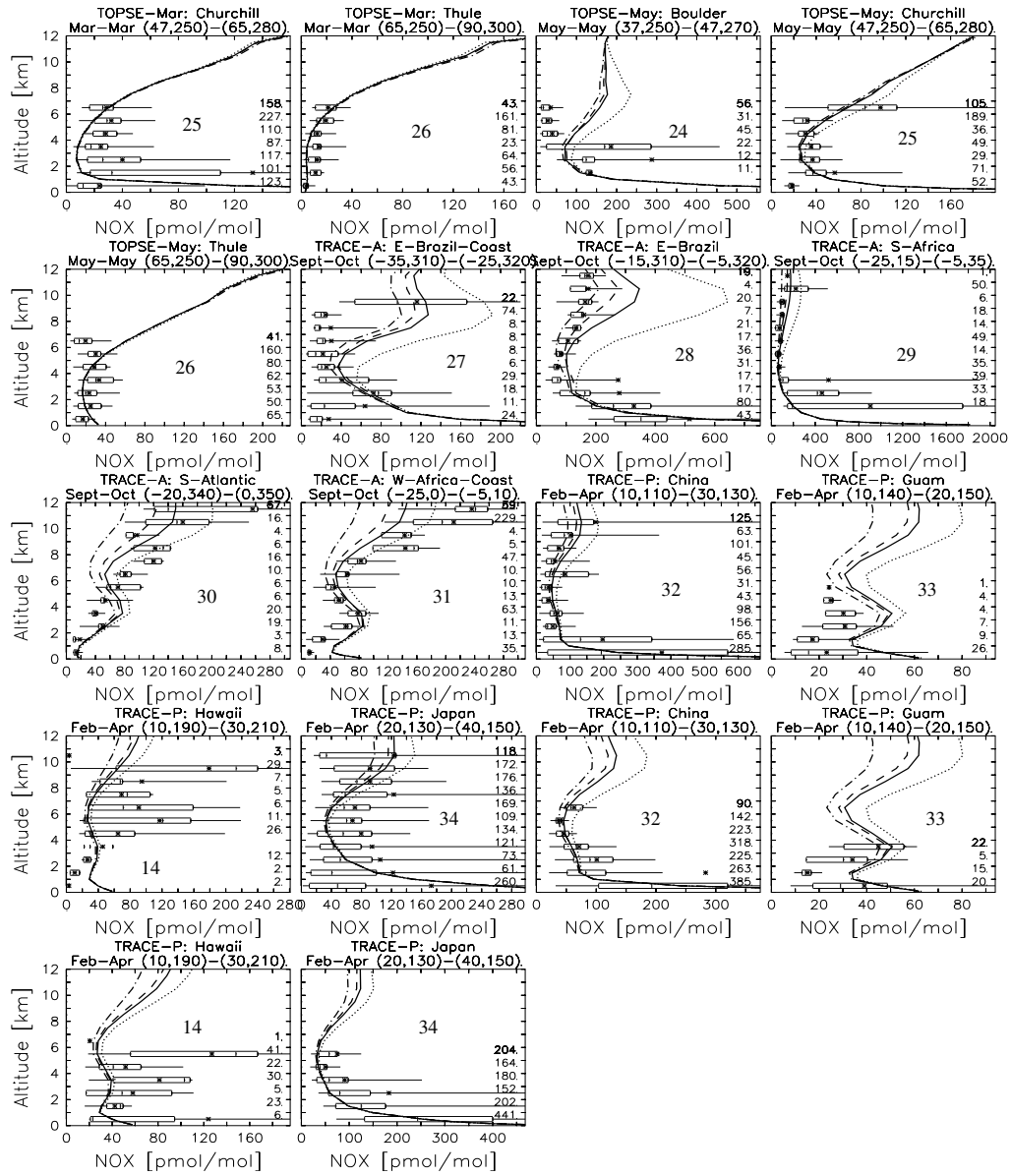


Figure 4.23: NO<sub>x</sub> profiles for different campaign regions and for NoLtNO<sub>x</sub> (dash-dotted line), EVEN5 (dashed line), PICK5 (solid line) and PICK20 (dotted line) runs. Part 3.

carried out during the dry season in South Africa (Emmons *et al.*, 2000), so enhancements in  $\text{NO}_x$  are most likely due to biomass burning emissions. In region 28, in the eastern part of Brazil, all 3 runs start to separate above  $\sim 2\text{km}$ , where the PICK20 clearly overestimates measured values. The two runs with  $5\text{ Tg(N)/yr}$  also overestimate the measurements above  $\sim 5\text{ km}$ . Interestingly, only the NoLt $\text{NO}_x$  runs stays within the error bars in the UT. The time year for the sampling of this campaign does correspond with the dry season in the area, so biomass burning emissions are a likely contributor to the profiles, probably more than Lt $\text{NO}_x$  itself. Region 7, located in the eastern coast of Brazil, shows a clear separation of the four simulations after approximately  $4\text{ km}$ , with the two runs with a  $5\text{Tg(N)/yr}$  production rate best fitting the measured profile from approximately  $4\text{ km}$  on up to the last measured data point at  $\sim 6\text{ km}$ . Within that altitude range, the NoLt $\text{NO}_x$  and PICK20 runs underestimate and overestimate the observed values, respectively. Given that the prevailing winds in that region are easterlies, the air mass is not likely to be significantly enhanced by lightning-produced  $\text{NO}_x$  from Brazil; enhancements might instead be due to biomass burning emissions from South Africa transported across the Atlantic, as the measurements were made in September and October.

The tropical marine sites sampled over the Atlantic Ocean (regions 30 and 31) show very large scatter in the data. A tendency is hard to discern as in region 30 the 3 runs with Lt $\text{NO}_x$  fall within the range of observed values. In region 31, the PICK20 run seems to best fit the observation in the UT. The relatively high  $\text{NO}_x$  values in this regions may be as a result of transport of biomass burning  $\text{NO}_x$ -rich air from the African continent, as the region was sampled during the dry season there. In the tropical Pacific (regions 10, 11, 12, 13, 15, 18, 19 and 32) a tendency is hard to discern, although the PICK20 again shows higher values than the observations. Measurements taken during the PEM-Tropics-A campaign show too much scatter and when observations are available above  $6\text{-}7\text{ km}$  all 3 runs fit the observations (regions 12 and 13). During the PEM-Tropics-B campaign, however, the PICK20 clearly overestimates the observations (regions

10, 11, 12 13 and 15).

While this tendency seems to be stronger over the tropics, it is also observed over the midlatitude continental sites. There is a clear separation of the PICK20 profile in most of the regions, as evidenced in regions 3, 7, 15 and 17. Despite the relatively large scatter in the data, it is apparent that the PICK20 run tends towards overestimation of observed values in most regions where data is available at high altitudes both in the tropics and midlatitudes.

Other than for PICK20 run, it is difficult to discern any particular trend of over- or underestimation of the model results, even when dividing the comparison between tropics and extratropics. Over the tropical continental landmasses, there is generally good agreement between modeled results and observations in the first 4 km for all 4 areas (Regions 7, 12, 13, 27,28 and 29) in the tropics. However, there is also little difference between the different model profiles up to that height, which underscores the fact that the largest differences in  $NO_x$  mixing ratios are found in the UT. The runs start to exhibit larger differences among them above about 4 km.

Figures 4.24 and 4.25 show the total  $NO_x$  scatter plots for 7 of the runs in this study, namely the NoLt $NO_x$ , EVEN2, EVEN5, PICK2, PICK5, PICK10 and PICK20 runs for data above 5km, since it is above this level that the modeled values mostly start to separate. The scatter plot for the ANVIL5 run was not included since no significant difference to the PICK5 plot is discernible. The plots are done for the entire set of airborne observation campaigns in the Emmons *et al.* (2000) dataset where  $NO_x$  measurements were available. The NoLt $NO_x$  run shows a distinct trend to underestimate observed values above approximately 40 pmol/mol.

The tendency is stronger and more apparent towards higher mixing ratios, which are computed in the UT. The plot for the PICK2 run shows a somewhat better fit than the EVEN2 plot. Since the difference between the two distribution is the weighting of the PICK2 run towards the higher levels, it can be speculated that it is this weighting that accounts for the

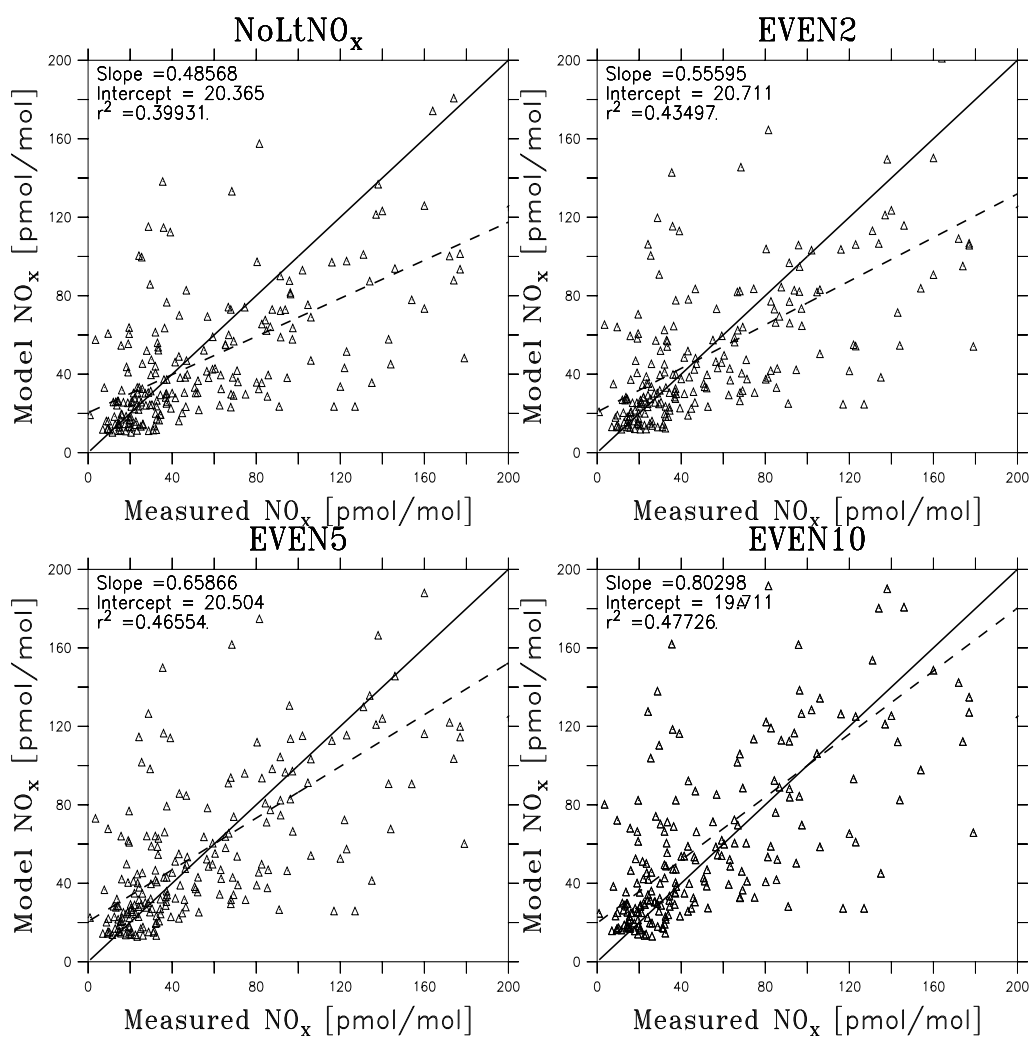


Figure 4.24: Scatter plots of the NoLt $\text{NO}_x$ , EVEN2, EVEN5, and EVEN10 runs against airborne observation campaign data above 5km.

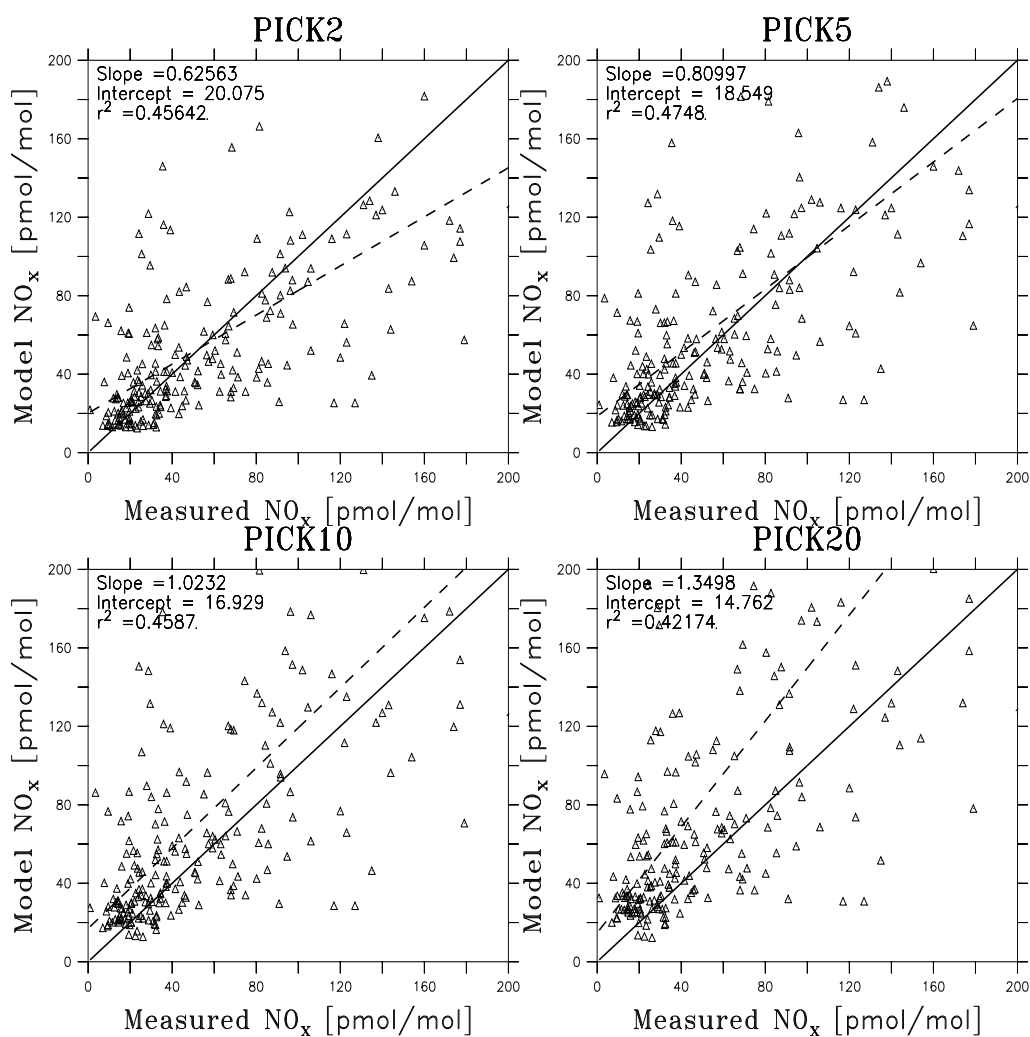


Figure 4.25: Scatter plots of the PICK2, PICK5, PICK10 and PICK20 runs against airborne observation campaign data above 5 km.

best fit. The PICK5 run shows the best fit of all runs, both burden- and distribution-wise, although the EVEN5 run shows a very similar correlation coefficient ( $r^2=0.4655$ ) but a lower slope (0.65866). It is interesting to notice that, in spite of these two runs having markedly different  $\text{NO}_x$  vertical distributions, the difference in the scatter plots is small. This is due to the lack of observations at key locations where the largest differences could be expected. The EVEN10 and PICK10 scatter plots result in very similar correlation coefficients;  $r^2=0.47726$  and  $r^2=0.4587$ , respectively. The plots suggest that the EVEN10 run fits the observations quite well for mixing ratios in the 90 pmol/mol range and slightly underestimating and overestimating for lower and higher concentrations, respectively. The PICK10 run overestimates the observed values in the entire range. The PICK20 run shows an even clearer tendency to overestimate the observations data throughout the entire range, particularly at the upper end, confirming the tendency already seen in the vertical profile plots.

The effects of the vertical distribution and source magnitude of  $\text{LtNO}_x$  have been addressed before in a number of modeling studies. In Chapter 5, the importance of the vertical distribution of  $\text{LtNO}_x$  is discussed in more detail. Tie *et al.* (2001) and Stockwell *et al.* (1999) point out that including lightning- $\text{NO}_x$  emissions in their models produces better agreement with observations. In another study, Tie *et al.* (2002) conclude, based on vertical profile plots, that simulations with a production of 7 Tg(N)/yr of  $\text{NO}_x$  from lightning uniformly distributed in clouds, and 3.5 Tg(N)/yr in the upper regions of clouds produce the best agreement with observations. In this study, however, it was found with the use of scatter plots, which provide a more objective means of comparing observed and modeled data, that a 5 Tg(N)/yr production rate using the Pickering *et al.* (1998) vertical distribution comes closest to the observations. The differences between the modeled results in this work and those in Tie *et al.* (2002) can be attributed to a number of causes. Tie *et al.* (2002) compare their model data with 14 sites, all close to active lightning regions, whereas for this study 33 regions from the same dataset have been compared. The extra number of sites,

some sampled more than once, provide more data to drive the comparisons. Similarly, the use of different models, and different convection parameterizations, particularly the use of only the simple Hack (1994) convection scheme in Tie *et al.* (2002), is fundamental in accounting for these differences since it is unable to simulate deep convective mixing well.

From the results in this study one can contend that it is not possible, based on the information provided by vertical profiles alone, to arrive at a solid conclusion as to which LtNO<sub>x</sub> production range best fits the observations because of the uncertainties introduced by the low availability of observational data, particularly in critical areas, such as the continental tropics, the large scatter in the available observations and the many uncertainties in modeling LtNO<sub>x</sub> and other NO<sub>x</sub> sources. While scatter plots afford an extra measure of objectivity to the analysis, it can only be said with confidence that, in the simulations presented here, the NoLtNO<sub>x</sub> and PICK20 runs underestimate and overestimate, respectively, the observations enough not to be considered as realistic assumptions. More observations campaigns, such as TROCCINOX (Tropical Convection, Cirrus and Nitrogen Oxides Experiment, Brazil, Feb.-March 2004) and the upcoming TROCCINOX II (Feb.-March 2005), specifically aimed at reducing the uncertainties in the source of NO<sub>x</sub> from lightning in key regions, such as the tropical continents, are therefore needed in order to reduce these uncertainties.

## Chapter 5

# Importance of the Vertical Distribution of the Source of NO<sub>x</sub> from Lightning

After showing the basic importance of the source of NO<sub>x</sub> from lightning in tropospheric chemistry in the previous chapters, an important remaining task is to examine the sensitivity of lightning-produced NO<sub>x</sub> to its vertical distribution, which turns out to be quite substantial. This chapter gives a brief overview of these findings, based on Labrador *et al.* (2004a). As discussed before, there is a great deal of uncertainty in the magnitude of the source of NO<sub>x</sub> from lightning. It is very important to determine accurate budgets for LtNO<sub>x</sub> if the total NO<sub>x</sub> budget is to be accurately calculated in turn. However, not only the burden, but also the vertical distribution of LtNO<sub>x</sub> after it is produced in and around thunderclouds is a crucial factor in determining an accurate budget of LtNO<sub>x</sub>, since its lifetime shows a strong dependency on height. One might pose the question, what happens to LtNO<sub>x</sub> once it is produced by a flash of lightning? Does convection act to take it to upper portions of the cloud? If so, how much of it? Do downdrafts carry some of it downward to the boundary layer? Although some studies, both theoretical and experimental, have been made to try to answer these questions, no firm conclusions have yet been reached. In trying to pro-

vide information that could be used in answering these questions, a series of runs were made for this study with MATCH-MPIC wherein 3 different assumptions concerning the vertical placement of LtNO<sub>x</sub> were tested. One distributes LtNO<sub>x</sub> density-weighted, keeping the mixing ratio of the new NO<sub>x</sub> production constant through the vertical cloudy column. This distribution is based on the findings of Goldenbaum and Dickerson (1993), where NO<sub>x</sub> production by lightning apparently exhibits a strong dependence on the ambient air density, being less for lower densities, and the assumption that the higher frequency of IC flashes is approximately balanced by their lower energies. A second distribution constrains LtNO<sub>x</sub> in the five uppermost vertical levels of the cloud column, simulating transport to the anvil region of the thunderstorm. Finally a distribution based on the LtNO<sub>x</sub> vertical profiles developed by Pickering *et al.* (1998), in which the effects of convection and downdraft are taken into account in the redistribution of LtNO<sub>x</sub>. In this chapter the effects of these assumption on tropospheric chemistry are discussed by studying the effects on total NO<sub>x</sub>, O<sub>3</sub>, OH, HNO<sub>3</sub> and PAN. For that purpose, the run with a 5Tg(N)/yr LtNO<sub>x</sub> production rate is used as the standard run, since it probably best reflects the most accepted production rate. The vertical distribution profiles studied herein are discussed in sections 2.3.5 and 2.4 of Chapter 2 and pictured in Fig. 2.1

## 5.1 Effects on NO<sub>x</sub>

Common to all three distributions is that the largest enhancements in all of these species occur in the tropical UT, between approximately 500 and 300 hPa, with significant differences in the magnitude and the vertical extent of the enhancements. The EVEN5 distribution (Fig. 5.1c) results in a rather gradual enhancement in NO<sub>x</sub> with altitude, consistent with a density-weighted distribution, reaching a maximum of a factor of 2 higher than the NoLtNO<sub>x</sub> run between approximately 300 and 400 hPa above the equator. It is interesting to remark that, despite an even mixing ratio in the vertical, the enhancements are simulated in this distribution in the UT. This is a

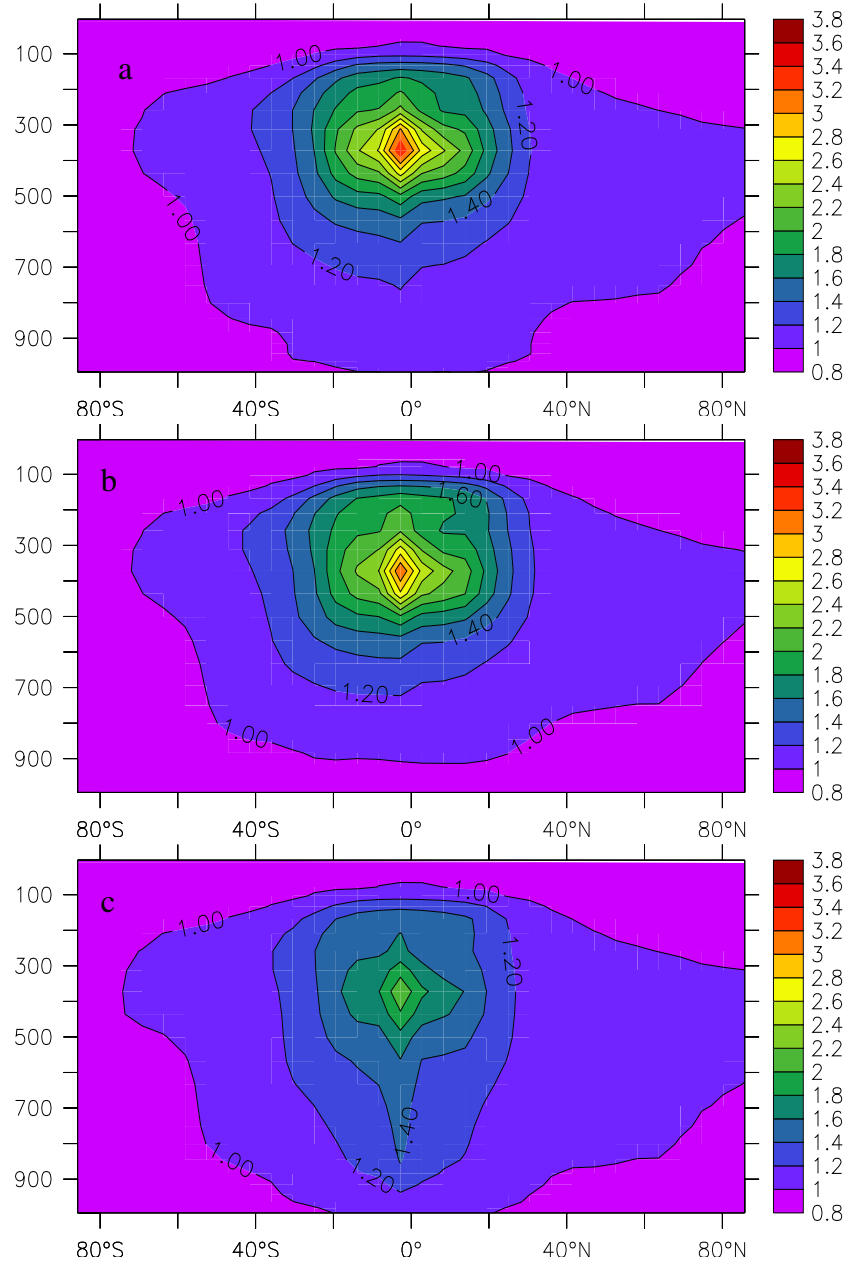


Figure 5.1: Ratios of the annual zonal means of the PICK5 (a), ANVIL5 (b) and EVEN5 (c) runs to the  $\text{NoLtNO}_x$  run for total  $\text{NO}_x$ .

clear manifestation of the longer lifetimes of  $\text{NO}_x$  in the UT. The PICK5 and ANVIL5 runs (Figs 5.1a and 5.1b, respectively), simulate very similar enhancements to each other, although the ANVIL5 run, more weighted toward the UT, simulates a reduction below 900 hPa at all latitudes and no evident enhancement below 800 hPa, in agreement with its definition. The maximum zonal mean enhancement in these two runs is about a factor of 3 higher than the mixing ratios of the NoLt $\text{NO}_x$  run at 300-400 hPa. Accounting for the uplifting by convection in the PICK5 and ANVIL5 runs results in twice the enhancement of  $\text{NO}_x$  in the UT compared to the EVEN distributions, a significant result considering that all three runs were done with the same 5 Tg(N)/yr Lt $\text{NO}_x$  production rate. In all three runs, decreases in total  $\text{NO}_x$  are computed at the surface in the extratropics and even in the tropics in the ANVIL5 run. As discussed in the previous chapter, this is mainly due to downward transport of ozone produced by enhanced  $\text{NO}_x$  in the UT, reducing the near-surface  $\text{NO}_x$  lifetime. Though one could also consider near-surface production of ozone, the computed reductions in surface  $\text{NO}_x$  make this unlikely.

Interestingly, the difference in the total  $\text{NO}_x$  burden for equivalent production ranges between the PICK and EVEN distributions increases with increasing Lt $\text{NO}_x$  production rates: relative to the NoLt $\text{NO}_x$  run, the PICK2 run simulates a total  $\text{NO}_x$  burden 2.5% larger than that of the EVEN2 run. For the 5 and 10 Tg(N)/yr production rates, these differences are 3.5 and 5.3, respectively. This is as a consequence of the weighting of the PICK distribution towards the higher altitudes where  $\text{NO}_x$  competes more effectively with other sources, as opposed to the even (density-weighted) EVEN distribution. These differences are in the UT, particularly in the tropics and consistent with the larger amounts of Lt $\text{NO}_x$  deposited in the upper levels by the PICK distribution.

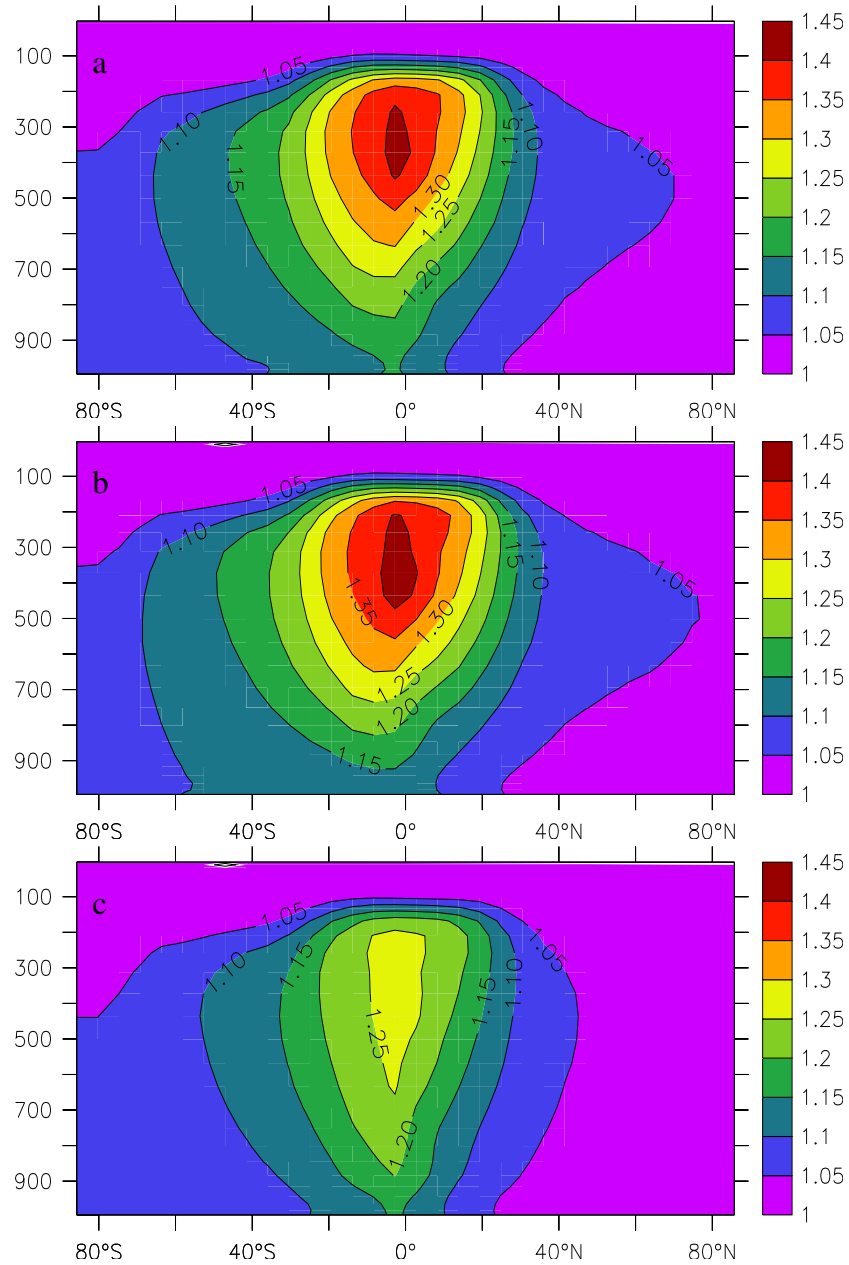


Figure 5.2: Ratios of the annual zonal means of the PICK5 (a), ANVIL5 (b) and EVEN5 (c) runs to the NoLtNO<sub>x</sub> run for O<sub>3</sub>.

## 5.2 Effects on O<sub>3</sub>

Much like with NO<sub>x</sub>, a gradual vertical enhancement of ozone is simulated in the EVEN5 run (Fig. 5.2), with the largest enhancements occurring at the tropical latitudes. Surface enhancements range from 12% within the tropics to ~ 4% at high latitudes. The peak zonal mean enhancement is approximately 30% with respect to the NoLtNO<sub>x</sub> run between 200 and 700 hPa in the tropics. Again, the PICK5 and ANVIL5 runs (Figs. 5.2 a and 5.2b, respectively) simulate very similar profiles to each other except at surface levels, where the PICK5 run results in an enhancement of up to 15% close to the equator and ~ 10% in the tropical regions, compared to a maximum zonal mean surface layer enhancement of 10% in the ANVIL5 run for most of the tropics. The largest enhancements in both runs are simulated between 200 and 400 hPa over the tropics with 45% more ozone compared to the NoLtNO<sub>x</sub> run. The general differences in tropospheric ozone as a result of the different vertical placements emphasizes the role of NO<sub>x</sub> in controlling the ozone budget, and underscores the need not only to determine an accurate estimate of the LtNO<sub>x</sub> source magnitude, but also to correctly assess its post-storm vertical distribution.

## 5.3 Effects on OH

As discussed previously there is a significant impact on OH by LtNO<sub>x</sub>. In the EVEN5 run (Fig. 7c), zonal mean enhancements of up to 60% with respect to the NoLtNO<sub>x</sub> run are simulated in the tropical UT, mainly in the narrow altitude band between 300 and 100 hPa. Again the PICK5 and ANVIL5 runs (Figs. 5.3a and b, respectively) show very similar profiles for OH, with enhancements of approximately 100% between 100 and 200 hPa. These two distributions therefore simulate enhancements of OH close to 40% larger than the EVEN distribution with respect to the NoLtNO<sub>x</sub> run. All three runs also predict enhancements of about 10% near the surface in the tropics. This is probably to be expected, since water vapor contents

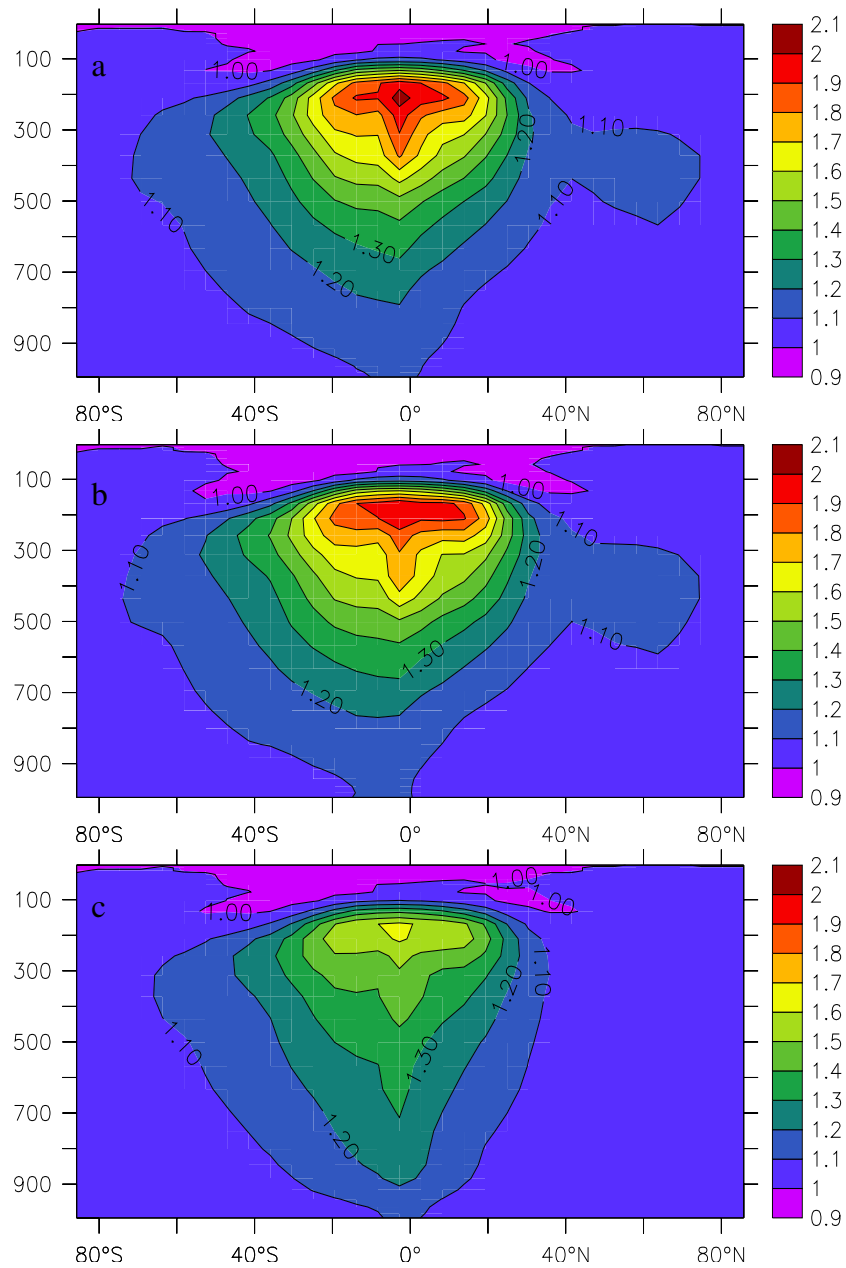


Figure 5.3: Ratios of the annual zonal means of the PICK5 (a), ANVIL5 (b) and EVEN5 (c) runs to the NoLtNO<sub>x</sub> run for OH.

are higher in the tropical LT. What is interesting to notice is that this enhancement is also present in the ANVIL distribution, which simulates no LtNO<sub>x</sub> enhancements at the surface. OH enhancements there can be expected to be as a result surface enhancements of O<sub>3</sub> (see Fig.4.3), brought on by convective mixing of the species originally produced by LtNO<sub>x</sub> aloft, as discussed in section 4.1.1 of Chapter 4.

## 5.4 Effects on HNO<sub>3</sub>

Not only does HNO<sub>3</sub> show a strong sensitivity to increases in the source of NO<sub>x</sub> from lightning as discussed in the previous chapter, but differences in the vertical placement also affect the annual average concentrations of the species considerably, as seen in Figs. 5.4a, b and c. The final post-storm vertical placement of HNO<sub>3</sub> can have definite impact on the ultimate fate of the species: higher concentrations in the lower troposphere make nitric acid more susceptible to loss via wet and dry deposition. On the other hand, enhancements in the UT, where rainout of the species is much less effective, have the potential to turn nitric acid into an effective reservoir species of NO<sub>x</sub>. Furthermore, in the UT, nitric acid becomes subject to long range transport by large scale circulation patterns. Compared to the NoLTNO<sub>x</sub> run, the PICK and ANVIL distribution simulate considerably larger enhancements than the EVEN distribution by virtue of being more weighted towards the UT. The PICK and ANVIL runs simulate maximum enhancement factors approximately 150% larger than those of the EVEN distribution. The main difference between the PICK and ANVIL distributions (Figs. 5.4a and 5.4b, respectively) is that the former simulates 10-20% larger concentrations at the surface than the ANVIL distribution, as a result of the PICK distribution prescribing some NO<sub>x</sub> placement at surface levels. From all three distributions, it can also be observed that, compared to most other trace gases discussed, the maximum enhancements in nitric acid occur at a somewhat lower altitude i.e., between 400 and 500 hPa. Two main reasons could account for this fact: first, while the largest relative in-

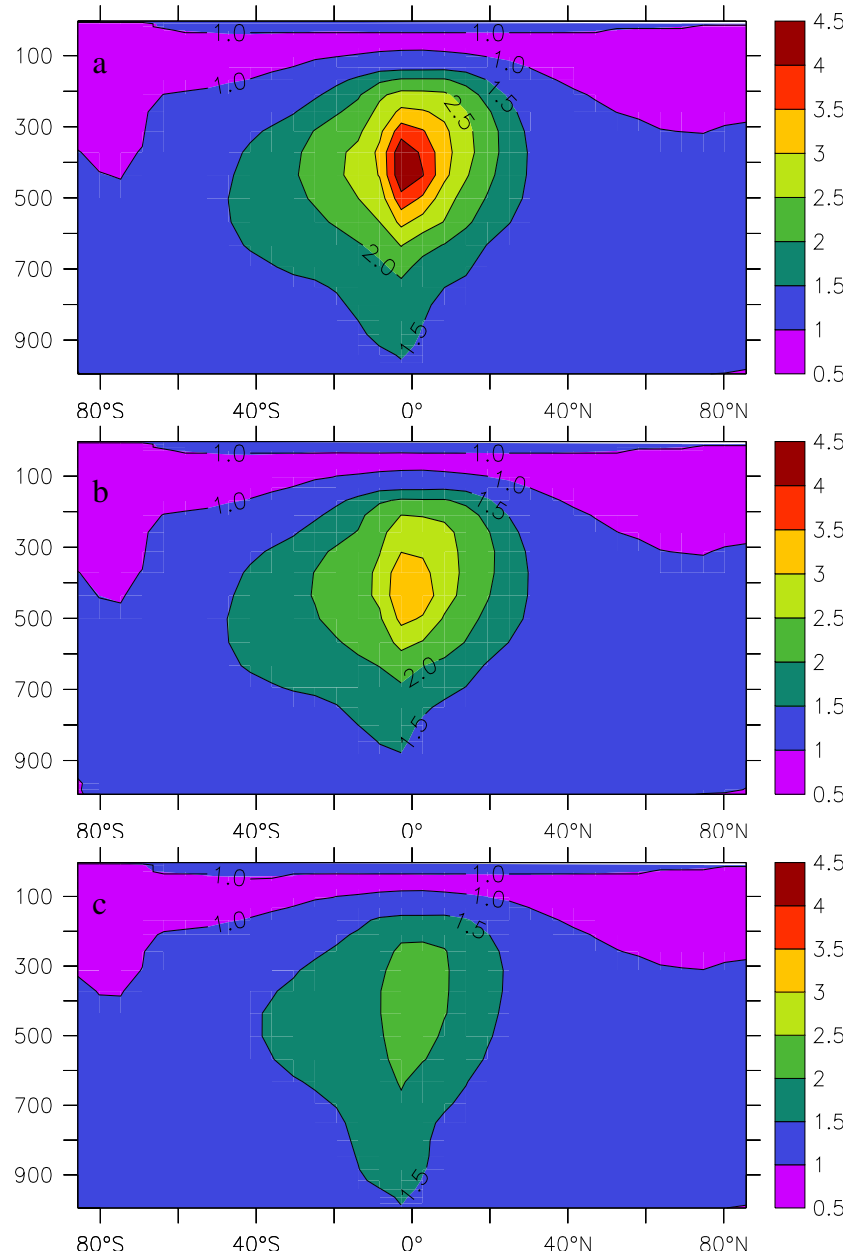


Figure 5.4: Ratios of the annual zonal means of the PICK5 (a) , ANVIL5 (b) and EVEN5 (c) runs to the NoLt $\text{NO}_x$  run for  $\text{HNO}_3$ .

crease in OH, a direct precursor of  $\text{HNO}_3$ , by adding  $\text{LtNO}_x$  occurs in the UT, the largest absolute enhancement occurs at a lower altitude (Labrador *et al.*, 2004b), coinciding with the maximum enhancement in nitric acid. Second, in the UT, there is a buffering effect of PAN, which is enhanced at the expense of nitric acid.

## 5.5 Effects on PAN

As shown in Figure 9a, the burden of PAN is doubled in the tropical UT by assuming the PICK5 lightning  $\text{NO}_x$  vertical distribution. The EVEN5 run (Fig. 5.5c) simulates increases of over 50% from 500 hPa up to tropopause level over the tropics, where values peak at a factor of 1.6 versus the NoLt $\text{NO}_x$  run. The PICK5 and ANVIL5 runs (Figs. 5.5a and 5.5b, respectively) show again a very similar pattern. Maximum enhancements are of the order of 100% between  $\sim 300$  and 200 hPa in both distributions, with enhancements decreasing rapidly outside of the tropical latitudes. All three distribution simulate enhancements in PAN in the UT, as a result of increases in  $\text{NO}_x$  in the same region. The ANVIL5 run simulates no notable enhancement at the surface, whereas the PICK5 run shows a 10% enhancement, consistent with the placement of  $\text{NO}_x$  by the PICK98 profiles in the lowermost troposphere.

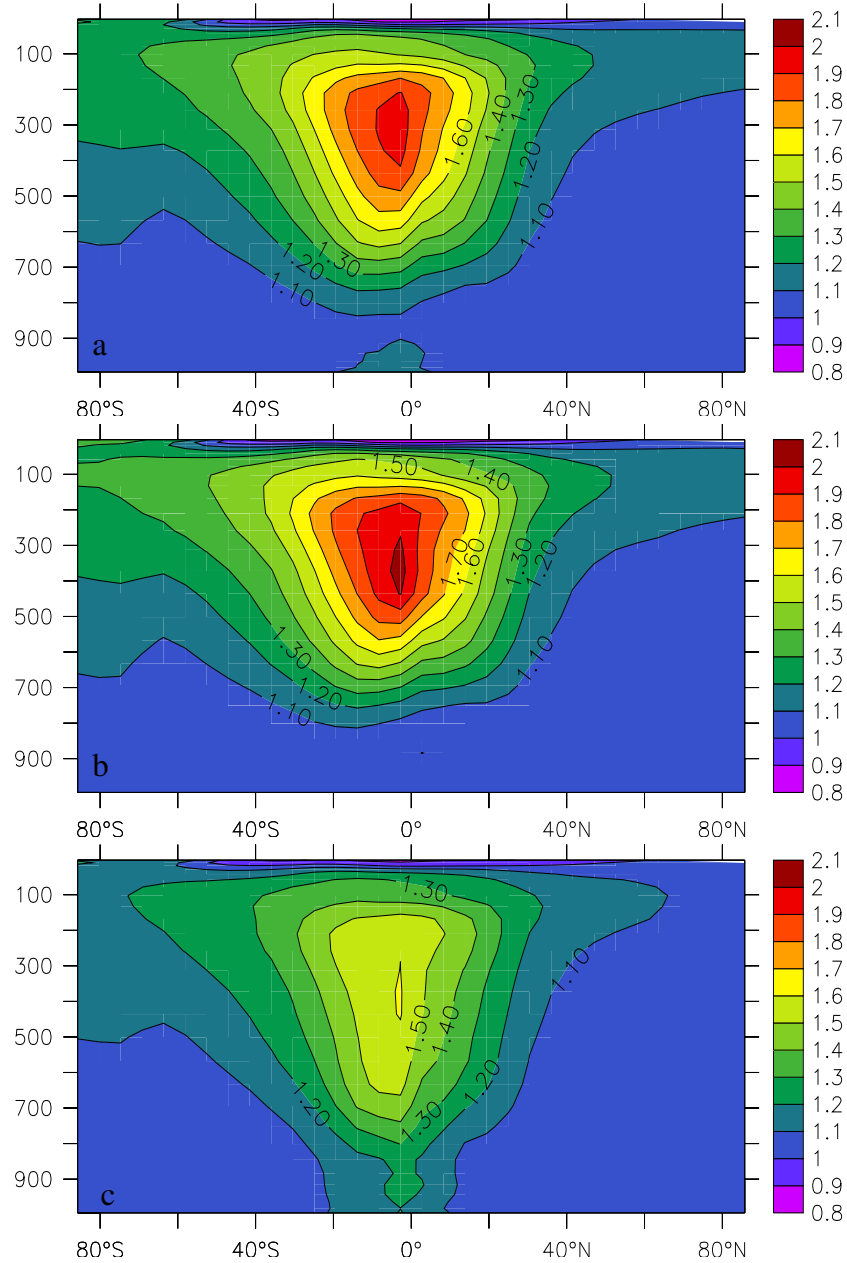


Figure 5.5: Ratios of the annual zonal means of the PICK5 (a), ANVIL5 (b) and EVEN5 (c) runs to the NoLtNO<sub>x</sub> run for for PAN.



# Chapter 6

## Conclusions

In order to determine an accurate budget of tropospheric ozone, it is first necessary to determine an accurate budget of tropospheric  $\text{NO}_x$ . Of all the various sources, the source of  $\text{NO}_x$  from lightning ( $\text{LtNO}_x$ ) has the largest uncertainty, with estimates of its production ranging from 2-20  $\text{Tg(N)}/\text{yr}$ . The reason for this large uncertainty stems in turn from the various uncertainties associated with the production of NO in the violent environment of thunderstorms, such as the partitioning between cloud-to-ground, intracloud and intercloud discharges, the energy produced by each type of lightning discharge, the amount of NO molecules produced per unit flash energy and the global distribution of lightning flashes.

These uncertainties involve processes that span many orders of magnitudes both in time and space. On microphysical scales, the charge separation in thunderstorms due to hydrometeor collisions leads to the production of the lightning discharge, and the actual production of NO molecules occurs in the hot lightning channel, on a time scale of milliseconds. Medium scale temporal and spatial processes include the in-cloud vertical distribution and transport of  $\text{NO}_x$ , of the order of a few kilometers and measured in minutes to hours. On the global scale, thunderstorm activity is determined by processes such as synoptic scale weather systems and global circulation patterns and is measured in thousand of kilometers and days or even months.

Given the difficulty in observing and measuring these processes, global models are a valuable tool for studying  $\text{LtNO}_x$  and its impact on tropospheric chemistry. In this study, a series of sensitivity simulations was conducted wherein different assumptions concerning the burden of  $\text{LtNO}_x$  and its vertical placement have been tested using the Model of Atmospheric Transport and Chemistry, in its Max Planck Institute for Chemistry version, or MATCH-MPIC. The sensitivity to  $\text{LtNO}_x$  was examined for  $\text{NO}_x$ ,  $\text{O}_3$ , OH,  $\text{HNO}_3$  and PAN.

The model uses the cloud-top height based lightning parameterization by Price and Rind (1992). When compared with satellite observations, it was found that the parameterization has a systematic tendency to underestimate flash densities in the midlatitudes and tropical marine areas, while at the same time overestimating flash densities in the tropical continental regions. A first implementation of the Allen and Pickering (2002) convective mass-flux based lightning parameterization has been evaluated in MATCH-MPIC. It was found that the parameterization produces a clear overestimation, of at least one order of magnitude, of marine lightning, while on the other hand underestimating continental flash densities, particularly in the tropics. Given the basic quality of the Price and Rind (1992) parameterization and the significant number of steps necessary to develop an improved version thereof, it was decided to conduct the sensitivity studies in this work using the PR92 parameterization.

The source of  $\text{NO}_x$  from lightning has a notable impact on trace gas tropospheric chemistry, particularly in the tropical regions where over 70% of the global lightning activity occurs. Compared to a run with  $\text{LtNO}_x$  turned off, enhancements in total  $\text{NO}_x$  for a run with a production rate of 5 Tg(N)/yr are of the order of 20% globally and 36% in the tropics. For  $\text{O}_3$ , enhancement are 14% and 20% for the whole globe and the tropics, respectively. The runs showed that, as the source magnitude was increased, the response showed a saturation signal for all trace species studied, save for  $\text{HNO}_3$ , which showed an approximately linear increase response throughout the source strength range. This response is due to the fact that  $\text{LtNO}_x$

---

enhances  $\text{NO}_2$  as well as another direct precursor of  $\text{HNO}_3$ , namely the OH radical. Most of the enhancements simulated take place in the tropical UT, where the trace gas lifetimes are increased and where the potential for long-range transport is larger, which may result in increased levels of both  $\text{NO}_x$  and  $\text{O}_3$  in areas with relatively low background concentrations of those species.

OH radical concentrations showed a strong sensitivity to increases in  $\text{LtNO}_x$ , larger than that of  $\text{O}_3$  (Labrador *et al.*, 2004b). This implies that  $\text{LtNO}_x$  might have the capacity to indirectly affect the oxidizing efficiency of the troposphere; however, it is not clear if this impact will be significant given that, in this study, the largest enhancements in OH due to  $\text{LtNO}_x$  occur in the UT, where colder temperatures make most photooxidation reactions less efficient. Perhaps for this reason, the impact on OH and the oxidizing efficiency of the atmosphere has received little attention in previous literature which has mostly emphasized the effects on  $\text{O}_3$ . By comparing the changes in the lifetimes of two long-lived trace gases, namely  $\text{CH}_4$  and  $\text{CH}_3\text{CCl}_3$ , reductions of the order of 15% were computed in both species in a run with 5 Tg(N)/yr, compared to a run with no  $\text{LtNO}_x$ . This is as large as the relative impact on the  $\text{O}_3$  burden. The simulations with MATCH-MPIC using the maximum and minimum  $\text{LtNO}_x$  sources lead to uncertainties in the lifetimes of both  $\text{CH}_4$  and  $\text{CH}_3\text{CCl}_3$  about as large as those in recent studies in the literature. Based on this, one could be tempted to say that improved estimates of the lifetimes of trace gases such as both  $\text{CH}_4$  and  $\text{CH}_3\text{CCl}_3$  could be used to constrain the source of  $\text{NO}_x$  from lightning. However, due to many other uncertainties involved in a global model, this is not currently practical. While future reductions of these uncertainties will certainly lead to more precise estimates of the effects of  $\text{LtNO}_x$  on OH and the tropospheric oxidizing efficiency, they are unlikely to change the main conclusion, namely that it will be important to consider the impact of  $\text{LtNO}_x$  on OH and the oxidizing efficiency of the troposphere alongside that on  $\text{O}_3$  in future studies.

The series of trace gases studied also showed a considerable sensitivity

to different assumptions concerning the vertical placement of  $\text{LtNO}_x$ . The Pickering (C-shaped) and Anvil (five topmost layers of the cloud) distributions, both of which place a large portion of  $\text{NO}_x$  in the upper portions of the cloud, resulted in enhanced levels of most trace gases in those levels, compared with the density-weighted EVEN distribution. Although observations suggest that the post-storm distribution of tracers is different than what a density-weighted distribution would suggest, more observations are needed to determine which assumptions best fit the actual distribution profile.

Comparison with data from observation campaigns constitute the best way to evaluate model results. In the specific case of  $\text{LtNO}_x$ , however, the number of uncertainties associated with the production of the species as well as the few data available and the large scatter present in them does not make it possible to discern a single “best” production rate for  $\text{LtNO}_x$  based on comparisons with observed data alone, although the 0 and 20  $\text{Tg(N)}/\text{yr}$  sources can be ruled out as generally underestimating (too low) or overestimating (too high) (Labrador *et al.*, 2004a). In particular, there are too few observations in key regions, especially in the tropics, where lightning is prevalent, suggesting the need for future field campaigns in these regions.

## Outlook

While the uncertainties associated with the source of  $\text{NO}_x$  from lightning are manifold, in the future the situation could be, if not entirely resolved, at least greatly improved with simultaneous attacks from two fronts: Improved lightning parameterizations and more observations campaigns specifically targeting lightning-produced nitrogen oxides. The first front implies a better understanding of the microphysics of convection, cloud formation, lightning generation and production of  $\text{NO}$  by lightning discharges. As one expert in the field pointed out, substantial improvement in lightning flash rate parameterizations may have to wait until more detailed cloud microphysics data are available from next-generation convection param-

eterizations (Kenneth A. Pickering, personal communication, 2004). On the other front, additional measurement campaigns, such as TROCCINOX (Feb.-Mar. 2004) and TROCCINOX II (Feb.-Mar. 2005), specifically designed to target lightning-produced  $\text{NO}_x$  and in key regions, such as the tropical continental landmasses, are needed to provide the data against which model results can be evaluated.



# Bibliography

- Allen, D., and Pickering, K., 2002: Evaluation of lightning flash rate parameterizations for use in a global chemical transport model. *J. Geophys. Res.*, 107(D23), 4711, doi:10.1029/2002JD002066.
- Barnes, S L, and Newton, C W., 1982: *Thunderstorms in the synoptic setting*. Vol. 2 edited by E. Kessler, U.S. Dept. of Commer., Washington, D.C. Pages 109–171.
- Bates, T. S., Kelly, K. C., Johnson, J. E., and Gammon, R. H., 1995: Regional and seasonal variations in the flux of oceanic carbon monoxide to the atmosphere. *J. Geophys. Res.*, 100, 23093–23101.
- Baughcum, S. L., Henderson, S. C., Hertel, P. S., Maggiora, D. R., and Oncina, C. A., 1994: *Stratospheric emissions effects database development*. Contr. Rep. CR-4592. NASA.
- Boccipio, D J, Goodman, S J, and Heckman, S., 2000: Regional differences in tropical lightning distributions. *J. Appl. Met.*, 39, 2231–2248.
- Bode, K., Helas, G., and Kesselmeier, J., 1997: *Biogenic contribution to atmospheric organic acids*. SPB Academic Publishing by Pages 157–170.
- Bonsang, B., Kanakidou, M., Lambert, G., and Monfray, P., 1988: The marine source of C<sub>2</sub>–C<sub>6</sub> aliphatic hydrocarbons. *J. Atmos. Chem.*, 6, 3–20.
- Chameides, W. L., 1979: Production of CO, H<sub>2</sub>, and other trace gases by atmospheric lightning. *Transactions, Amer. Geophys. Un.*, 59(12), 1150–1150.

- Chameides, W. L., Davis, D. D., Bradshaw, J., Rodgers, M., Sandholm, S., and Bai, D. B., 1987: An estimate of the  $\text{NO}_x$  production-rate in electrified clouds based on NO observation from the GTEs CITE-1 fall 1983 field operation. *J. Geophys. Res.*, 92(D2), 2153–2156.
- Chameides, W.L., Stedman, D.H., Dickerson, R.R., Rusch, D.W., and Ciccerone, R.J., 1977:  $\text{NO}_x$  production in lightning. *J. Atmos. Sci.*, 34(1), 143–149.
- Christian, H. J., Blakeslee, R. J., Goodman, S. J., Mach, D. A., Stewart, M. F., Buechler, D. E, Koshak, W. J., Hall, J. M., Boeck, W. L., Driscoll, K. T., and Boccippio, D. J., 1999: The Lightning Imaging Sensor. *Proc. of 11th internat. conf. on atmp. electricity, Guntersville, Alabama*, 746–749.
- Christian, H. J., Blakeslee, R. J., Boccippio, D. J., Boeck, W. L., Buechler, D. E., Driscoll, K. T., Goodman, S. J., Hall, J. M., Koshak, W. J., Mach, D. M., and Stewart, M. F., 2003: Global frequency and distribution of lightning as observed from space by the Optical Transient Detector. *J. Geophys. Res.*, 108(D1), 4005, doi:10.1029/2002JD002347.
- Corbett, J. J., Fischbeck, P. S., and Pandis, S. N., 1999: Global nitrogen and sulfur inventories for oceangoing ships. *J. Geophys. Res.*, 104, 3457–3470.
- Cramer, J. A., and Cummins, K. L., 1999: Long range trans-oceanic lightning detection. *Pages 250–253 of: Proceedings from the 11th International Conference Atmospheric Electricity, Guntersville, Alabama, NASA/CP-1999-2092601, NASA, Washington, D.C.*
- Crawford, J., *et al.*, 1996: Photostationary state analysis of the  $\text{NO}_2$ -NO system based on airborne observations from the western and central North Pacific. *J. Geophys. Res.*, 101, 2053–2072.
- Crutzen, P. J., 1972: *Gas-phase nitrogen and methane chemistry in the atmosphere*. Report AP-10. University of Stockholm.

- Crutzen, P. J., 1974: Photochemical reactions initiated by and influencing ozone in unpolluted tropospheric air. *Tellus*, 16, 47–56.
- Crutzen, P. J., 1979: The role of NO and NO<sub>2</sub> in the chemistry of the stratosphere and troposphere. *Ann. Rev. Earth Planet Sci.*, 7, 443–472.
- Crutzen, P. J., and Lawrence, M. G., 2000: The impact of precipitation scavenging on the transport of trace gases: A 3-dimensional model sensitivity study. *J. Atmos. Chem.*, 37, 81–112.
- Crutzen, P. J., Heidt, L. E., Krasnec, J. P., Pollock, W. H., and Seiler, W., 1979: Biomass burning as a source of atmospheric gases CO, H<sub>2</sub>, N<sub>2</sub>O, NO, CH<sub>3</sub>Cl and COS. *Nature*, 282, 253–256.
- Damian-Iordache, V., 1996: *KPP — Chemistry Simulation Development Environment*. M.Phil. thesis, University of Iowa, Iowa City, Iowa.
- Dawson, G. A., 1980: Nitrogen-fixation by lightning. *J. Atmos. Sci.*, 37(1), 174–178.
- Dentener, F., Peters, W., Krol, M., van Weele, M., Bergamashi, P., and Lelieveld, J., 2003: Interannual variability and trend of CH<sub>4</sub> lifetime as a measure of OH changes in the 1979–1993 time period. *J. Geophys. Res.*, 108(D15), 4442, doi:10.1029/2002JD002916.
- Dentener, F. J., and Crutzen, P. J., 1993: Reaction of N<sub>2</sub>O<sub>5</sub> on tropospheric aerosols: impact on the global distributions of NO<sub>x</sub>, O<sub>3</sub>, and OH. *J. Geophys. Res.*, 98, 7149–7163.
- Drapcho, D. L., Sisterson, D., and Kumar, R., 1983: Nitrogen fixation by lightning activity in a thunderstorm. *J. Geophys. Res.*, 19(4), 729–734.
- Eigen, M., and Demaeyer, L., 1958: Self dissociation and protonic charge transport in water and ice. *Proc. Roy. Soc.*, 247(1251), 505–533.
- Emmons, L. K., Hauglustaine, D. A., Müller, J.-F., Carroll, M. A., Brasseur, G. P., Brunner, D., Staehelin, J., Thouret, V., and Marenco, A., 2000:

- Data composites of airborne observations of tropospheric ozone and its precursors. *J. Geophys. Res.*, 105, 20497–20538.
- Fall, R., 1999: *Biogenic Emissions of Volatile Organic Compounds from Higher Plants*. Academic Press Pages 41–96.
- Fehr, T., Holler, H., and Huntrieser, H., 2004: Model study on production and transport of lightning-produced  $\text{NO}_x$  in a EULINOX supercell storm. *J. Geophys. Res.*, 109(D), D09102, doi:10.1029/2003JD003935.
- Folkens, I., and Chatfield, R., 2000: Impact of acetone on ozone production and OH in the upper troposphere at high  $\text{NO}_x$ . *J. Geophys. Res.*, 105, 11585–11599.
- Franzblau, E., and Popp, C. J., 1989: Nitrogen oxides produced from lightning. *J. Geophys. Res.*, 94(D8), 11089–11104.
- Galanter, M., Levy, H. II, and Carmichael, G. R., 2000: Impacts of biomass burning on tropospheric CO,  $\text{NO}_x$ , and  $\text{O}_3$ . *J. Geophys. Res.*, 105, 6633–6653.
- Gallardo, L., 1996: *Oxidized Nitrogen in the Troposphere: The role of Lightning*. Ph.D. thesis, Stockholm University.
- Gallardo, L., and Cooray, V., 1996: Could cloud-to-cloud discharges be as effective as cloud-to-ground discharges in producing  $\text{NO}_x$ ? *Tellus*, 48B, 641–651.
- Ganzeveld, L., and Lelieveld, J., 1995: Dry deposition parameterization in a chemical general circulation model and its influence on the distribution of reactive trace gases. *J. Geophys. Res.*, 100, 20999–21012.
- Ganzeveld, L., Lelieveld, J., and Roelofs, G.-J., 1998: A dry deposition parameterization for sulfur oxides in a chemistry and general circulation model. *J. Geophys. Res.*, 103, 5679–5694.
- Goldenbaum, G. C., and Dickerson, R. R., 1993: Nitric-oxide Production by Lightning discharges. *J. Geophys. Res.*, 98(D10), 18333–18338.

- Grenet, G., 1947: Electricite atmospherique - un electrometre a lampes destine aux mesures d'electricite atmospherique. *Comptes Rendus Hebdomadaires Des Seances de l'Academie des Sciences*, 225(14), 585–634.
- Guenther, A., Hewitt, C. N., Erickson, D., Fall, R., Geron, C., Graedel, T., Harley, P., Klinger, L., Lerdau, M., McKay, W. A., Pierce, T., Scholes, B., Steinbrecher, R., Tallamraju, R., Taylor, J., and Zimmerman, P., 1995: A global model of natural volatile organic compound emissions. *J. Geophys. Res.*, 100, 8873–8892.
- Hack, J. J., 1994: Parameterization of moist convection in the National Center for Atmospheric Research community climate model (CCM2). *J. Geophys. Res.*, 99, 5551–5568.
- Hamid, E. Y., Kawasaki, Z.-I., and Mardiana, R., 2001: Impact of the 1997-98 El Niño event on lightning activity over Indonesia. *Geophys. Res. Lett.*, 28(1), 147–150.
- Helas, G., and Kesselmeier, J., 1993: Estimates on sinks and sources of formic and acetic acid. *Pages 299–304 of: Slanina, J., Angeletti, G., and Beilke, S. (eds), General Assessment of Biogenic Emissions and Deposition of Nitrogen Compounds, Sulphur Compounds and Oxidants in Europe.*
- Hill, R. D., Rinker, R. G., and Wilson, H. D., 1980: Atmospheric nitrogen-fixation by lightning. *J. Atmos. Sci.*, 37(1), 179–192.
- Holtslag, A. A. M., and Boville, B. A., 1993: Local versus nonlocal boundary-layer diffusion in a global climate model. *J. Climate*, 6, 1825–1841.
- Houweling, S., Dentener, F., and Lelieveld, J., 1998: The impact of non-methane hydrocarbon compounds on tropospheric photochemistry. *J. Geophys. Res.*, 103, 10673–10696.
- Huntrieser, H., Feigl, C., Schlager, H., Schröder, F., Gerbig, C., van Velthoven, P., Flatøy, F., They, C., Petzold, A., Holler, H., and Schu-

- mann, U., 2002: Airborne measurements of  $\text{NO}_x$ , tracer species, and small particles during the European Lightning Nitrogen Oxides Experiment. *J. Geophys. Res.*, 107(D11), 4113 doi: 10.1029/2000JD000209.
- Jaeglé, L., Jacob, D. J., Wennberg, P. O., Spivakovsky, C. M., Hanisco, T. F., Lanzendorf, E. J., Hints, E. J., Fahey, D. W., Keim, E. R., Proffitt, M. H., Atlas, E. L., Flocke, F., Schauffler, S., McElroy, C. T., Midwinter, C., Pfister, L., and Wilson, J. C., 1997: Observed OH and  $\text{HO}_2$  in the upper troposphere suggest a major source from convective injection of peroxides. *Geophys. Res. Lett.*, 24, 3181–3184.
- Jayarathne, E. R., and Saunders, C. P. R., 1985: The rain gush, lightning, and the lower positive charge center in thunderstorms. *J. Geophys. Res.*, 89(D10), 11816–11818.
- Kowalczyk, M., and Bauer, E., 1982 (December). *Lightning as a source of  $\text{NO}_x$  in the troposphere*. Technical Memorandum ORNL/TM-2001/268. Federal Aviation Administration, Oak Ridge, Tenn.
- Krehbiel, P. R., 1986: *The electrical structure of thunderstorms*. Vol. 18 Washington, DC: National academy Press Pages 90–113.
- Krol, M., van Leeuwen, P. J., and Lelieveld, J., 1998: Global OH trend inferred from methyl-chloroform measurements. *J. Geophys. Res.*, 103, 10697–10711.
- Kumar, P. P., Manohar, G. K., and Kandalgaonkar, S. S., 1995: Global distribution of nitric-oxide produced by lightning and its seasonal variation. *J. Geophys. Res.*, 100(D6), 11203–11208.
- Labrador, L., von Kuhlmann, R., and Lawrence, M. G., 2004a: The effects of lightning-produced  $\text{NO}_x$  and its vertical distribution on atmospheric chemistry: sensitivity simulations with MATCH-MPIC. *Atmos. Chem. Phys. Discuss.*, 4, 6239–6281.
- Labrador, L., von Kuhlmann, R., and Lawrence, M. G., 2004b: Strong sensitivity of the global mean OH concentration and the troposphere's

- oxidizing efficiency to the source of  $\text{NO}_x$  from lightning. *Geophys. Res. Lett.*, 31(L06102), L06102, doi:10.1029/20003GL019229.
- Landgraf, J., and Crutzen, P. J., 1998: An efficient method for online calculations of photolysis and heating rates. *J. Atmos. Chem.*, 25, 863–878.
- Latham, J, and Mason, B.J., 1961: Electric charge transfer associated with temperature gradients in ice. *Proc. Roy. Soc.*, 260(130), 523.
- Lawrence, M. G., 1996: *Photochemistry in the Tropical Pacific Troposphere: Studies with a Global 3D Chemistry-Meteorology Model*. Ph.D. thesis, Georgia Institute of Technology.
- Lawrence, M. G., and Crutzen, P. J., 1998: The impact of cloud particle gravitational settling on soluble trace gas distributions. *Tellus*, 50B, 263–289.
- Lawrence, M. G., and Crutzen, P. J., 1999: Influence of  $\text{NO}_x$  emissions from ships on tropospheric photochemistry and climate. *Nature*, 402, 167–170.
- Lawrence, M. G., and Rasch, P., 2005: Trace transport in deep convective updrafts: plume ensemble versus bulk formulation. *J. Atmos. Sci.*, in press.
- Lawrence, M. G., Chameides, W. L., Kasibhatla, P. S., Levy II, H., and Moxim, W., 1995: *Lightning and atmospheric chemistry: The rate of atmospheric NO production*. Vol. I CRC Press, Inc. Pages 189–202.
- Lawrence, M. G., Crutzen, P. J., Rasch, P. J., Eaton, B. E., and Mahowald, N. M., 1999: A model for studies of tropospheric photochemistry: Description, global distributions, and evaluation. *J. Geophys. Res.*, 104, 26245–26277.
- Lawrence, M. G., Jöckel, P., and von Kuhlmann, R., 2001: What does the global mean OH concentration tell us? *Atmos. Chem. Phys.*, 1, 37–49.

- Lawrence, M. G., von Kuhlmann, R., and Salzmann, M., 2003: The balance of effects of deep convective mixing on tropospheric ozone. *Geophys. Res. Lett.*, 30(18), 1940, doi:10.1029/2003GL017644.
- Lee, D. S., Köhler, I., Grobler, E., Rohrer, F., Sausen, R., Gallardo-Klenner, L., Olivier, J. G. J., Dentener, F. J., and Bouwman, A. F., 1997: Estimations of global NO<sub>x</sub> emissions and their uncertainties. *Atmos. Environ.*, 31, 1735–1749.
- Levine, J. S., Rogowski, R. S., Gregory, G. L., Howell, W. E., and Fishman, J., 1981: Simultaneous measurements of NO<sub>x</sub>, NO and O<sub>3</sub> production in a laboratory discharge: atmospheric implications. *Geophys. Res. Lett.*, 8(4), 357–360.
- Levy, H., Moxim, W. J., and Kasibhatla, P. S., 1996: A global three-dimensional time-dependent lightning source of tropospheric NO<sub>x</sub>. *J. Geophys. Res.*, 101(D17), 22911–22922.
- Liaw, Y. P., Sisterson, D. L., and Miller, N. L., 1990: Comparison of field, laboratory, and theoretical estimates of global nitrogen-fixation by lightning. *J. Geophys. Res.*, 22(D13), 22489–22494.
- Liu, S. C., Kley, D., and McFarland, M., 1980: On the origin of tropospheric ozone. *J. Geophys. Res.*, 85(C12), 7546–7552.
- McCollum, J R, Gruber, A, and Ba, M B., 2000: Discrepancy between gages and satellite estimates of rainfall in equatorial Africa. *J. Appl. Met.*, 39, 666–679.
- Montzka, S. A., Spivakovsky, C. M., Butler, J. H., Elkins, J. W., Lock, L. T., and Mondeel, D. J., 2000: New observational constraints for atmospheric hydroxyl on global and hemispheric scales. *Science*, 288, 500–503.
- Navarro-Gonzales, R., Villagran-Muniz, M., Molina, L.T., and Molina, M., 2001: The physical mechanism of nitric oxide formation in simulated lightning. *Geophys. Res. Lett.*, 28(20), 3867–3870.

- Nesbitt, S. W., Zhang, R., and Orville, R. E., 2000: Seasonal and global  $\text{NO}_x$  production by lightning estimated from the Optical Transient Detector (OTD). *Tellus*, 52B, 1206–1215.
- Noxon, J. F., 1976: Atmospheric nitrogen-fixation by lightning. *Geophys. Res. Lett.*, 3(8), 463–465.
- Olivier, J. G. J., Bloos, J. P. J., Berdowski, J. J. M., Visschedijk, A. J. H., and Bouwman, A. F., 1999: A 1990 global emission inventory of anthropogenic sources of carbon monoxide on  $1^\circ \times 1^\circ$  developed in the framework of EDGAR/GEIA. *Chemosphere: Global Change Science*, 1, 1–17.
- Orville, R. E., and Huffines, G. R., 2001: Cloud-to-ground lightning in the United States: NLDN results in the first decade, 1989–1998. *Mon. Weather Rev.*, 129, 1179–1193.
- Petersen, W A, and Rutledge, S A., 2001: Regional variability in tropical convection: Observations from TRMM. *J. Climate*, 15, 3566–3586.
- Petersen, W A, Nesbitt, S W, Blakeslee, R J, Cifelli, R, Hein, P, and Rutledge, S A., 2002: TRMM observations of intraseasonal variability in convective regimes over the Amazon. *J. Climate*, 15, 1278–1294.
- Peyroux, R., and Lapyere, R. M., 1982: Gaseous products created by electrical discharges in the atmosphere and condensation nuclei resulting from gaseous-phase reactions. *Atmos. Environ.*, 6(5), 959–968.
- Pickering, K. E., Wang, Y., Tao, W. K., Price, C., and Müller, J-F., 1998: Vertical distributions of lightning  $\text{NO}_x$  for use in regional and global chemical transport models. *J. Geophys. Res.*, 103(D23), 31203–31216.
- Plass-Dülmer, C., Koppmann, R., Ratte, M., and Rudolph, J., 1995: Light non-methane hydrocarbons in seawater. *Global Biogeochem. Cycles*, 9, 79–100.
- Price, C., and Rind, D., 1992: A simple lightning parameterization for calculating global lightning distributions. *J. Geophys. Res.*, 97, 9919–9933.

- Price, C., and Rind, D., 1994: Modeling global lightning distributions in a general circulation model. *Mon. Weather Rev.*, 122, 1930–1939.
- Price, C., Penner, J., and Prather, M., 1997a: NO<sub>x</sub> from lightning: 1. Global distribution based on lightning physics. *J. Geophys. Res.*, 102, 5929–5941.
- Price, C., Penner, J., and Prather, M., 1997b: NO<sub>x</sub> from lightning: 2. Constraints from the global atmospheric electric circuit. *J. Geophys. Res.*, 102, 5942–5951.
- Prinn, R. G., Weiss, R. F., Miller, B. R., Huang, J., Alya, F. N., Cunnold, D. M., Fraser, P. J., Hartley, D. E., and Simmonds, P. G., 1995: Atmospheric trends and lifetime of CH<sub>3</sub>CCl<sub>3</sub> and global OH concentrations. *Science*, 269, 187–190.
- Prinn, R. G., Huang, J., Weiss, R. F., Cunnold, D. M., Fraser, P. J., Simmonds, P. G., McCulloch, A., Harth, C., Salameh, P., O’Doherty, S., Wang, R. J. J., Porter, L., and Miller, B. R., 2001: Evidence for substantial variations of atmospheric hydroxyl radicals in the past two decades. *Science*, 292, 1882–1888.
- Pruppacher, H R, and Klett, J D., 1997: *Cloud Electricity*. Vol. 18 Kluwer Academic Publishers Pages 792–852.
- Rakov, V A, and Uman, M., 2003: *Electrical structure of lightning-producing clouds*. Cambridge University Press.
- Rasch, P. J., and Kristjánsson, J. E., 1998: A comparison of the CCM3 model climate using diagnosed and predicted condensate parameterizations. *J. Climate*, 11, 1587–1614.
- Rasch, P. J., Boville, B. A., and Brasseur, G. P., 1995: A three-dimensional general circulation model with coupled chemistry for the middle atmosphere. *J. Geophys. Res.*, 100, 9041–9071.

- Ridley, B. A., Dye, J. E., Walega, J. G., Zheng, J., Grahek, F. E., and Rison, W., 1996: On the production of active nitrogen by thunderstorms over New Mexico. *J. Geophys. Res.*, 101(D15), 20985–21005.
- Saunders, C. P. R., 1995: *Thunderstorm Electrification*. Vol. I CRC Press, Inc. Pages 61–92.
- Schubert, S. D., Rood, R. B., and Pfaendtner, J., 1993: An assimilated data set for Earth Science applications. *Bull. Am. Meteorol. Soc.*, 74, 2331–2342.
- Seinfeld, J. H., and Pandis, S. N., 1998: *Atmospheric Chemistry and Physics*. Wiley-Interscience.
- Singh, H., Chen, Y., Tabazadeh, A., Fukui, Y., Bey, I., Yantosca, R., Jacob, D., Arnold, F., Wohlfrom, K., Atlas, D., Flocke, F., Blake, D., Blake, N., Heikes, B., Snow, J., Talbot, R., Gregory, G., Sachse, G., Vay, S., and Kondo, Y., 2000: Distribution and fate of selected oxygenated organic species in the troposphere and lower stratosphere over the Atlantic. *J. Geophys. Res.*, 105, 3795–3805.
- Sisterson, D. L., and Liaw, Y. P., 1990: An evaluation of lightning and corona discharge on thunderstorm air and precipitation chemistry. *J. Atmos. Chem.*, 10(1), 83–96.
- Slingo, J. M., 1987: The development and verification of a cloud prediction scheme for the ECMWF model. *Q. J. R. Meteorol. Soc.*, 113, 899–927.
- Spivakovsky, C. M., Logan, J. A., Montzka, S. A., Balkanski, Y. J., Foreman-Fowler, M., Jones, D. B. A., Horowitz, L. W., Fusco, A. C., Brenninkmeijer, C. A. M., Prather, M. J., Wofsy, S. C., and McElroy, M. B., 2000: Three-dimensional climatological distribution of tropospheric OH: Update and evaluation. *J. Geophys. Res.*, 105, 8931–8980.
- Stark, M. S., Harrison, J. T. H., and Anastasi, C., 1996: Formation of nitrogen oxides by electrical discharges and implications for Atmospheric Lightning. *J. Geophys. Res.*, 101(D3), 6963–6969.

- Stockwell, D. Z., Giannakopoulos, C., Plantevin, P. H., Carver, G. D., Chipperfield, M. P., Law, K. S., Pyle, J. A., Shallcross, D. E., and Wang, K.-Y., 1999: Modelling  $\text{NO}_x$  from lightning and its impact on global chemical fields. *Atmos. Environ.*, 33, 4477–4493.
- Tie, X., Brasseur, G., Emmons, L., Horowitz, L., and Kinnison, D., 2001: Effects of aerosols on tropospheric oxidants: A global model study. *J. Geophys. Res.*, 106, 22931–22964.
- Tie, X., Zhang, R., Brasseur, G., and Lei, W., 2002: Global  $\text{NO}_x$  production by lightning. *J. Atmos. Chem.*, 43(1), 61–74.
- Tuck, A. F., 1976: Production of nitrogen-oxides by lightning discharges. *Q. J. R. Meteorol. Soc.*, 102(434), 749–755.
- Turman, B. N., 1978: Analysis of lightning data from DMSP satellite. *J. Geophys. Res.*, 83(NC10), 5019–5024.
- Turman, B. N., and Edgar, B. C., 1982: Global lightning distributions at dawn and dusk. *J. Geophys. Res.*, 87, 1191–1206.
- Uman, M., 1987: *The Lightning Discharge*. Academic Press Inc.
- Uman, M., and Krider, P., 1989: Natural and artificially initiated lightning. *Science*, 246(4929), 457–464.
- Ushio, T., Heckman, S. J., Boccipio, D. J., and Christian, H., 2001: A survey of thunderstorms flash rates compared to cloud top heights using TRMM satellite data. *J. Geophys. Res.*, 106(D20), 24089–24095.
- Verwer, J. G., Spee, E. J., Blom, J. G., and Hundsdorfer, W. H., 1997: *A second order Rosenbrock method applied to photochemical dispersion problems*. MAS-R9717. Centrum voor Wiskunde en Informatica, Amsterdam.
- Verwer, J. G., Spee, E. J., Blom, J. G., and Hundsdorfer, W. H., 1999: A second order Rosenbrock method applied to photochemical dispersion problems. *SIAM J. Sci. Comput.*, 20, 1456–1480.

- von Kuhlmann, R., Lawrence, M. G., Crutzen, P. J., and Rasch, P. J., 2003a: A model for studies of tropospheric ozone and non-methane hydrocarbons: model evaluation of ozone related species. *J. Geophys. Res.*, 108(D28), 4729, doi:10.1019/2002JD003348.
- von Kuhlmann, R., Lawrence, M. G., Crutzen, P. J., and Rasch, P. J., 2003b: A model for studies of tropospheric ozone and nonmethane hydrocarbons: Model description and ozone results. *J. Geophys. Res.*, 108(D9), 4294, doi:10.1029/2002JD002893.
- von Kuhlmann, R., Lawrence, M. G., Pöschl, U., and Crutzen, P. J., 2004: Sensitivities in global scale modeling of isoprene. *Atmos. Chem. Phys.*, 4, 1–17.
- von Kuhlmann, Rolf., 2001: *Tropospheric Photochemistry of Ozone, its Precursors and the Hydroxyl Radical: A 3D-Modeling Study Considering Non-Methane Hydrocarbons*. Ph.D. thesis, Johannes Gutenberg-Universität Mainz, Mainz, Germany.
- von Liebig, J., 1827: Extrait d'une note sur la nitrification. *Ann. Chem. Phys.*, 35, 329–333.
- Vonnegut, B., 1953: Possible mechanisms for the formation of thunderstorm electricity. *Bull. Am. Meteorol. Soc.*, 34.
- Wang, Y, DeSilva, A. W., Goldenbaum, G. C., and Dickerson, R. R., 1998: Nitric oxide production by simulated lightning: dependence on current, energy, and pressure. *J. Geophys. Res.*, 103(D15), 19149–19159.
- Wesely, M. L., 1989: Parameterization of surface resistances to gaseous dry deposition in regional-scale numerical models. *Atmos. Environ.*, 23, 1293–1304.
- Wettlaufer, J. S., and Dash, J. G., 2000: Melting below zero. *Scient. American*, 282(2), 34–37.

- Williams, E., 1988: The electrification of thunderstorms. *Scient. American*, 295(5), 48–65.
- Williams, E R., 1992: The Schumann resonance: A global thermometer. *Science*, 256(1251), 1184–1187.
- Wilson, C. T. R., 1920: Investigations on lightning discharges and on the electric field of thunderstorms. *Philos. Trans. R. Soc. London Ser. A.*, 221, 73–115.
- Yienger, J. J., and Levy, H. II., 1995: Empirical model of global soil-biogenic  $\text{NO}_x$  emissions. *J. Geophys. Res.*, 100, 11447–11464.
- Zel'dovitch, Y B, and Razier, Y P., 1966: *Physics of Shock Waves and High-Temperature Hydrodynamic Phenomena*. Academic Press, Inc., New York.
- Zhang, G. J., and McFarlane, N. A., 1995: Sensitivity of climate simulations to the parameterization of cumulus convection in the Canadian Climate Centre General Circulation Model. *Atmos. Ocean*, 33, 407–446.
- Zhang, X. J., Helsdon Jr., J. H., and Farley, R. D., 2003: Numerical modeling of lightning-produced  $\text{NO}_x$  using an explicit lightning scheme: 1. Three-dimensional simulation and expanded chemistry. *J. Geophys. Res.*, 108(D18), 4580, doi:10.1029/2002JD003225.
- Zipser, E J., 1994: Deep cumulonimbus cloud systems in the tropics with and without lightning. *Mon. Weather Rev.*, 122, 1837–1854.

# Acknowledgements

In the years spent at the Max Planck Institute for Chemistry, I came to realize that a PhD is definitely a collaborative undertaking. It requires the help, assistance and guidance of many people to turn an aspiring candidate into a fully-fledged and independent researcher. I hereby would like to give credit to all those people who, in many different ways, helped me tread this path and made this work possible.

First and foremost, I would like to express my most sincere gratitude to Dr. Mark G. Lawrence. First, for making me a part of his group, thereby giving me the opportunity to explore this wonderful field of the atmospheric sciences. Second, for his insight, patience, dedication and overall guidance, which were instrumental in showing me the way toward the successful completion of this project, all the while making it fun. Third, for being a friend.

I am also deeply indebted to Prof. Dr. Ulrich Platt, for opening the doors of the Institut für Umweltphysik of the University of Heidelberg to me and for his tutorship and suggestions throughout this project.

I have a special debt of gratitude with Dr. Rolf von Kuhlmann. Throughout my stay at the Max Planck Institute, Rolf served as a co-tutor of sorts, showing me, with generous doses of patience, some of the intricacies and “tricks of the trade” of the art of modeling. He was always there to answer any questions I might have had. Likewise, thanks for the many “extracurricular” activities done together, which went a long way to keeping my sanity in good shape all along, as well as for being such a fine friend.

I would also like to thank in a very special way Drs. Betina Kleiss and Alejandro Mujica, for opening me the doors of their home when I first came to Germany and for being the wonderful people they have been throughout these years. Betina, you taught me the meaning of the word “serendipity”.

Thanks also go to Drs. Laurens Ganzeveld and John vann Aardenne, both for the very interesting and stimulating scientific discussions as well as their warmth and friendship.

Thanks to all my room- and groupmates, past and present: Marc Salzmann, Kunhikrishnan Thengumthara, Rüdiger Lang, Boris Bonn, Tim Butler, Jörg Steinkamp, Karin Oliveira Dos Santos and Claudia Keller. Working with and alongside you has been a privilege.

Special thanks go to Marc Salzmann, for his interesting and wide-ranging discussions as well as for his kind help in matters technical.

Thanks also to Drs. Roland von Glasow, Christoph Brühl, Patrick Jöckel and Rolf Sander for their welcome and orientation when taking my first steps in the MPI modeling community.

I would also like to thank the institute’s system administrators: K. Egenolf, Drs. M. Körfer, H. Gimm and T. Wawers for their constant support and overall nice attitude.

I would also like to thank the administrative staff of the Max Planck Institute, specially Bettina Krüger, Herr May, Frau Winkler and Frau Katsch, who were always ready to make things easy for me with a smile in their faces.

I like to sincerely thank Sandra Bartenbach for extending her hand in times of trouble. Thank you brat.

Thanks to Mathias Zöllner (aka “The Iceman”) for the good times and heartfelt friendship.

Thanks to many other of my colleagues at the institute, who helped create that great working atmosphere there, among them: Meryem Tanarhte, Udo Rummel, Patience Gwaze, Lutz Lange, Marian de Reus, Jessica Valverde, Araceli Bracho, Giomar Chaparro and Andrea Pozzer.

Special thanks go to Dr. Giovanni Caselotti, for being a friend and a wonderful person.

To my *mitbewohner* past and present: Mauri, Cristina, Javier, Jacob and Sebastian for their friendship and camaraderie and, most of all, for their understanding and for putting up with my rather somber moods during stressy times.

Finally, I would like to thank my parents. Without their support and immense love I would simply not have made it.